II. PLASMA DYNAMICS

II-A. PLASMA PHYSICS*

Prof. S. C. Brown
Prof. W. P. Allis
Prof. D. J. Rose
Prof. D. R. Whitehouse
Dr. G. Bekefi
Dr. B. Brandt
Dr. S. Gruber
V. Arunasalam
C. D. Buntschuh
J. D. Coccoli
E. W. Fitzgerald, Jr.
S. Frankenthal
P. J. Freyheit
J. C. Ingraham
W. R. Kittredge
J. J. McCarthy
W. J. Mulligan
J. J. Nolan, Jr.
J. C. Terlouw
K. F. Voyenli
R. E. Whitney

1. NEGATIVE CONDUCTIVITY IN A PLASMA

In an effort to better understand negative conductivity (1) (or amplification of plane electromagnetic waves in a plasma) an attempt was made to solve the Boltzmann equation for a warm plasma by employing a perturbation technique. Our approach follows that of

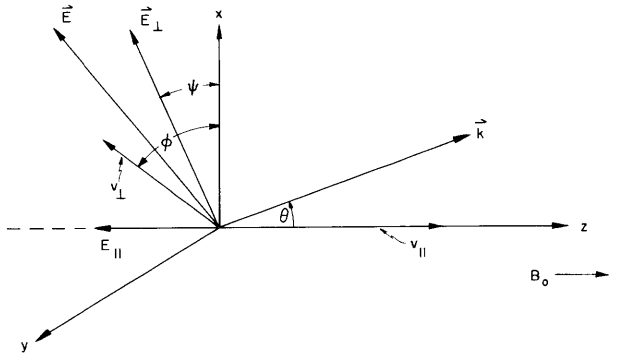

Fig. II-1. Coordinate system for conductivity calculations.

Buchsbaum (2) except that a nonspherical equilibrium distribution was allowed and the perturbation in the distribution function was found.

The geometrical configuration is illustrated in Fig. II-1. The x-z plane contains the plane wave propagation vector $\vec{k}$. The z-axis is chosen in the direction of the uniform dc magnetic field.

From Fig. II-1 we see that

$$\vec{k} = \vec{a}_z k_{||} + \vec{a}_x k_\perp$$

and

*This work was supported in part by the Atomic Energy Commission under Contract AT(30-1)1842; and in part by the Air Force Command and Control Development Division under Contract AF19(604)-5992; and in part by National Science Foundation under Grant G-9330.

$$\vec{E} = \vec{a}_z E_{\parallel} + \vec{a}_x E_{\perp} \cos\psi + \vec{a}_y E_{\perp} \sin\psi$$

where E is the ac electric field, and no dc electric field is assumed to exist. If $f = f_o + f_1$, where f is the distribution in the presence of a plane wave, f_o is the unperturbed distribution function, and f_1 is the small perturbation of the original distribution function, then the equation for the perturbation in terms of the fields and the unperturbed distribution is

$$\frac{\partial f_1}{\partial t} + \vec{v} \cdot \nabla_r f_1 - \frac{e}{m}\vec{E}_1 \cdot \frac{\partial f_o}{\partial \vec{v}} - \frac{e}{m}\vec{v} \times \vec{B}_o \cdot \frac{\partial f_1}{\partial \vec{v}} - \frac{e}{m}\vec{v} \times \vec{B}_1 \cdot \frac{\partial f_o}{\partial \vec{v}} = -\nu_c f_1 \tag{1}$$

where

$$\vec{E} = \vec{E}_1 \, e^{-j(\omega t - \vec{k}\cdot\vec{r})}$$

and

$$\vec{B} = \vec{B}_o + \vec{B}_1 \, e^{-j(\omega t - \vec{k}\cdot\vec{r})}$$

If we assume that $f_1 = F(\vec{v}) \exp[-j(\omega t - \vec{k}\cdot\vec{r})]$, then

$$\frac{\partial F}{\partial \phi} - j\frac{(\omega - \vec{k}\cdot\vec{v} + j\nu_c)}{\omega_B}F - \frac{e}{m}\left[\frac{1}{\omega_B} - \frac{\vec{k}\cdot\vec{v}}{\omega\omega_B}\right]\vec{E}_1 \cdot \frac{\partial f_o}{\partial \vec{v}} - \frac{e}{m}\frac{\vec{v}\cdot\vec{E}}{\omega_B \omega}\vec{k} \cdot \frac{\partial f_o}{\partial \vec{v}} = 0 \tag{2}$$

To find this solution, we used the plane wave relationship

$$\vec{B}_1 = \frac{\vec{k} \times \vec{E}_1}{\omega}$$

Equation 2 can easily be solved for F to yield

$$F = \frac{1}{2}\frac{eE_{\perp}}{B_o} e^{-j\beta\sin\phi} \sum_{m=-\infty}^{\infty} J_m(\beta)\left[\frac{\exp(-j(a+m-2)\phi - j\psi)}{-j(a+m-1)} + \frac{\exp(-j(a+m)\phi + j\psi)}{-j(a+m+1)}\right]$$

$$\times\left[\frac{\partial f_o}{\partial v_{\perp}} + \frac{v_{\perp}}{c_{\parallel}}\frac{\partial f_o}{\partial v_{\parallel}} - \frac{v_{\parallel}}{c_{\parallel}}\frac{\partial f_o}{\partial v_{\perp}}\right] + \frac{1}{2}\frac{eE_{\parallel}}{B_o} e^{-j\beta\sin\phi} \sum_{m=-\infty}^{\infty} J_m(\beta)$$

$$\times\left[\frac{\exp(-j(a+m-1)\phi)}{-j(a+m)}\frac{\partial f_o}{\partial v_{\parallel}} - \left(\frac{\exp(-j(a+m-2)\phi)}{-j(a+m-1)} + \frac{\exp(-j(a+m)\phi)}{-j(a+m+1)}\right)\left(\frac{v_{\perp}}{c_{\perp}}\frac{\partial f_o}{\partial v_{\parallel}} - \frac{v_{\parallel}}{c_{\perp}}\frac{\partial f_o}{\partial v_{\perp}}\right)\right] \tag{3}$$

where

$$\beta = \frac{k_{\perp} v_{\perp}}{\omega_B}$$

$$a = \frac{\omega - k_{||} v_{||} + j\nu_c}{\omega_B}$$

$$c_{||} = \frac{\omega}{k_{||}}$$

$$c_{\perp} = \frac{\omega}{k_{\perp}}$$

$$\omega_B = \frac{eB}{m_o}\left(1 - \frac{v_{\perp}^2 + v_{||}^2}{c^2}\right)^{1/2} = \omega_{B_o}\left(1 - \frac{v_{\perp}^2 + v_{||}^2}{c^2}\right)^{1/2}$$

The power absorbed from the field $\vec{E}$ by an electron of velocity $\vec{v}$ is equal to $e\vec{v} \cdot \vec{E}$. The power absorbed by all electrons is the real part of this quantity weighted by F and integrated over all v. Choosing the first harmonic (m=0) and assuming that ν_c is negligibly small so that the term

$$R_e\left[-\frac{1}{j(a-1)}\right] \approx \pi\delta\left(\frac{\omega - k_{||} v_{||}}{\omega_B} - 1\right) = \pi\delta(a-1)$$

we obtain

$$P_{abs} \approx -R_e\left\{\frac{\pi}{4}\frac{e^2E^2}{B_o}\int_0^{\infty} dv_{\perp}\int_{-\infty}^{\infty} dv_{||}\left[e^{-j\beta\sin\phi}\ J_o(\beta)\ v_{\perp}^2\delta(a-1)\frac{\partial f_o}{\partial v_{\perp}}\right]\right\} \tag{4}$$

Here, we have assumed that $E_{||} = 0$, $E = E_{\perp}$; $c_{||} = c_{\perp} = c \gg v_{\perp}, v_{||}$ for the important range of velocities; the phase factor $\exp(-j(a-1)\phi) \approx 1$, since $a \approx 1$; and the term in F that varies as $\frac{-1}{j(a+1)}$ is always negligible.

One integration can be performed without the assumption of an explicit f_o. For the present, we shall consider $\vec{k} = \vec{k}_{||}$, and $f_o(v_{\perp}, v_{||}) = f_{o_{\perp}}(v_{\perp})\, f_{o_{||}}(v_{||})$. For $|\vec{k}| = |\vec{k}_{||}| = \frac{\omega}{c}$, we integrate with respect to ϕ and $v_{||}$ to obtain

$$P_{abs} \approx -R_e\left\{\frac{\pi^2}{2}\frac{e^2E^2}{B_o}\int_0^{\infty} v_{\perp}^2\frac{\partial f_o}{\partial v_{\perp}}\, f_{o_{||}}\left[v_{||} = c\left(1 - \frac{\omega_{B_o}}{\omega} + \frac{v_{\perp}^2}{2c^2}\right)\right] dv_{\perp}\right\} \tag{5}$$

To proceed further we must assume a distribution function. For simplicity of integration and to illustrate the conditions for negative conductivity, let us assume

$$f_{o_{\perp}} = \begin{cases} \frac{\sqrt{n}}{2A^2}(v - v_o + A) & v_o - A \leq v_{\perp} \leq v_o \\ \frac{\sqrt{n}}{2A^2}(v_o + A - v) & v_o \leq v_{\perp} \leq v_o + A \\ 0 & \text{elsewhere} \end{cases}$$

and

$$f_{o_{||}} = \begin{cases} \dfrac{\sqrt{n}}{v_2 - v_1} & v_1 \leq v_{||} \leq v_2 \\ 0 & \text{elsewhere} \end{cases}$$

Then

$$\frac{\partial f_o}{\partial v_\perp} = \begin{cases} \dfrac{\sqrt{n}}{2A^4} & v_o - A \leq v_\perp \leq v_o \\ \dfrac{-\sqrt{n}}{2A^4} & v_o \leq v_\perp \leq v_o + A \\ 0 & \text{elsewhere} \end{cases}$$

and

$$f_{o_{||}}\left[v_{||} = c\left(1 - \frac{\omega_{B_o}}{\omega} + \frac{v_\perp^2}{2c^2}\right)\right] = \begin{cases} \dfrac{\sqrt{n}}{v_{\perp_2} - v_{\perp_1}} & v_{\perp_1} \leq v_\perp \leq v_{\perp_2} \\ 0 & \text{elsewhere} \end{cases}$$

where

$$v_{\perp_1} = \sqrt{2}c\left(\frac{v_1}{c} - \frac{\Delta\omega}{\omega}\right)^{1/2}$$

$$v_{\perp_2} = \sqrt{2}c\left(\frac{v_2}{c} - \frac{\Delta\omega}{\omega}\right)^{1/2}$$

$$\frac{\Delta\omega}{\omega} = \frac{\omega - \omega_{B_o}}{\omega}$$

The integral may now be easily evaluated in terms of $v_{\perp_2}$, $v_{\perp_1}$, v_o, and A for various conditions.

Condition 1. $v_{\perp_2} \leq v_o$ and $v_{\perp_1} \leq v_o - A$. Then

$$P_{abs} \propto -\int_{v_o - A}^{v_{\perp_2}} v_\perp^2 \, dv_\perp = -\frac{v_{\perp_2}^3 - (v_o - A)^3}{3}$$

and hence the plasma exhibits negative conductivity. We note that condition 1 can be obtained by various combinations of $\Delta\omega$ and v_2.

Condition 2. $v_o \leq v_{\perp_2} \leq v_o + A$ and $v_{\perp_2} - v_{\perp_1} > 2A$. Then

$$P_{abs} \propto -\int_{v_o-A}^{v_o} v_\perp^2 \, dv_\perp + \int_{v_o}^{v_{\perp_2}} v_\perp^2 \, dv_\perp$$

$$P_{abs} \propto -\frac{1}{3}\left[v_o^3-(v_o-A)^3\right] + \frac{1}{3}\left[v_{\perp_2}^3 - v_o^3\right]$$

If $A \ll v_o$, then with $v_{\perp_2} \leq v_o + A$, the conductivity is positive.

These calculations (through Eq. 4) are applicable to a plasma of arbitrarily large charge concentration. When the plasma is tenuous, so that $\omega_p^2 = \left(Ne^2/m\epsilon_o\right) < \omega^2$, the following procedure can be adopted for deriving the absorption A, or amplification -A, of a plane wave traveling through the plasma: Compute the absorption per electron A_1 and sum over all electrons after weighting A_1 with the distribution function f. Then,

$$A = 2\pi N \int A_1 \, f(p_\perp, p_{||}) \, p_\perp \, dp_\perp \, dp_{||} \tag{6}$$

where $p_\perp$ and $p_{||}$ are the momentum of the electron perpendicular and parallel to the dc magnetic field, respectively. If the electron has relativistic energies, then $\vec{p} = \epsilon\vec{v}/c^2$. Here, $\epsilon = mc^2\Big/\left[1-\left(v_{||}^2+v_\perp^2\right)\Big/c^2\right]^{1/2}$ is the total energy of the electron.

The absorption A_1 is related to the known (3) rate of cyclotron emission, y, by

$$A_1 = \frac{8\pi^3c^2}{\omega^2\epsilon}\left[\left(\eta + \frac{\epsilon^2}{c^2p_\perp}\frac{\partial\eta}{\partial p_\perp}\right) + \frac{\epsilon\cos\theta}{cp_\perp}\left(p_\perp\frac{\partial\eta}{\partial p_{||}} - p_{||}\frac{\partial\eta}{\partial p_\perp}\right)\right] \tag{7}$$

where θ is the angle between the direction of propagation of the wave and the direction of the dc magnetic field, B_o. We substitute Eq. 7 in Eq. 6, perform an integration by parts, and obtain

$$A = \frac{16\pi^3cN}{\omega^2}\int_{p_{||}}\int_{p_\perp} \eta(\theta)\left[-\frac{\epsilon}{c}\frac{\partial f}{\partial p_\perp} + \cos\theta\left\{p_{||}\frac{\partial f}{\partial p_\perp} - p_\perp\frac{\partial f}{\partial p_{||}}\right\}\right] dp_{||}\, dp_\perp \tag{8}$$

Note that (a) when the wave propagates at right angles to B_o, or (b) when the distribution function is isotropic, the last two terms in the integrand of Eq. 8 become zero. The remaining term can be shown to be identical to that obtained previously (1); in that report, absorption and amplification were calculated for $\theta = \pi/2$.

For low-energy electrons $(v/c)^2 \ll 1$, and in the absence of collisions, we have

$$\eta(\theta) = \frac{e^2\omega^2}{8\pi^2\epsilon_o c}\sum_n \beta_\perp^2 \frac{n^2x^{2n-2}}{2^{2n}(n!)^2}\,\delta[n\omega_B - \omega(1-\beta_{||}\cos\theta)] \tag{9}$$

where $x = (n\beta_\perp \sin\theta)/(1-\beta_{||}\cos\theta)$, $\beta_{||} = v_{||}/c$, $\beta_\perp = v_\perp/c$, and $\omega_B = (eB_o/m)\left[1-\left(\beta_{||}^2+\beta_\perp^2\right)\right]^{1/2}$. We have not succeeded in reducing the solution obtained from Boltzmann's equation to

the "single-particle" solution given by Eqs. 8 and 9. However, comparing Eq. 3 with Eq. 8, we find that the term $\cos\theta\{\ldots\}$ of Eq. 8 is associated with the term $(v\times B_1)\cdot(\partial f_o/\partial\vec{v})$ of Eq. 1; this term also vanishes for isotropic distributions.

Calculations are being made of the amplification of a wave passing through an electron beam, for various distributions $f_{||}$ and $f_{\perp}$. The calculations will be compared with recent experiments (4), to determine whether or not the present theory can explain the observed amplifications.

S. Gruber

References

1. G. Bekefi and J. L. Hirshfield, Cyclotron emission from plasmas with non-Maxwellian distributions, Quarterly Progress Report No. 60, Jan. 15, 1961, pp. 6-13.

2. W. P. Allis and S. J. Buchsbaum, Notes on Plasma Dynamics, Summer Session, M. I. T., 1959 (unpublished).

3. B. A. Trubnikov (English translation of doctoral thesis, Moscow University, 1958), Report AEC-tr-4073, U. S. Atomic Energy Commission.

4. K. K. Chow and R. H. Pantell, Proc. IRE 48, 1865 (1960).

2. MICROWAVE MEASUREMENTS OF THE RADIATION TEMPERATURE OF A PLASMA IN A MAGNETIC FIELD

Measurements were made of the radiation temperature in the positive column of a dc discharge in neon as a function of magnetic field, at various pressures and currents. The positive column was subjected to an axial magnetic field that did not exceed 2000 gauss. The radiation temperature was determined from measurements of the radiated power at a frequency close to 3000 mc. Except for a solenoid to provide the magnetic field, the measuring apparatus was the same as that previously described by Bekefi and Brown (1), and a technique similar to theirs was used to render the interpretation of the radiation temperature independent of plasma absorptivity. Samples of the data are presented in Fig. II-2a and II-2b.

The poor reproducibility that is evident away from cyclotron resonance, is due to the low sensitivity of the radiometer at these values of magnetic field. The radiometer sensitivity is strongly dependent on the absorptivity of the plasma. The closer the value of absorptivity is to 1, the better the sensitivity. Since in our plasmas $\omega_p < \omega$, the absorptivity is low away from cyclotron resonance.

The results show a general decrease of the radiation temperature with increasing magnetic field, except for a resonance at a magnetic field for which the electron orbital frequency equals the measuring frequency. The general decrease with increasing magnetic field is in agreement with calculations and with probe measurements of the electron

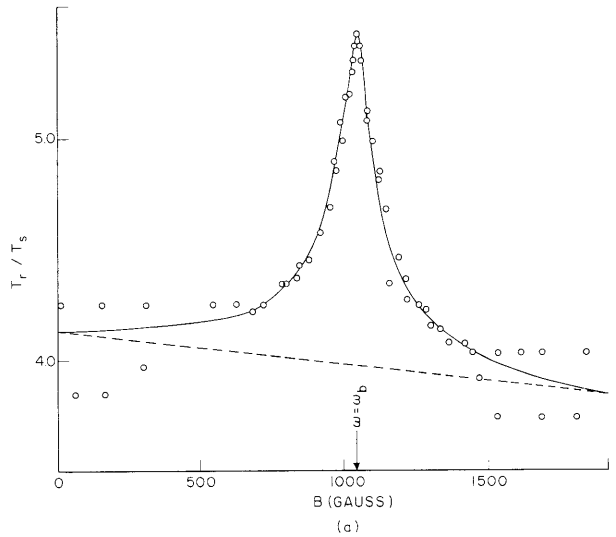

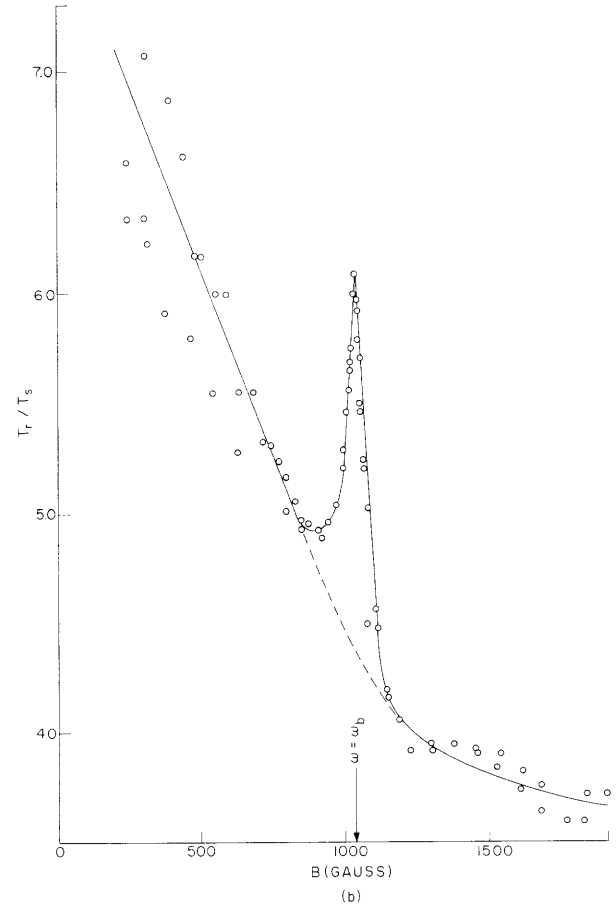

Fig. II-2. Radiation temperature T_r versus magnetic field at constant pressure and current: (a) P_o = 1.2 mm Hg, I = 10 ma, T_s = 10,700°K; (b) P_o = 0.5 mm Hg, I = 30 ma, T_s = 10,700°K.

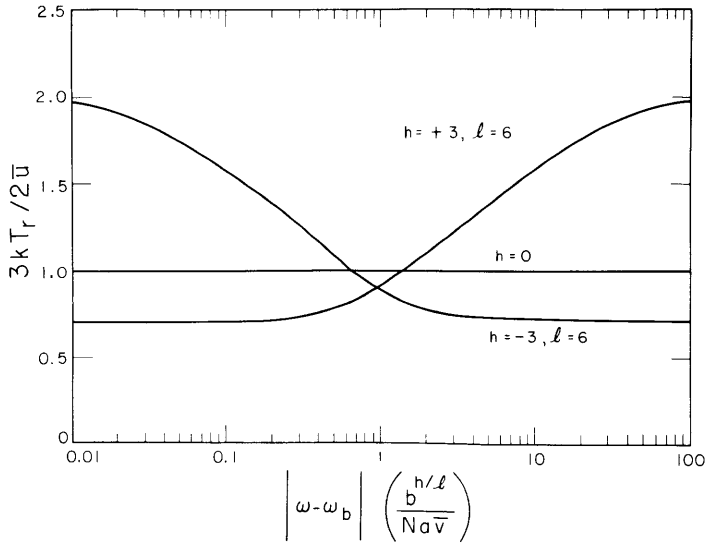

Fig. II-3. The ratio T_r/T_e as a function of frequency.

temperature (2). However, the observed resonance at the cyclotron frequency cannot be interpreted as a resonance of the electron temperature. We attribute the departure of the measured radiation temperature from the electron temperature as being caused by a non-Maxwellian distribution of electron velocities.

Calculations (3) have shown that when the distribution function of electron velocities f(v) deviates from a Maxwellian distribution, the radiation temperature T_r as defined by Kirchhoff's law can deviate significantly from the electron temperature T_e, defined as $3/2\ kT_e = \bar{u}$, where $\bar{u}$ is the mean electron energy. Figure II-3 shows a plot of $3kT_r/2\bar{u}$ as a function of $\omega - \omega_b$, where ω is the measuring frequency, and ω_b is the cyclotron frequency eB/m. Our calculations were made for a distribution function $f(v) = \exp[-b(v/\bar{v})^{\ell}]$, where $\bar{v}$ is the mean electron velocity, and b is an arbitrary positive constant. The electron-atom collision cross section for momentum transfer was taken to be $Q_m = a(v/\bar{v})^{h-1}$, where a is a positive constant and h is a constant greater than or equal to −3.

It can be seen from Fig. II-3 that $T_r = T_e$ whenever either of two conditions is satisfied. Either $\ell = 2$, which is for a Maxwellian distribution, or $h = 0$, which implies a collision time independent of energy. If neither of these conditions is satisfied, $T_r \neq T_e$. Calculations then show that at cyclotron resonance T_r will be greater than T_e if h is positive, and lower than T_e if h is negative. For neon, $h \approx 1$, therefore a resonance peak for T_r at the cyclotron frequency can be expected.

The measured heights of the peaks agree with calculations, but quantitative comparisons with theory have not been made because the precise form of the distribution function is not known.

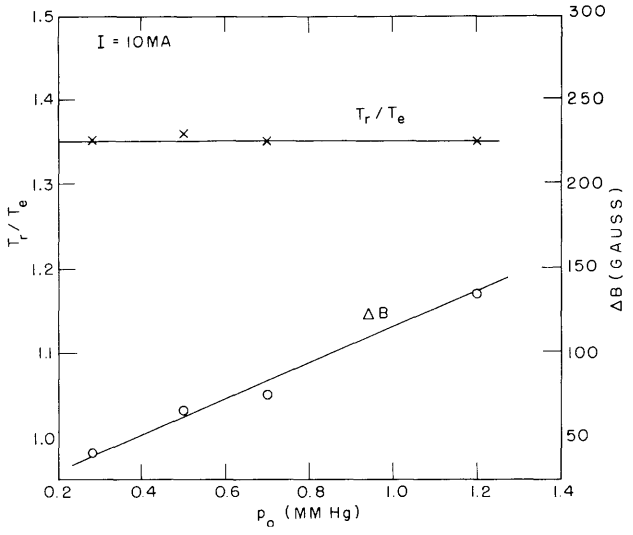

Fig. II-4. The ratio T_r/T_e and the resonance width ΔB as a function of pressure.

The theory also predicts that (a) although the magnitude of T_r at the peak will be a function of pressure, the ratio T_r/T_e should be independent of both pressure and electron density, and (b) the width of the peak should be linearly proportional to the pressure but independent of electron density. (Predictions (a) and (b) refer to a temperature range in which h is constant.) Measurements show that at a given pressure both T_r/T_e at the peak and the resonance width are independent of current. This finding is in agreement with theory, since the density varies almost linearly with current. Figure II-4 shows the variation of T_r/T_e at the peak and its width as a function of pressure for a constant current. These results agree with predictions (a) and (b). At higher pressures and currents (with $\omega_p/\omega > 1$, a region in which the theory does not apply) departures were observed.

In plotting Fig. II-4, T_e was inferred to be the temperature that would have been measured had the resonance not occurred. In other words, T_e was obtained from the monotonically decreasing sections of Fig. II-2a and II-2b, shown by a dashed line.

The resonance width in each case was determined at a value of T_r for a 10 per cent decrease in its peak value.

Further measurements are planned with gases such as argon, xenon, and mercury. For these gases, h changes sign in going from high to low electron energies. At high pressures or low energies h is positive, while at low pressures or high energies h is negative. We can therefore expect a resonance peak, at $\omega = \omega_b$ for high pressures, which should reverse and become a minimal resonance at low pressures.

H. Fields

(Mr. Harvey Fields is from Microwave Associates, Burlington, Massachusetts.)

References

1. G. Bekefi and S. C. Brown, Microwave measurements of the radiation temperature of plasmas, J. Appl. Phys. 32, 25 (1961).

2. R. J. Bickerton and A. von Engel, Phys. Soc. (London) B69, 468 (1956).

3. G. Bekefi, J. L. Hirshfield, and S. C. Brown, Kirchhoff's radiation law for plasmas with non-Maxwellian distributions, Phys. Fluids 4, 173 (1961).

3. INFRARED REFRACTOMETER FOR THE MEASUREMENT OF HIGH ELECTRON DENSITIES

The electron concentration of a plasma can be inferred from the phase change suffered by an electromagnetic wave in its passage through a medium. Generally, the maximum density that can be measured is determined by the condition $(\omega_p/\omega)^2 = \left(ne^2/m\epsilon_o\omega^2\right) < 1$, where ω_p is the plasma frequency, n is the electron density, e and m are the charge and mass of the electron, ϵ_o is the permittivity of free space, and ω is the radian frequency of the wave. With available microwave generators, $n_{max} \approx 10^{14}$ electrons/cc. On the other hand, at frequencies of the visible spectrum, the sensitivity of measurement of phase changes does not permit n_{min} to be less than approximately 10^{16} electrons/cc. The present experiment is designed to bridge the gap between $n \approx 10^{14}$ cm^{-3} and $n \approx 10^{16}$ cm^{-3}, in which range techniques for measurement of n are lacking. The refractometer, designed and constructed by Dr. F. Zernicke, of Block Associates, Cambridge, Massachusetts, is intended to operate at a wavelength of approximately 0.03 cm.

The optical principle of the refractometer can be explained as follows. Consider a light source A (Fig. II-5) that is imaged at B by a lens L. Introduce a grating into the beam between lens and image; then different orders on both sides of the zero order will create a number of coherent light sources, and if these light sources are focused at the proper distance, an image of the grating will be reproduced. An easy way to do this is to focus the images back onto the grating by putting a concave mirror that has a radius of curvature equal to the distance between the grating and B at point B. In other words, the grating is imaged normally on itself by putting it at the center of curvature of a concave mirror. Geometrical optics shows that if the grating is moved laterally, the image moves laterally in the other direction. Physical optics shows that the definition of the image depends on the number of orders reflected by the mirror. An image of relatively poor definition can be obtained by using only the 0, +1, and −1 orders. It can be shown that if a phase

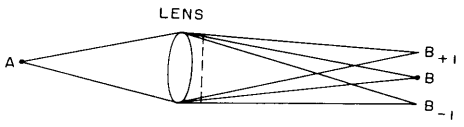

Fig. II-5. Principle of the optical system.

change is introduced in the +1 or the −1 order, the image of the grating will shift in position laterally. A detector placed behind the grating should, therefore, detect a change of signal when a phase change is introduced. If the grating is imaged exactly on itself before the introduction of a phase change, then the shifted image can be brought to coincide with the grating by moving the position of the grating. By measuring the amount of grating displacement the phase change can be calculated, and from this calculation the difference in refractive index between the material used to cause the phase change and air can be obtained.

The actual instrument (see Fig. II-6) consists of a mercury light source (G.E. Type AH-4 with outer glass envelope removed) that is focused by a mirror M_1 onto a large spherical mirror M_2; the grating G is mounted in a sliding mounting.

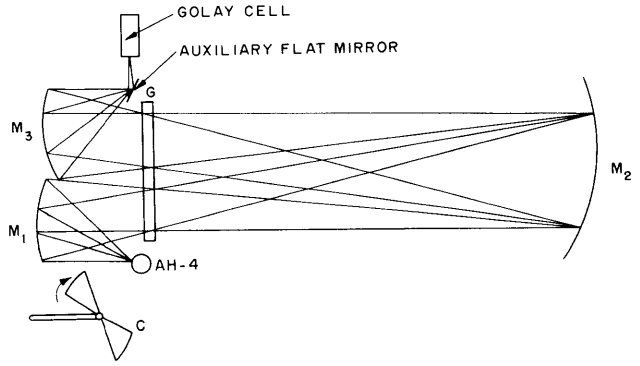

Fig. II-6. Schematic diagram of the optical system.

Mirror M_3 focuses the radiation that comes back to the grating from M_2 onto a Golay detector. A chopper C is used to "chop" the radiation, since the Golay cell is sensitive only to ac signals. The electric signal from the Golay cell is then synchronously rectified and integrated to provide a dc output.

Measurements were made to determine the best way in which to use the Golay detector. Several forms of chopper were tried, and finally a chopper with 15 blades rotating at 60 rpm was chosen. The square-wave signal needed for the synchronous rectification is generated by a separate light source and photocell mounted on opposite sides of the chopper. A small transistorized switching circuit amplifies the square-wave signal so that it can be used to trigger the synchronous rectifier. The synchronous rectifier developed in this laboratory was found to be stable for this application.

Measurements were made to determine the effectiveness of black photographic wrapping paper as a filter for absorbing wavelengths shorter than 150 μ. It is known that this kind of paper transmits approximately 90 per cent of the energy at wavelengths longer than 150 μ. We found that at least three pieces of black paper must be inserted

between the AH-4 source and the Golay cell before the addition of one more piece of paper causes a small difference in signal.

All of the parts for the instrument have been constructed, but an attempt to make it operate in breadboard fashion proved unsuccessful. The instrument was then set up as a refractometer for visible radiation; this experiment indicated a strong need for a rigid mounting of all of the elements. Work on this mounting and other necessary changes has been started. The entire instrument has now been built and is being optically aligned.

S. C. Brown, G. Bekefi

4. THE EFFECT OF PRESSURE ANISOTROPY ON THE LOCAL, MAGNETOHYDRODYNAMIC STABILITY OF NONUNIFORM, STATIC EQUILIBRIUM STATES IN A PLASMA

a. Introduction

In an earlier report (1) we investigated the local instabilities caused by pressure anisotropy in a uniform plasma in a uniform magnetic field. It is the purpose of the present report to investigate the effect of pressure anisotropy on nonuniform equilibrium states by using an energy principle (2). First, a transformation is made of the energy-variation integral, in order to obtain maximum mathematical symmetry between the material and magnetic pressures. Then, possible nonuniform equilibrium states are discussed. It is convenient to distinguish between two classes of possible equilibrium states. For one of these classes an associated isotropic equilibrium state, for which the mathematical treatment of the stability problem can be essentially simplified, is defined.

b. Basic Equations and the Energy Principle for Stability

The discussion is based upon the so-called double-adiabatic, anisotropic magnetohydrodynamics (2). The continuity equation is

$$\frac{d\rho}{dt} + \rho\nabla \cdot \underline{v} = 0$$

The momentum equation is

$$\rho \frac{d\underline{v}}{dt} = -\nabla \cdot \underline{\underline{P}} + \underline{j} \times \underline{B}$$

where the pressure tensor $\underline{\underline{P}}$ is of the form $\underline{\underline{P}} = p_{||}\underline{e}\,\underline{e} + p_{\perp}(\underline{\underline{I}} - \underline{e}\,\underline{e}) = p_{\perp}\underline{\underline{I}} - \Delta p\,\underline{e}\,\underline{e}$, with $\underline{e} = \underline{B}/B$; $\underline{\underline{I}}$ is the unit tensor; and $\Delta p = p_{\perp} - p_{||}$. There are two adiabatic equations for the components of the pressure:

$$\frac{dp_{||}}{dt} = -p_{||}\nabla \cdot \underline{v} - 2p_{||}(\underline{e}\cdot\nabla\underline{v}) \cdot \underline{e}$$

$$\frac{dp_{\perp}}{dt} = -2p_{\perp}\nabla \cdot \underline{v} + p_{\perp}(\underline{e}\cdot\nabla\underline{v})\,\underline{e}$$

Furthermore, $\underline{E} + \underline{v} \times \underline{B} = 0$, and we have the magnetohydrodynamic approximation for Maxwell's equations,

$$\nabla \times \underline{E} = -\frac{\partial \underline{B}}{\partial t}, \quad \nabla \times \underline{B} = \underline{j}, \quad \nabla \cdot \underline{B} = 0$$

An energy principle for investigating the stability of static equilibrium states can be obtained from this description (2). We shall confine ourselves to instabilities that are excited by initial perturbations of the fluid which are limited to a finite region of the plasma, that is, they vanish outside that region and on its boundaries. It is clear that in an unbounded plasma, all instabilities will be of this type.

The energy principle for this case can be stated: A static equilibrium state is unstable if, and only if, there exists a perturbation $\underline{\xi}(\underline{r})$ and a volume V such that (a) $\underline{\xi}(\underline{r}) = 0$ outside and on the boundaries of V; and (b) the change in potential energy of the system δW caused by this perturbation is negative. The energy variation δW is given by

$$\delta W = \frac{1}{2}\int_V d\tau\Big\{\underline{Q}^2 - \underline{j}\cdot(\underline{Q}\times\underline{\xi}) + \frac{5}{3}p_{\perp}(\nabla\cdot\underline{\xi})^2 + \nabla\cdot\underline{\xi}(\underline{\xi}\cdot\nabla p_{\perp}) + \frac{1}{3}p_{\perp}(\nabla\cdot\underline{\xi} - 3q)^2 - q\nabla\cdot(\underline{\xi}\Delta p)$$

$$+\Delta p[(\underline{e}\cdot\nabla\underline{\xi})^2 - 4q^2] + \Delta p[(\underline{e}\cdot\nabla\underline{\xi})\cdot(\nabla\underline{\xi}\cdot\underline{e}) - (\underline{\xi}\cdot\nabla\underline{e})\cdot(\nabla\underline{\xi}\cdot\underline{e}) - (\underline{\xi}\cdot\nabla\underline{e})\cdot(\underline{e}\cdot\nabla\underline{\xi})]\Big\} \tag{1}$$

where

$$\underline{Q} = \nabla \times (\underline{\xi}\times\underline{B}) \tag{2}$$

and

$$q = (\underline{e}\cdot\nabla\underline{\xi}) \cdot \underline{e} \tag{3}$$

In Eqs. 1-3 all quantities have their unperturbed values (except for $\underline{\xi}$, of course).

The conditions for instability for constant $\underline{B}$ and $\underline{\underline{P}}$ were discussed previously (1). The result is that the plasma is unstable if, and only if,

$$\Delta p + B^2 < 0 \quad \text{or} \quad 3p_{||} - \frac{p_{\perp}^2}{B^2 + 2p_{\perp}} < 0 \tag{4}$$

This result does depend on the magnitude of the volume V. It therefore follows that in the nonuniform case condition 4 remains a sufficient condition for instability. This follows from the fact that if condition 4 is satisfied somewhere in the region under

consideration and we choose V around this point and make it small, then the plasma in V can be treated as uniform. Hence, in the nonuniform case it is sufficient to investigate the stability when condition 4 is not satisfied; that is, when

$$\Delta p + B^2 \geqslant 0 \quad \text{and} \quad 3p_{\parallel} - \frac{p_{\perp}^2}{B^2 + 2p_{\perp}} \geqslant 0 \qquad \text{everywhere} \tag{5}$$

so that eventual instabilities are not of the "uniform" type, but depend upon the nonuniformity of the equilibrium state.

c. Transformation of δW

As given in Eq. 1 δW is not very symmetric in material and magnetic pressures. By separating from the integrand certain divergence terms that do not make any contribution to the integral, it is possible to obtain greater symmetry. We shall now proceed to do this.

We have by direct computation

$$\begin{aligned}
\underline{Q}^2 - \underline{j} \cdot (\underline{Q} \times \underline{\xi}) = {} & B^2(\underline{e}\cdot\nabla\underline{\xi})^2 + B^2(\nabla\cdot\underline{\xi})^2 - 2B^2(\nabla\cdot\underline{\xi})\, q + \nabla \cdot \underline{\xi}\left(\underline{\xi} \cdot \nabla \frac{B^2}{2}\right) \\
& + \left[-q\underline{\xi} \cdot \nabla \frac{B^2}{2} - (\underline{\xi}\cdot\underline{e})(\underline{e}\cdot\nabla\underline{\xi}) \cdot \left(\nabla \frac{B^2}{2}\right) + (\underline{\xi}\cdot\nabla\underline{e}) \cdot \left(\nabla \frac{B^2}{2}\right)(\underline{\xi}\cdot\underline{e})\right. \\
& \left. + \left(\underline{e} \cdot \nabla \frac{B^2}{2}\right)(\underline{\xi}\cdot\underline{e})(\nabla\cdot\underline{\xi}) + (\underline{e}\cdot\nabla B)(\underline{\xi}\cdot\nabla B)(\underline{\xi}\cdot\underline{e})\right] \\
& - B^2(\underline{e}\cdot\nabla\underline{\xi})(\underline{\xi}\cdot\nabla\underline{e}+\nabla\underline{e}\cdot\underline{\xi}) + B^2\underline{\xi} \cdot (\nabla\underline{e}) \cdot (\nabla\underline{e}) \cdot \underline{\xi} \\
& + B^2(\nabla\cdot\underline{\xi})(\underline{e}\cdot\nabla\underline{e}) \cdot \underline{\xi} + \left(\underline{\xi} \cdot \nabla \frac{B^2}{2}\right)(\underline{e}\cdot\nabla\underline{e}) \cdot \underline{\xi}
\end{aligned} \tag{6}$$

We introduce the transformation:

$$\begin{aligned}
& -q\underline{\xi} \cdot \nabla \frac{B^2}{2} - (\underline{\xi}\cdot\underline{e})(\underline{e}\cdot\nabla\underline{\xi}) \cdot \left(\nabla \frac{B^2}{2}\right) + (\underline{\xi}\cdot\nabla\underline{e}) \cdot \left(\nabla \frac{B^2}{2}\right)(\underline{\xi}\cdot\underline{e}) + \left(\underline{e} \cdot \nabla \frac{B^2}{2}\right)(\underline{\xi}\cdot\underline{e})(\nabla\cdot\underline{\xi}) \\
& + (\underline{e}\cdot\nabla B)(\underline{\xi}\cdot\nabla B)(\underline{\xi}\cdot\underline{e}) = \nabla \cdot \left[(\underline{\xi}\cdot\underline{e})(\underline{e}\times\underline{\xi}) \times \nabla \frac{B^2}{2}\right] + \underline{e} \cdot \nabla\underline{e} \cdot \underline{\xi}\left(\underline{\xi} \cdot \nabla \frac{B^2}{2}\right) \\
& \qquad - \left(\underline{e} \cdot \nabla \frac{B^2}{2}\right)\underline{\xi} \cdot \nabla(\underline{\xi}\cdot\underline{e})
\end{aligned} \tag{7}$$

This can be verified by letting the operator ∇ in the first term on the right-hand side act on each factor separately, and using the equation

$$\nabla \cdot \underline{e} = -\frac{1}{B}\,\underline{e} \cdot \nabla B$$

that follows from $\nabla \cdot \underline{B} = 0$.

By substituting Eq. 7 in Eq. 6, we get

$$\underline{Q}^2 - \underline{j} \cdot (\underline{Q} \times \underline{\xi}) = B^2(\underline{e}\cdot\nabla\underline{\xi})^2 + B^2(\nabla\cdot\underline{\xi})^2 - 2B^2(\nabla\cdot\underline{\xi})\, q$$

$$+ (\nabla\cdot\underline{\xi})\left(\underline{\xi} \cdot \nabla \frac{B^2}{2}\right) + \nabla \cdot \left[(\underline{\xi}\cdot\underline{e})(\underline{e}\times\underline{\xi}) \times \nabla \frac{B^2}{2}\right]$$

$$- B^2(\underline{e}\cdot\nabla\underline{\xi})(\underline{\xi}\cdot\nabla\underline{e}+\nabla\underline{e}\cdot\underline{\xi}) + B^2\underline{\xi} \cdot (\nabla\underline{e}) \cdot (\nabla\underline{e}) \cdot \underline{\xi}$$

$$- \underline{e} \cdot \nabla\left(\frac{B^2}{2}\right) \underline{\xi} \cdot \nabla(\underline{\xi}\cdot\underline{e}) + \nabla \cdot (B^2\underline{\xi})\, \underline{e} \cdot (\nabla\underline{e}) \cdot \underline{\xi} \qquad (8)$$

Now, we introduce the transformation:

$$-q\nabla \cdot (\underline{\xi}\Delta p) + \Delta p[(\underline{e}\cdot\nabla\underline{\xi})\cdot(\nabla\underline{\xi}\cdot\underline{e})-(\underline{\xi}\cdot\nabla\underline{e})\cdot(\nabla\underline{\xi}\cdot\underline{e})-(\underline{\xi}\cdot\nabla\underline{e})\cdot(\underline{e}\cdot\nabla\underline{\xi})]$$

$$= -\nabla \cdot [\Delta p(\underline{e}\times\underline{\xi})\times\nabla(\underline{\xi}\cdot\underline{e})] - \Delta p(\underline{e}\cdot\nabla\underline{\xi})(\underline{\xi}\cdot\nabla\underline{e}+\nabla\underline{e}\cdot\underline{\xi})$$

$$+ \Delta p\underline{\xi} \cdot (\nabla\underline{e}) \cdot (\nabla\underline{e}) \cdot \underline{\xi} - \underline{e} \cdot \nabla(\Delta p)[\underline{\xi}\cdot\nabla(\underline{\xi}\cdot\underline{e})]$$

$$+ \nabla \cdot (\underline{\xi}\Delta p)\, \underline{e} \cdot (\nabla\underline{e}) \cdot \underline{\xi} - \Delta p\underline{\xi} \cdot \nabla(\underline{\xi}\cdot\nabla(\underline{\xi}\cdot\underline{e}))\,(\nabla\cdot\underline{e}) \qquad (9)$$

Equation 9 can be verified in the same way as Eq. 8. If we substitute Eqs. 8 and 9 in Eq. 1, we get

$$\delta W = \frac{1}{2}\int_V d\tau \left\{B^2(\underline{e}\cdot\nabla\underline{\xi})^2 + B^2(\nabla\cdot\underline{\xi})^2 - 2B^2(\nabla\cdot\underline{\xi})\, q + \frac{5}{3}\, p_\perp (\nabla\cdot\underline{\xi})^2 + \frac{1}{3}\, p_\perp (\nabla\cdot\underline{\xi}-3q)^2\right.$$

$$+ \Delta p[(\underline{e}\cdot\nabla\underline{\xi})^2-4q^2] + \nabla \cdot \left[(\underline{e}\times\underline{\xi}) \times \left((\underline{\xi}\cdot\underline{e})\, \nabla \frac{B^2}{2} - \Delta p\nabla(\underline{\xi}\cdot\underline{e})\right)\right]$$

$$- (B^2+\Delta p)(\underline{e}\cdot\nabla\underline{\xi})(\underline{\xi}\cdot\nabla\underline{e}+\nabla\underline{e}\cdot\underline{\xi}) + (B^2+\Delta p)(\underline{\xi}\cdot\nabla\underline{e}) \cdot (\nabla\underline{e}\cdot\underline{\xi})$$

$$+ \nabla \cdot (\underline{\xi}(B^2+\Delta p))\, \underline{e} \cdot (\nabla\underline{e}) \cdot \underline{\xi} - \left[\underline{e} \cdot \nabla\left(\frac{B^2}{2} + \Delta p\right) + \Delta p\nabla \cdot \underline{e}\right](\underline{\xi}\cdot\nabla(\underline{\xi}\cdot\underline{e}))$$

$$\left. + (\nabla\cdot\underline{\xi})\left(\underline{\xi} \cdot \nabla\left(p_\perp + \frac{B^2}{2}\right)\right)\right) \qquad (10)$$

By using $\nabla \cdot \underline{e} = -\frac{1}{B}\, \underline{e} \cdot \nabla B$, the equation

$$\underline{e} \cdot \nabla\left(\frac{B^2}{2} + p_\perp\right) + \Delta p(\nabla\cdot\underline{e}) = \frac{1}{2}\, \underline{e} \cdot \nabla(B^2+\Delta p) + \frac{1}{2}\, B^2\, \underline{e} \cdot \nabla \frac{\Delta p}{B^2} \qquad (11)$$

is easily verified. The equilibrium condition gives

$$\nabla\left(p_\perp + \frac{B^2}{2}\right) = \nabla \cdot [(B^2+\Delta p)\underline{e}\,\underline{e}] \tag{12}$$

If we substitute Eqs. 11 and 12 in Eq. 10 and use the symbols

$$B'^2 = B^2 + \Delta p$$

$$p' = p_\perp - \frac{1}{2}\Delta p = \frac{1}{2}(p_{||} + p_\perp)$$

we get

$$\begin{aligned}\delta W = \frac{1}{2}\int_V d\tau \Big\{ & B'^2(\underline{e}\cdot\nabla\underline{\xi})^2 + B'^2(\nabla\cdot\underline{\xi})^2 - 2B'^2(\nabla\cdot\underline{\xi})\,q + \frac{5}{3}\,p'(\nabla\cdot\underline{\xi})^2 + \frac{1}{3}\,p'(\nabla\cdot\underline{\xi}-3q)^2 \\ & + \Delta p\left[(\nabla\cdot\underline{\xi})\,q - \frac{5}{2}q^2\right] - B'^2(\underline{e}\cdot\nabla\underline{\xi})(\underline{\xi}\cdot\nabla\underline{e}+\nabla\underline{e}\cdot\underline{\xi}) \\ & + B'^2(\underline{\xi}\cdot\nabla\underline{e})\cdot(\nabla\underline{e}\cdot\underline{\xi}) + \nabla\cdot(\underline{\xi}B'^2)(\underline{e}\cdot\nabla\underline{e})\cdot\underline{\xi} + (\nabla\cdot\underline{\xi})\,\nabla\cdot(B'^2\underline{e}\,\underline{e})\cdot\underline{\xi} \\ & - \left(\frac{1}{2}\,\underline{e}\cdot\nabla B'^2 + \frac{B^2}{2}\,\underline{e}\cdot\nabla\frac{\Delta p}{B^2}\right)(\underline{\xi}\cdot\nabla(\underline{\xi}\cdot\underline{e}))\end{aligned} \tag{13}$$

Note that the divergence term in the integrand in Eq. 10 does not make any contribution to the integral. We see also that $B'^2 \geq 0$ because of Eq. 5.

d. Discussion of Static Equilibrium States

The equilibrium condition is

$$\nabla\cdot\left(\left(p_\perp + \frac{B^2}{2}\right)\underline{\underline{I}} - (B^2+\Delta p)\underline{e}\,\underline{e}\right) = 0$$

It is convenient to distinguish between two classes of equilibrium states:

Class 1. Those for which

$$\underline{e}\cdot\nabla\left(\frac{\Delta p}{B^2}\right) = 0 \qquad \text{everywhere} \tag{14}$$

Class 2. Those for which

$$\underline{e}\cdot\nabla\left(\frac{\Delta p}{B^2}\right) \neq 0 \qquad \text{somewhere} \tag{15}$$

Condition 14 is equivalent to the condition

$$\nabla\cdot\underline{B}' = 0 \tag{16}$$

where $\underline{B}' = B'\underline{e}$. This can be shown in the following way: $\underline{e}\cdot\nabla(\Delta p/B^2) = \underline{e}\cdot\nabla(B'/B)^2 = 0$,

which gives $\underline{e} \cdot \nabla(B'/B) = 0$. If we use the equation $\underline{e} \cdot \nabla B = -B\nabla \cdot \underline{e}$, it follows readily that $\nabla \cdot \underline{B}' = 0$. The converse is also easy to prove.

The equilibrium condition can be written

$$\nabla \cdot \left[\left(p' + \frac{B'^2}{2}\right)\underline{\underline{I}} - B'^2\,\underline{e}\,\underline{e}\right] = 0 \tag{17}$$

This is the same equilibrium condition that we would have for a fluid with isotropic pressure p' in a magnetic field $\underline{B}'$. From Eqs. 16 and 17 and from the fact that $B'^2 \geqslant 0$, it follows that to each anisotropic equilibrium state of class 1 we can find an "associated" isotropic equilibrium state with pressure p' and magnetic field $\underline{B}'$. Conversely, it is easy to find anisotropic equilibrium states of class 1 from isotropic ones. Let $\underline{B}'$ and p' be the magnetic field and isotropic pressure, respectively, in a given equilibrium state. We can then construct a series of anisotropic equilibrium states by defining a Δp such that $\underline{e} \cdot \nabla(\Delta p/B'^2) = 0$ everywhere, and set $B^2 = B'^2 - \Delta p$, $\underline{B} = B\underline{e}$, $p_\perp = p' + \frac{1}{2}\Delta p$, and $p_\parallel = p' - \frac{1}{2}\Delta p$. Hence, there exists a simple relationship between the possible anisotropic equilibrium states of class 1 and the possible isotropic states.

e. The Stability of Equilibrium States for Which $\underline{e} \cdot \nabla\left(\frac{\Delta p}{B^2}\right) = 0$ (Class 1)

For equilibrium states of Class 1, the term containing $\underline{e} \cdot \nabla(\Delta p/B^2)$ in Eq. 13 vanishes. We get

$$\delta W = \delta W' + \frac{1}{2}\int_V dt\, \Delta p\left[(\nabla \cdot \underline{\xi})\, q - \frac{5}{2}q^2\right] \tag{18}$$

where $\delta W'$ is the energy variation of the associated isotropic state.

We see that δW has been split into two terms: $\delta W'$ referring to the energy variation of the associated isotropic state, and a "uniform" term containing Δp but not the derivatives of $\underline{\underline{P}}$ and $\underline{B}$. The latter term is therefore present also for the uniform equilibrium states. The effect of pressure anisotropy on a nonuniform equilibrium state can hence be taken into account by taking the energy variation of the associated isotropic equilibrium state and adding a uniform correction term containing Δp.

We are therefore led to the conclusion that the complications introduced by nonuniformity on anisotropic equilibrium states can be described by an associated isotropic equilibrium state, and that the total effect of pressure anisotropy and nonuniformity does not lead to any new types of instability that are not already present in the uniform, anisotropic, and in the isotropic, nonuniform equilibrium states.

We shall now use Eq. 18 to establish some simple comparison criteria for stability. Let $\delta W' = \delta W'_{B'} + \delta W'_{p'}$, where $\delta W'_{B'}$ contains all terms in $\delta W'$ that contain B', and likewise for $\delta W'_{p'}$ and p'. We have

$$\delta W_{p'} = \frac{1}{2}\int_V d\tau\left\{\frac{5}{3}p'(\nabla\cdot\underline{\xi})^2 + \frac{1}{3}p'(\nabla\cdot\underline{\xi}-3q)^2\right\}$$

We substitute the transformation

$$(\nabla\cdot\underline{\xi})\, q - \frac{5}{2}\, q^2 = -\frac{1}{6}\,(\nabla\cdot\underline{\xi}-3q)^2 + \frac{1}{6}\,(\nabla\cdot\underline{\xi})^2 - q^2$$

in Eq. 18 and get

$$\delta W = \delta W'_{B'} + \frac{1}{2}\int_V d\tau\left\{\frac{5}{3}\left(p' + \frac{1}{10}\Delta p\right)(\nabla\cdot\underline{\xi})^2 + \frac{1}{3}\left(p' - \frac{1}{2}\Delta p\right)(\nabla\cdot\underline{\xi}-3q)^2 - \Delta p q^2\right\}$$

Now, if $\Delta p > 0$ and $(\Delta p)_{max}$ is its maximum value in the region considered, we see that

$$\delta W \leqslant \frac{1}{2}\int_V d\tau\left\{\frac{5}{3}\left(p' + \frac{1}{10}(\Delta p)_{max}\right)(\nabla\cdot\underline{\xi})^2 + \frac{1}{3}\left(p' + \frac{1}{10}(\Delta p)_{max}\right)(\nabla\cdot\underline{\xi}-3q)^2\right\}$$

$$= \delta W'_{B'} + \delta W'_{p''} \qquad p'' = p' + \frac{1}{10}\,(\Delta p)_{max}$$

Hence, if $\Delta p > 0$, the anisotropic equilibrium state is less stable than the associated isotropic equilibrium state when $\frac{1}{10}\,(\Delta p)_{max}$ is added to the isotropic pressure p'.

Likewise, when $\Delta p < 0$,

$$\delta W \geqslant \delta W'_{B'} + \delta W'_{p'''} \qquad p''' = p' - \frac{1}{10}\,|\Delta p|_{max}$$

which means that the anisotropic state is more stable than the associated isotropic state when $\frac{1}{10}\,|\Delta p|_{max}$ is subtracted from the isotropic pressure p'.

The investigation of the stability of Class 2 states is more complicated for two reasons. First, due to the fact that $\nabla \cdot \underline{B}'$ no longer vanishes, the $\delta W'$ in Eq. 18 no longer refers to a possible isotropic equilibrium state. Second, we get the extra term containing $\underline{e} \cdot \nabla(\Delta p/B^2)$ in the energy-variation integral, which may be expected to give rise to essentially new types of instability associated with the combined effect of non-uniformity and anisotropy. It is interesting to note that this term can be written $B'\Delta \cdot B'$.

K-F. Voyenli

References

1. K-F. Voyenli, Quarterly Progress Report No. 60, Research Laboratory of Electronics, M.I.T., Jan. 15, 1961, pp. 17-24.

2. I. Bernstein, E. A. Frieman, M. D. Kruskal, and R. M. Kulsrud, An energy principle for hydromagnetic stability problems, Proc. Roy. Soc. (London) A244, 17-40 (1958).

II-B. PLASMA ELECTRONICS*

Prof. L. D. Smullin
Prof. H. A. Haus
Prof. A. Bers
Prof. D. J. Rose
P. Chorney
J. R. Cogdell
L. J. Donadieu
T. H. Dupree
T. J. Fessenden
W. D. Getty
H. Y. Hsieh
P. W. Jameson
W. Larrabee IV
L. M. Lidsky
D. L. Morse
S. D. Rothleder
A. J. Schneider
P. E. Serafim
A. W. Starr
M. C. Vanwormhoudt
R. C. Wingerson
S. Yoshikawa

1. BIDIRECTIONAL WAVEGUIDES

a. General Classification

In Quarterly Progress Report No. 60 a general class of waveguides, which we called bidirectional, was introduced. The materials contained in these waveguides were characterized by the gyrotropic tensors given by Eqs. 11 and 12 in that report (1). It turns out that the classification "bidirectional waveguide" may be extended to include many more systems, if we express the permittivity and permeability tensors in a more general form.

We now characterize these tensors by the forms

$$\bar{\bar{\epsilon}}(x,y) = \begin{bmatrix} \epsilon_{11} & \epsilon_{12} & 0 \\ \epsilon_{21} & \epsilon_{22} & 0 \\ 0 & 0 & \epsilon_{33} \end{bmatrix} \tag{1}$$

$$\bar{\bar{\mu}}(x,y) = \begin{bmatrix} \mu_{11} & \mu_{12} & 0 \\ \mu_{21} & \mu_{22} & 0 \\ 0 & 0 & \mu_{33} \end{bmatrix} \tag{2}$$

All of the elements of the tensors may be complex, and the tensor need not be restricted to lossless media. For lossless, passive media, all of the diagonal terms are pure real, and the off-diagonal terms are complex conjugates of each other. For lossless, passive, gyrotropic media, the off-diagonal terms are pure imaginary.

Besides the waveguide systems mentioned in Quarterly Progress Report No. 60, we may now include as specific examples of bidirectional waveguides: (a) those containing anisotropic single crystals with an axis of symmetry along the waveguide axis, and (b) those containing polycrystalline materials with a preferred orientation along the waveguide axis because of mechanical stresses.

---

*This work was supported in part by National Science Foundation under Grant G-9330.

b. Proof of Bidirectionality

The proof of bidirectionality that is based on the work of Villeneuve (2) applies only to gyrotropic media. We shall show that waveguides whose media are characterized by the more general tensors given by Eqs. 1 and 2 are bidirectional. Consider a uniform

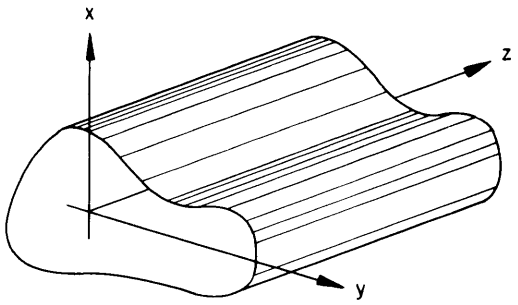

Fig. II-7. Uniform waveguide with general cross section.

waveguide of arbitrary cross section (Fig. II-7). The waveguide walls may be composed of perfect electric conductors, perfect magnetic conductors, or both. The boundary conditions at the walls are

$$\bar{n} \times \bar{\bar{E}} = 0 \tag{3}$$

on perfect electric conductors, and

$$\bar{n} \times \bar{\bar{H}} = 0 \tag{4}$$

on perfect magnetic conductors. Here, $\bar{n}$ is the unit normal vector at the waveguide wall. The fields in this waveguide are governed by Maxwell's equations:

$$\nabla \times \bar{\bar{H}} = j\omega \bar{\bar{\epsilon}} \cdot \bar{\bar{E}} \tag{5}$$

$$\nabla \times \bar{\bar{E}} = -j\omega \bar{\bar{\mu}} \cdot \bar{\bar{H}} \tag{6}$$

These equations may be separated into transverse and longitudinal components with the following results:

$$\nabla_T \hat{H}_z + \Gamma \hat{H}_T = j\omega \bar{i}_z \times \bar{\bar{\epsilon}}_T \cdot \hat{E}_T \tag{7}$$

$$\nabla_T \hat{E}_z + \Gamma \hat{E}_T = -j\omega \bar{i}_z \times \bar{\bar{\mu}}_T \cdot \hat{H}_T \tag{8}$$

$$\bar{i}_z \cdot (\nabla_T \times \hat{H}_T) = j\omega \epsilon_{33} \hat{E}_z \tag{9}$$

$$\bar{i}_z \cdot (\nabla_T \times \hat{E}_T) = -j\omega\mu_{33}\hat{H}_z \tag{10}$$

The z-dependence of all field quantities has been assumed to be $\exp(-\Gamma z)$. The circumflex denotes that a field quantity is independent of z. The notation previously used — that of underlining complex quantities — has been dropped; all quantities are to be understood as generally complex. The subscripts T and z denote transverse and longitudinal components, respectively. The 2×2 subtensors that contain the transverse elements of the permittivity and permeability tensors are also denoted by the subscript T.

We note that if we replace Γ by $-\Gamma$, $\hat{E}_T$ by $\mp\hat{E}_T$, $\hat{H}_T$ by $\pm\hat{H}_T$, $\hat{E}_z$ by $\pm\hat{E}_z$, and $\hat{H}_z$ by $\mp\hat{H}_z$, then Eqs. 7-10 remain unchanged; and the boundary conditions, Eqs. 3 and 4, of course, remain unchanged. Thus we conclude that the dispersion relation for Γ is the same as that for $-\Gamma$; that is, the dispersion relation must be an even function of Γ. Hence, if a wave propagates as $\exp(-\Gamma z)$, it is possible to excite another wave having the same basic field structure that propagates as $\exp(+\Gamma z)$. This statement is the basic definition of the property of bidirectionality. We recall that the only restriction that makes this waveguide system bidirectional is the form of the permittivity and permeability tensors given by Eqs. 1 and 2. The relations previously derived (1) for lossless, passive, bidirectional waveguides still apply to systems with media characterized by Eqs. 3 and 4 in lossless, passive form.

c. Some General Properties of Plasma-Filled Waveguides

As an illustration of the implications of the relations already derived, we shall apply them to a waveguide that is completely filled with a uniform, cold, collisionless, longitudinally magnetized plasma. The cross section is arbitrary, and the elements of the permittivity tensor are given by

$$\epsilon_{11} = \epsilon_{22} = \epsilon_o\left[1 + \frac{\omega_p^2}{\omega_c^2 - \omega^2}\right] \tag{11}$$

$$\epsilon_{12} = \epsilon_{21}^* = -j\epsilon_o \frac{\omega_c}{\omega}\frac{\omega_p^2}{\omega_c^2 - \omega^2} \tag{12}$$

$$\epsilon_{33} = \epsilon_o\left[1 - \frac{\omega_p^2}{\omega^2}\right] \tag{13}$$

The motion of the plasma ions is neglected. The permeability tensor becomes the scalar μ_o. We must bear in mind that for such a waveguide system, the modes do not separate into TE and TM solutions; in general, they simultaneously possess both

transverse and longitudinal components of the E- and H-fields (3, 4, 5). Thus we have all of the pseudo-energy quantities – U_{eT}, U_{mT}, U_{ez}, and U_{mz}.

We note that ϵ_3 is negative for $\omega < \omega_p$ and positive for $\omega > \omega_p$; thus U_{ez} is negative for $\omega < \omega_p$ and positive for $\omega > \omega_p$. Now, U_{mT} and W are always positive, since it can be shown that $\bar{\bar{\epsilon}}_\omega$ is a positive definite quadratic form. Since U_{ez} is negative for $\omega < \omega_p$ and U_{mT} is always positive, the quantity $U_{mT} - U_{ez}$ is always positive for $\omega < \omega_p$, and we conclude (6) that if β exists for $\omega < \omega_p$, then

$$\frac{\partial \beta}{\partial \omega} > 0 \tag{14}$$

That is to say, $\beta(\omega)$ always has a positive slope for $\omega < \omega_p$. This result is indeed substantiated by quasi-static solutions (7, 8) and by the curves of Schumann (9).

Next, we consider the possibility of the existence of complex propagation constants. We note from the previous report (10) the necessary pseudo-energy relations that must be satisfied when complex roots exist,

$$\left.\begin{aligned} U_T &= U_z \\ U_m &= U_e \end{aligned}\right\} \tag{15}$$

This pair of expressions can be manipulated to give an equivalent pair

$$\left.\begin{aligned} U_{eT} &= U_{mz} \\ U_{mT} &= U_{ez} \end{aligned}\right\} \tag{16}$$

which must be simultaneously satisfied for complex Γ. Now, since U_{ez} is negative for $\omega < \omega_p$ and positive for $\omega > \omega_p$, and U_{mT} is always positive, we conclude that if complex propagation constants exist, they must occur for $\omega > \omega_p$.

On the basis of the theorems previously derived, it is also possible to deduce the field structure of the wave for particular conditions. Suppose we have a cutoff $\beta = 0$, for some frequency ω_o that is such that $0 < \omega_o < \omega_p$. Then at the cutoff frequency ω_o the psuedo-energy conditions that must be met are the same as those (11) given by Eq. 16. We conclude that at this cutoff frequency a longitudinal E-field cannot exist because if it existed U_{ez} would be negative, and U_{mT} is always positive. Consequently, the transverse H-field vanishes and the field is composed of merely a longitudinal H-field and a transverse E-field. That this is true can be shown from the exact field solution (3, 4, 5).

Other results may be derived from these theorems. One that poses an interesting question will now be discussed. Some recent computations performed by Wang and Hopson (12) indicate that $\partial\beta/\partial\omega = \infty$, for finite β, under certain conditions. A dispersion relation showing this behavior is sketched in Fig. II-8; the frequency at which $\partial\beta/\partial\omega = \infty$ is denoted ω_∞. The modes under consideration are the circularly symmetric ones that

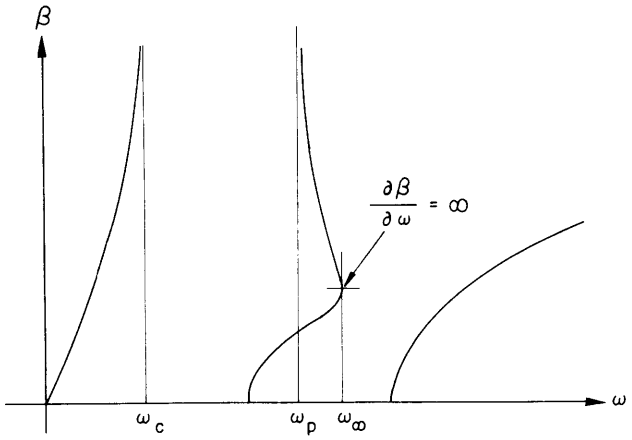

Fig. II-8. Sketch of nonquasi-static plasma-waveguide dispersion.

occur in a plasma-filled circular waveguide; they do not exhibit Faraday rotation because of their degenerate symmetry. It seems that this behavior ($\partial\beta/\partial\omega=\infty$) is exhibited when the cutoff frequency of the empty-waveguide TM_{01} mode becomes comparable to, or less than, either ω_p or ω_c.

At the frequency ω_∞ we have the pseudo-energy relations given by Eqs. 15 and 16; these are the same as those needed for complex propagation constants. This conclusion

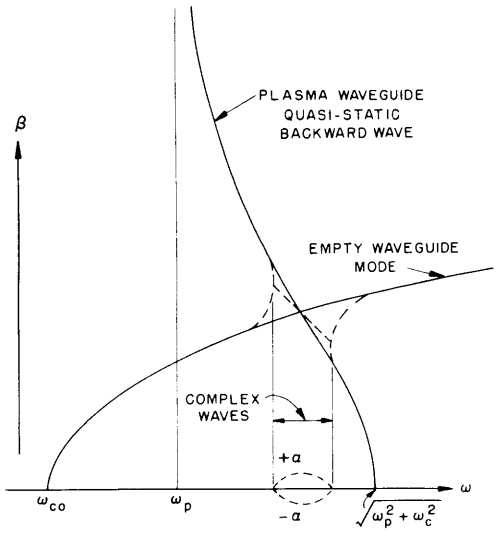

Fig. II-9. Weak coupling of empty-waveguide mode with quasi-static plasma-waveguide backward wave. (ω_{co} is the cutoff frequency of the empty-waveguide TM mode.)

is based on previous work (13); we must have $U_T = U_z$ in order that $\partial\beta/\partial\omega = \infty$, for finite β and finite energy storage W. We now pose the question, Is this the onset of complex propagation constants? Apparently, only direct computation can completely answer this question and, to the author's knowledge, such computations have not been

performed. But an argument based on the nature of mode coupling (14) indicates that this is the onset of complex roots. The modes that are coupled are the backward-wave, obtained from quasi statics (7, 8), and the empty-waveguide mode whose cutoff frequency is less than, say, the plasma frequency. The coupling of modes is sketched in Fig. II-9. The originally unperturbed separate modes are indicated by solid lines. The perturbations arising from mode coupling are indicated by broken lines. In the region where the two unperturbed modes are synchronous, complex waves are shown. The imaginary part of Γ (i.e., β), is approximately the arithmetic mean between the two unperturbed modes, according to the theory of weak coupling. The values of the real parts $\pm\alpha$ are small compared with β for weak coupling.

These modes, according to the theory of coupling of modes, couple to give complex roots. However, we invoke this principle in a heuristic manner — the coupling-of-modes theory cannot be used to obtain quantitative results, since it is a first-order theory and hence applies to weak coupling and, obviously, we have very strong coupling. But from both approaches — the pseudo-energy theorems and coupling of modes — there is a strong suspicion that the plasma-filled waveguide exhibits complex propagation constants.

P. Chorney

References

1. P. Chorney, Power, energy, group velocity, and phase velocity in bidirectional waveguides, Quarterly Progress Report No. 60, Research Laboratory of Electronics, M. I. T., Jan. 15, 1961, pp. 37-46.

2. A. T. Villeneuve, Orthogonality relationships for waveguides and cavities with inhomogeneous anisotropic media, Trans. IRE, vol. MTT-7, pp. 441-446, October 1959.

3. H. Gamo, The Faraday rotation of waves in a circular waveguide, J. Phys. Soc. Japan 8, 176-182 (1953).

4. A. A. Th. M. Van Trier, Guided electromagnetic waves in anisotropic media, Appl. Sci. Research B3, 305-371 (1953).

5. H. Suhl and L. R. Walker, Topics in guided-wave propagation through gyromagnetic media. Part I. The completely filled cylindrical guide, Bell System Tech. J. 33, 579-659 (1954).

6. P. Chorney, op. cit., see especially Eq. 39, p. 42.

7. A. W. Trivelpiece and R. W. Gould, Space charge waves in cylindrical plasma columns, J. Appl. Phys. 30, 1784-1793 (1959).

8. L. D. Smullin and P. Chorney, Propagation in ion-loaded waveguides, Proceedings of the Symposium on Electronic Waveguides (Polytechnic Press, New York, April 1958), pp. 229-247.

9. W. O. Schumann, Über Wellenausbreitung in Plasma zwischen zwei unendlich gut Leitenden Ebenen in Richtung eines aufgeprägten äussern Magnetfeldes, Z. angew. Phys. 8, 482-485 (1956).

10. P. Chorney, op. cit., see Table II-1, p. 42.

(References continued on following page)

11. This follows from an examination of Eq. 26 in P. Chorney, op. cit., p. 40.

12. C. C. Wang and J. E. Hopson, Electromagnetic wave propagation in gyroelectric plasmas, Second Scientific Report on Contract No. AF19(604)-5555, Sperry Gyroscope Company, Great Neck, L. I., New York, April 1960.

13. P. Chorney, op. cit., see Eq. 39, p. 42.

14. J. R. Pierce, Coupling of modes of propagation, J. Appl. Phys. 25, 179-183 (1954).

2. ALFVÈN-WAVE AMPLIFIER

A part of the theoretical study on magnetohydrodynamic ac power generation is aimed at examining various kinds of interaction schemes that could be used for generation of power through interaction of magnetic fields with highly conducting moving plasmas. One of the results of this study is the Alfvèn-wave amplifier.

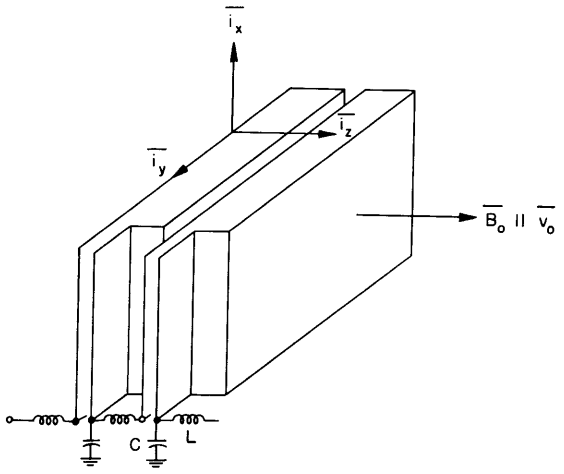

Fig. II-10. Schematic drawing of Alfvèn-wave amplifier.

A one-dimensional structure has been analyzed; it incorporates the circuit previously described (1) and a uniform plasma moving with a velocity v_o along the lines of a uniform dc magnetic field. The idealized one-dimensional geometry of this structure is shown in Fig. II-10. The magnetohydrodynamic equations of a perfectly conducting plasma are used. The ac excitation variables are split into time-average and time-variant components. The time-variant parts of the equations are subsequently linearized. The physical quantities that enter into the equations are shown in Table II-1. The directions of the vector quantities are indicated. The circuit equations are identical to those used before (1). The determinantal equation for an assumed time-space dependence of the form $\exp[j(\omega t-\beta z)]$ is

$$(\omega - v_o\beta)^2 = \beta^2 c_b^2 \left(1 + \frac{\beta_o^2 \frac{\mu_o}{L}}{\beta_o^2 - \beta^2} \right)$$

where β_o is the propagation constant of the circuit without the plasma, c_b is the Alfvèn velocity, $c_b^2 = B_o^2/(\mu_o \rho_o)$, and L is the external inductance of the circuit.

The circuit is effectively decoupled from the plasma in the limit $\mu_o/L \to 0$. Then we find the solutions $\beta = \pm\beta_o$, corresponding to the unperturbed circuit propagation constants,

Table II-1. Table of symbols.

Quantity	Time Average		Perturbation Amplitude	
	Symbol	Direction	Symbol	Direction
Mass Density	ρ_o	–	ρ	–
Velocity	v_o	z	v	x
Magnetic Field	B_o	z	B	x
Electric Field	–	–	E	y
Current Density	–	–	J	y

and $\beta = \omega/(v_o \pm c_b)$, corresponding to a fast and a slow wave in the plasma. In a frame of reference moving at the dc velocity of the plasma v_o, these are the well-known Alfvèn waves propagating in the +z and -z directions. For nonzero, but weak, coupling of the circuit to the plasma the interaction is appreciable only when the circuit wave is close to synchronism with either the slow or the fast wave. We may then set

$$\beta = \frac{\omega}{v_o \pm c_b} + \delta$$

and

$$\beta_o = \frac{\omega}{v_o \pm c_b} + b$$

with both b and δ small. The solutions are

$$\delta(\delta - b) = \pm \frac{\beta_o^3}{4\frac{\omega}{c_b}} \frac{\mu_o}{L}$$

The plus sign applies to coupling with the fast wave, the minus sign to coupling with the slow wave. When b = 0 and $v_o > c_b$, and thus $\beta_o > 0$, we find for coupling to the slow wave

$$\delta = \pm j \frac{\frac{\beta_o}{\omega}\frac{\mu_o}{L}}{c_b}$$

The two values of δ are pure imaginary and represent spatial growth and decay. The growth can be used as an amplification mechanism. This can be shown, either by matching the boundary conditions at the input of the amplifier, or from arguments based on a small-signal power theorem. It can be shown that the small-signal power propagating in the plasma is

$$P = \rho_o v_o \left(v^2 - v_o v \frac{B}{B_o} \right) - (vB_o - v_o B) \frac{B}{\mu_o}$$

$$= \rho_o v_o \left[v^2 - \left(1 + \frac{c_b^2}{v_o^2} \right) v_o v \frac{B}{B_o} + c_b^2 \left(\frac{B}{B_o} \right)^2 \right]$$

In terms of the velocity amplitudes v_+ and v_- of the fast and slow waves, respectively, the time-average power $\langle P \rangle$ in the fast and slow Alfvèn wave may be written as

$$\langle P \rangle = \pm \rho_o c_b \left\langle v_\pm^2 \right\rangle (1 + v_o)^2$$

The small-signal power is positive for the fast wave, and negative for the slow wave. Since, for $v_o > c_b$, the group velocity of the slow wave is positive and its power is negative, it may be concluded from coupling-of-modes theory (2) that the growing wave produced as the result of coupling of a circuit wave to the slow wave signifies a true amplification.

An interesting feature of the Alfvèn-wave amplifier is that the velocity of the plasma v_o has to be only greater than the Alfvèn velocity $B_o/(\mu_o \rho_o)^{1/2}$, and not greater than the combined Alfvèn and sound velocities, $\left(B_o^2/\mu_o \rho_o + \gamma p_o/\rho_o \right)^{1/2}$, as in the magnetohydrodynamic generator discussed in the last report (1). This raises the possibility of testing this effect experimentally by using liquid metals flowing at comparatively low velocities.

Another remarkable feature of the Alfvèn amplifier is that in the incompressible fluid case, the equations can be solved exactly — even for large signals. From such an analysis it is possible to determine what physical process accounts for the power transferred to the circuit. One finds that the power transfer is accounted for by a pressure drop from the input end to the output end of the amplifier. This pressure drop is of second order in the ac excitation amplitudes.

a. The Compression-Wave Magnetohydrodynamic Generator

The previously proposed ac generator (1) may be called a compression-wave generator because its operation depends on plasma waves with compression. The present work

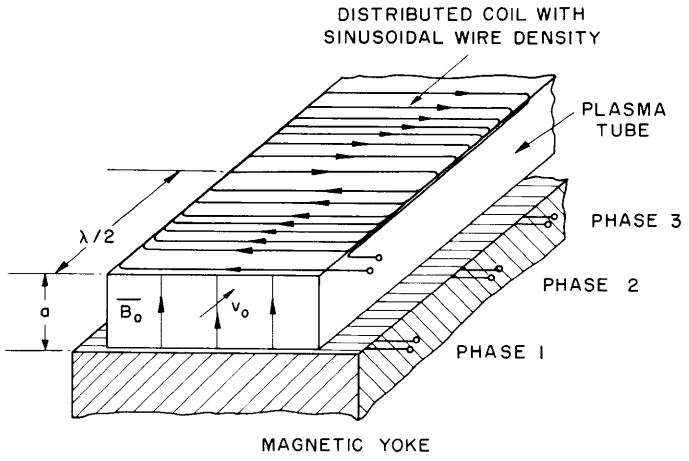

Fig. II-11. Geometry of compression-wave amplifier. (Two top windings removed.)

is aimed at finding an experimental structure of practicable size and power requirements for testing experimentally the predicted energy conversion in the compression-wave ac generator. An analysis has been carried out of a three-dimensional system from which quantitative information may be obtained for various envisaged experimental structures. A model is illustrated in Fig. II-11. It consists of a straight rectangular nonconducting tube in which the plasma flows. The top and bottom walls support two three-phase windings; one of which is shown idealized in Fig. II-11. The current in the top winding is in phase with that in the bottom winding. The windings are backed up by highly permeable magnetic yokes of zero conductivity. The following assumptions are made:

(a) The viscosity of the plasma is zero so that the boundary layers are of negligible thickness. The plasma in the tube flows at a uniform velocity v_o and is of uniform density.

(b) The conductivity of the plasma is infinite.

(c) The winding currents can be approximated by a surface current distribution.

(d) The thickness of the tube walls is negligible.

(e) The electrical length of the coil wires at the frequency of operation is small compared with a free-space wavelength.

Solutions are assumed that are periodic in z, with the periodicity λ of twice the winding width, and the complex frequency eigenvalues are sought, with each of the coils terminated in the load admittance $G + j\omega C$. Such a solution applies to a situation in which the plasma is confined in a tube of rectangular cross section that bends back on itself and in which the plasma flow lines are circular. Such a structure may prove useful for transient tests of the compression-wave ac generator. The solution with — what is believed to be — the fastest rate of growth is the solution that has the least dependence upon the x coordinate. For relatively slow rates of growth, the complicated

determinantal equation may be simplified to yield the complex frequency $\sigma + j\omega$, where $\omega = (v_o - c)\beta_z$, and

$$\frac{\sigma}{\omega} = +\frac{3}{4}\frac{c_b^2}{c^2}\left(\frac{\mu_o}{a}G\right)\frac{n_o^2\pi}{\beta_z^2}$$

Here, $\beta_z = 2\pi/\lambda$ is the z component of the propagation constant which is fixed by the dimensions of the three-phase winding;

$$c = \left(\frac{\gamma p_o}{\rho_o} + \frac{B_o^2}{\mu_o \rho_o}\right)^{1/2}$$

is the velocity of propagation of a one-dimensional compression wave;

$$c_b^2 = \frac{B_o^2}{\mu_o \rho_o}$$

is the Alfvèn velocity; n_o is the maximum wire density of any one of the three phase windings; and $\underline{a}$ is the height of the tube.

The remarkable conclusion of this study is that an instability, and therefore an oscillation, may be produced in this system by terminating the coils in resistances only. The technical problem of producing coupling to the plasma waves with attendant electromagnetic power generation is thus considerably simpler than originally expected when a slow-wave line incorporating large capacitors was envisaged.

H. A. Haus

References

1. H. A. Haus, Magnetohydrodynamic ac generators, Quarterly Progress Report No. 60, Research Laboratory of Electronics, M.I.T., Jan. 15, 1961, pp. 46-50.

2. J. R. Pierce, Coupling of modes of propagation, J. Appl. Phys. 25, 179 (1954).

3. LARGE-SIGNAL ELECTRON-STIMULATED PLASMA OSCILLATIONS

A pulsed, 10-kv, 1-amp, 2.5-μsec beam is injected into an electric field-free region, as shown in Fig. II-12. The apparatus is that used for the hollow-cathode discharge (1), except that a dc arc was not formed in these experiments. Gas (argon) was continuously injected through the arc cathode at a rate of several cc-atm/min and was removed by the vacuum pumps so that the pressure in the vacuum chamber was held at approximately 5×10^{-4} mm Hg, and the pressure in the gun chamber was approximately 10^{-5} mm Hg. The shape of the magnetic field $B_z(z)$ could be varied by separately exciting the two coils.

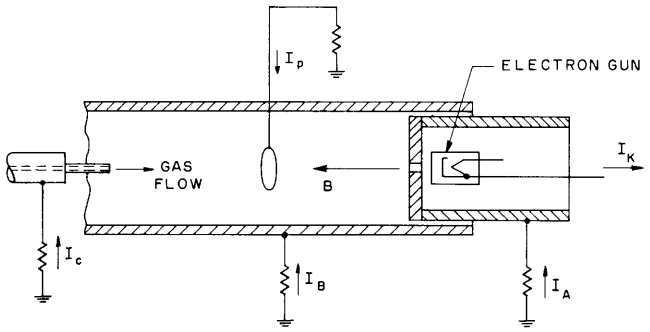

Fig. II-12. Schematic diagram of apparatus used in large-signal, electron-beam and plasma interaction experiment.

A typical value at the center of the region was 500 gauss. The currents collected by the arc cathode (I_c), the ring probe (I_p), and the walls of the vacuum chamber (I_B), and the current emitted by the electron gun (I_K) were observed on an oscilloscope. A photomultiplier tube was used to detect light emitted along the path of the beam and its output was also recorded. Figure II-13 shows the oscilloscope recordings of the various currents. Figure II-13a shows the behavior under vacuum conditions (no gas flow, and pressure approximately 10^{-6} mm Hg). Figure II-13b shows the corresponding currents with a gas flow of 5 cc-atm/min and a chamber pressure of approximately 4.5×10^{-4} mm Hg. The gun cathode current and accelerating voltage were held constant in these experiments. In Fig. II-13b a break is observed in the various collected currents 1.5 μsec after the start of the pulse. Coincident with this break is the sudden appearance of light, as indicated by the photomultiplier current. In Fig. II-13c, similar recordings are shown for which the gas flow was increased to 40 cc-atm/min, the pressure was increased to 6×10^{-4} mm Hg, and the exciting current of the coil nearest the electron gun was increased 90 per cent. A sharp break is observed in the collected currents approximately 1 μsec after the start of the pulse, and a sharp increase in the photomultiplier current is also observed. These breaks last approximately 0.1 μsec, after which the currents return to magnitudes that are nearly equal to their values before the break. A second break, which can be seen most clearly in the recording of I_p, occurs approximately 1.4 μsec later. Following the second break, the photomultiplier current oscillates about a high level, and I_c continues to oscillate for a few tenths of a microsecond.

As the magnitude of the exciting current in the coil nearest the gun is increased, while the gas flow rate is held constant at 5 cc-atm/min, the single break moves toward the trailing edge of the pulse. On the other hand, an increase of the flow rate while the coil current is held fixed causes the opposite effect. When the electrode used as a collector for I_c was biased approximately 100 volts positive with respect to the anode of

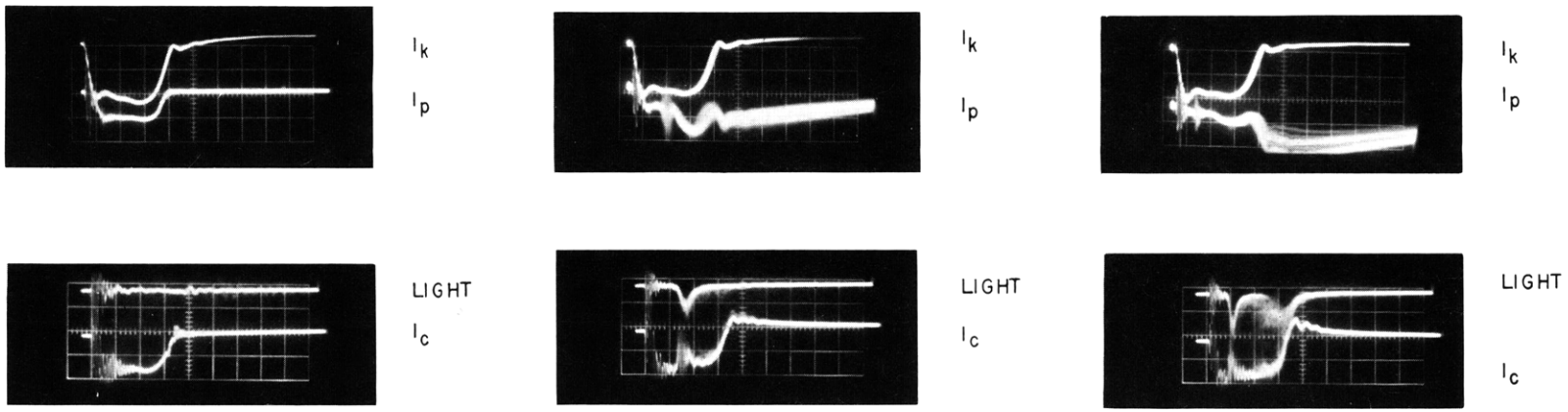

Fig. II-13. Oscilloscope records of the currents indicated in Fig. II-12 (electron-gun parameters: voltage, 10 kv; cathode current, 1 amp; pulse length, 2.5 μsec). The vertical calibration of each current photograph is 1 amp/cm. The time-axis calibration is 1 μsec/cm. Read time from left to right. (a) No flow; pressure 10^{-6} mm Hg. (b) Flow, 5 cc-atm/min; pressure, 5.4×10^{-4} mm Hg. (c) Flow, 40 cc-atm/min; pressure, 6×10^{-4} mm Hg.

the gun and the vacuum chamber, the sharp breaks in the collected currents were not present; the currents all behaved as in the vacuum case (Fig. II-13a), and no light was emitted.

From these experiments certain tentative conclusions can be drawn. (a) The breaks in the current pulses are due to an electron beam-plasma interaction, and are not simply due to scattering by the neutral gas. This is proved by the effect of the biased collector that served to continuously collect any ions produced by the beam. (b) The velocities of some of the electrons were changed by the interaction; during the sharp break in the currents the emitted light intensity increases considerably over the value of intensity resulting from excitation by beam electrons only. (c) A minimum density of ion-electron pairs must be built up before the oscillation phenomenon can occur. This conclusion is suggested by the fact that the delay between the pulse leading edge and the onset of oscillations decreases as the flow rate (and gas pressure) is increased.

It is tentatively proposed that the breakup of the beam observed here is the result of large-signal oscillations produced by the beam interaction with the plasma (the plasma is produced by the beam).

L. D. Smullin, W. D. Getty

References

1. W. D. Getty and L. D. Smullin, Experimental results of the study of the hollow-cathode discharge, Quarterly Progress Report No. 58, Research Laboratory of Electronics, M. I. T., July 15, 1960, pp. 35-41.

4. PLASMA HEATING BY ELECTRON BEAM-PLASMA INTERACTION

A study is being made of the energy transfer to a plasma from an electron beam injected into the plasma. Two cases of the one-dimensional beam-plasma interaction have been studied. In case (a), the plasma has an electron-ion collision frequency, but no thermal velocity distribution. In case (b), the plasma has no electron-ion collisions, but has a thermal velocity distribution. It was found that for reasonable beam and plasma parameters, more than 20 per cent of the dc beam power is transferred to the plasma ions in case (a) before the interaction leaves the small-signal region.

In analyzing the beam-plasma system, we recognize its similarity to two different types of beam microwave amplifier. The first of these types is the reactive-medium amplifier, in which the beam passes through a medium that carries a current that is proportional to the ac convection current on the beam. The second is the squeezer (1), in which the beam traverses a series of closely spaced externally loaded interaction gaps.

These two amplifiers and the beam-plasma interaction can be analyzed on a small-signal basis, and exponential growth constants for space-charge waves on the electron

beam can be found. A comparison of the results for the squeezer and the reactive-medium amplifier yields a growth constant in terms of an arbitrary gap loading. Equating this growth constant with that for the beam-plasma interaction yields an equivalent squeezer gap circuit for the plasma interaction.

To carry the analysis into the large-signal domain, the small-signal equivalent gap circuits are retained in the squeezer structure and the large-signal analysis of this device developed by Bers (1) and Briggs (2) is used. The input to the structure is determined from the small-signal analysis. The bunching of the beam electrons may be followed to the point at which slow electrons begin to be overtaken by the faster ones.

a. Small-Signal Analysis

The beam characteristic admittance and growth constant for a system characterized by a driving current that is proportional to the beam current are given by

$$Y_o = \frac{\omega \epsilon_o \beta_{pb}}{(1-m)^{1/2}} \tag{1}$$

$$\gamma_{\pm} = j\beta_{eb} \pm j\beta_{pb}(1-m)^{1/2} \tag{2}$$

where m is a complex constant representing the ratio of the driving current to the ac beam current. Figure II-14 shows an equivalent circuit for a typical squeezer gap. Identification of I(t) with the driving current leads to

$$m = \frac{1}{1 + jz_c} \tag{3}$$

with

$$z_c = \frac{\omega \epsilon_o}{d} Z_c \tag{4}$$

The growth constant is, then,

$$\gamma_{\pm} = j\beta_{eb} \pm j\beta_{pb}\left(\frac{jz_c}{1 + jz_c}\right)^{1/2} \tag{5}$$

It should be noted that although I(t) is a function of time only in each gap, it can be smoothed out over the length of the squeezer to a continuous function of z and t.

b. Equivalent Circuits

The growth constant for the one-dimensional beam-plasma interaction, with thermal velocities ignored, can be solved explicitly.

$$\gamma_{\pm} = j\left[\beta_{eb} \pm \beta_{pb}\left(\frac{\omega_{pa}}{2\nu_{ca}}\right)^{1/2}\right] \mp \beta_{pb}\left(\frac{\omega_{pa}}{2\nu_{ca}}\right)^{1/2} \tag{6}$$

In Eq. 6, ν_{ca} is the average electron-ion collision frequency. Equating Eqs. 6 and 5 gives the gap impedance (see Fig. II-15)

$$Z_c = \frac{d\nu_{ca}}{\epsilon_o \omega_{pa}^2} + \frac{jd}{\epsilon_o \omega_{pa}} \tag{7}$$

The interaction of an electron beam with a plasma possessing a thermal velocity distribution has been analyzed by Boyd (3). With collisions neglected, the growth constant for a growing wave is given by

$$\gamma_+ = j\beta_{eb}\left[\frac{1}{2} + \frac{1}{2}(1+j4\sqrt{\sigma})^{1/2}\right] \tag{8}$$

where

$$\sigma = R\left(\frac{\omega_{pb}}{\omega_{pa}}\right)^2 \tag{9}$$

and

$$R = \frac{\frac{1}{2}mv_{ob}^2}{\frac{3}{2}KT} \tag{10}$$

The equivalent circuit is shown in Fig. II-16. The parameters R and X in Fig. II-16 are given by

$$R = \frac{d}{2\omega_{pa}\epsilon_o}\left(\frac{\omega_{pa}}{\omega_{pb}}\right)^2 \left\{2\sqrt{\sigma}\frac{1}{\sqrt{2}}\left[(1+16\sigma)^{1/2}-1\right]^{1/2}\right\} \tag{11}$$

$$X = \frac{-d}{2\omega_{pa}\epsilon_o}\left(\frac{\omega_{pa}}{\omega_{pb}}\right)^2 \left\{1 - \frac{1}{\sqrt{2}}\left[(1+16\sigma)^{1/2}+1\right]^{1/2}\right\} \tag{12}$$

c. Beam Characteristic Admittance

The beam characteristic admittance can be found in terms of $z_c = r_c + jx_c$ from Eqs. 1, 2, and 5.

$$Y_o = \pm \frac{\omega\epsilon_o\beta_{pb}\left[(1-x_c)^2+r_c^2\right]^{1/2}}{\left(r_c^2 - x_c(1-x_c)+jr_c\right)^{1/2}} \tag{13}$$

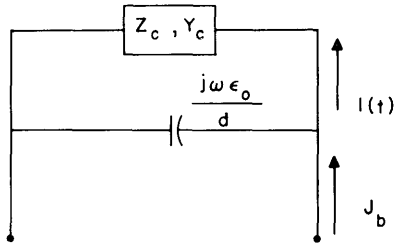

Fig. II-14. Squeezer gap circuit.

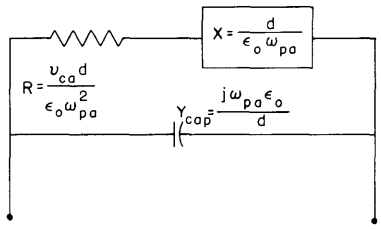

Fig. II-15. Equivalent gap circuit for cold plasma with collision frequency ν_{ca}.

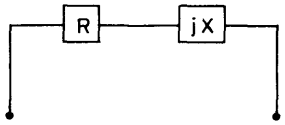

Fig. II-16. Equivalent gap circuit for plasma with thermal velocity distribution.

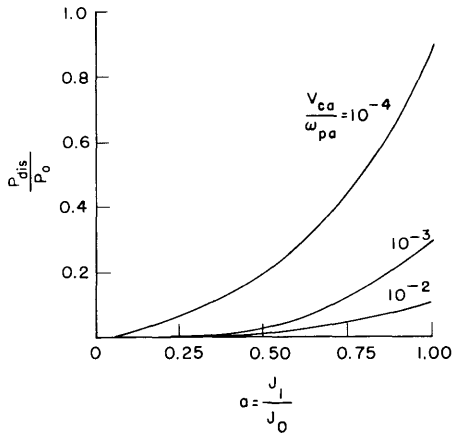

Fig. II-17. Ratio of power dissipated in plasma to dc beam power versus ratio of ac to dc beam current.

It can be seen that (a) the beam carries no real kinetic power when $r_c = 0$ and $x_c(1-x_c) > 0$, and (b) the beam always carries real kinetic power when $r_c \neq 0$, that is, when there is dissipation in the medium.

The beam characteristic admittance gives the relative sizes of the current and velocity modulation – an important factor in determining the range of validity of the small-signal analysis.

d. Small-Signal Power Transfer

The power dissipated in the equivalent resistance in the gap circuit for the interaction of a beam with a "cold" plasma with collisions is plotted in Fig. II-17 for parametric values of ν_{ca}/ω_{pa}. The beam and plasma parameters shown here have been measured in the hollow-cathode discharge described by Getty and Smullin (4).

D. L. Morse

References

1. A. Bers, Interaction of Electrons with Electromagnetic Fields of Gaps with Applications to Multicavity Klystrons, Sc. D. Thesis, Department of Electrical Engineering, M. I. T., June 1959.

2. R. J. Briggs, Bunching of One-Dimensional Electron Beams, S. M. Thesis, Department of Electrical Engineering, M. I. T., January 1961.

3. G. Boyd, Experiments on the interaction of a modulated electron beam with a plasma, Technical Report No. 1, California Institute of Technology, Pasadena, California, May 1959.

4. W. D. Getty and L. D. Smullin, Experimental results of the study of the hollow-cathode discharge, Quarterly Progress Report No. 58, Research Laboratory of Electronics, M. I. T., July 15, 1960, p. 35.

5. PROBE MEASUREMENTS IN THE HOLLOW-CATHODE DISCHARGE

Probe measurements were made on the hollow-cathode discharge to determine the density and temperature of the plasma as a function of radial distance from the core of the arc, for different arc currents.

The temperature was calculated from simple Langmuir probe theory, which assumes a Maxwellian distribution.

$$T_e = \left[\frac{d}{dv} \ln (J-J_+)\right]^{-1}$$

where V is the probe voltage with respect to the anode, J_+ is the ion saturation current, J is the probe current, and T_e is the electron temperature in electron volts. The electron density n was calculated from the ion saturation current.

$$n = \frac{J_+}{0.40\ eA}\left(\frac{m_+}{2eT_e}\right)^{1/2}$$

where e is the electronic charge, A is the probe area, and m_+ is the mass of the ion.

A small tantalum probe was used; its length was equal to several electron Larmor radii. Figure II-18 shows the geometry of the probe, and Fig. II-19 shows a typical probe curve.

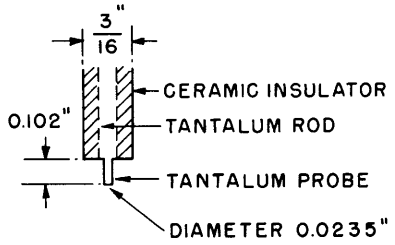

Fig. II-18. Geometry of the probe.

The electron temperature was found to range between 1.4 ev far from the arc to 16 ev at the visible edge of the arc, as shown in Fig. II-20. The corresponding densities range between 0.3×10^{12} and 3×10^{12} per cubic centimeter, as shown in Fig. II-21. Because of the extreme temperatures, the probe could not be inserted into the center of the arc.

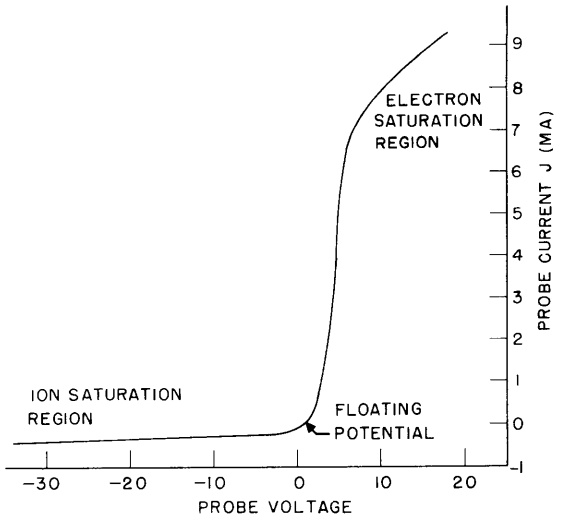

Fig. II-19. A typical probe characteristic for an arc current of 5 amps. The probe was approximately 1.37 inches from the center of the arc.

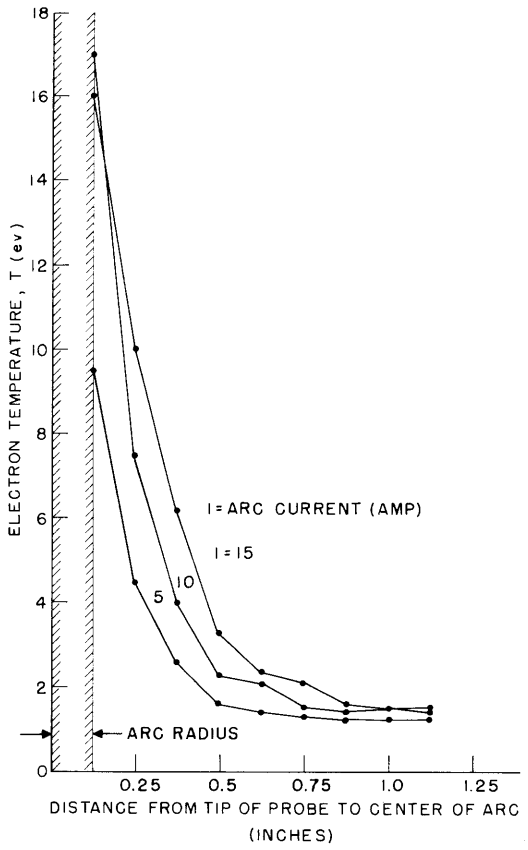

Fig. II-20. Variation of electron temperature with radial distance from the center of the arc.

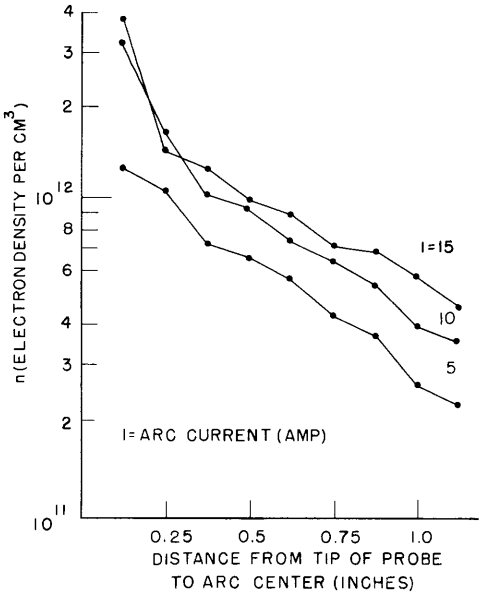

Fig. II-21. Variation of density with radial position.

The data were taken for a relatively low rate of gas flow (argon) through the cathode (3 cc-atm/min). Data taken previously at a higher flow rate (approximately 7 cc-atm/min) indicated one order of magnitude increase in particle density, with little change in temperature.

When the probe was placed very close to the edge of the arc, the plot of $\ln(J-J_+)$ was nonlinear; this suggests a non-Maxwellian distribution. This discrepancy could be the result of high-energy "streaming" electrons near the center of the arc. Thus there is still some uncertainty in the values of T_e for probe positions within 1/16 inch of the visible edge of the discharge.

A. W. Starr

6. SCATTERING OF WAVES BY A TENUOUS PLASMA OF FINITE GEOMETRY

We plan to build a plasma diagnostic system operating at f ≈ 150 kmc. This frequency is well above any plasma frequency that we expect to achieve. Therefore, taking $0 < \omega_p < \omega_o$, we plan to deduce the plasma frequency from measurements of transmission through the plasma. The plasma in which we are primarily interested is the hollow-cathode discharge. It is in a cylinder that is 10-15 cm long, with a 6-mm diameter, and ω_p is approximately 30-40 kmc. Thus even at 2-mm wavelength, we cannot treat the plasma as an "infinite" slab.

The study of this finite-geometry problem has already received some attention. One

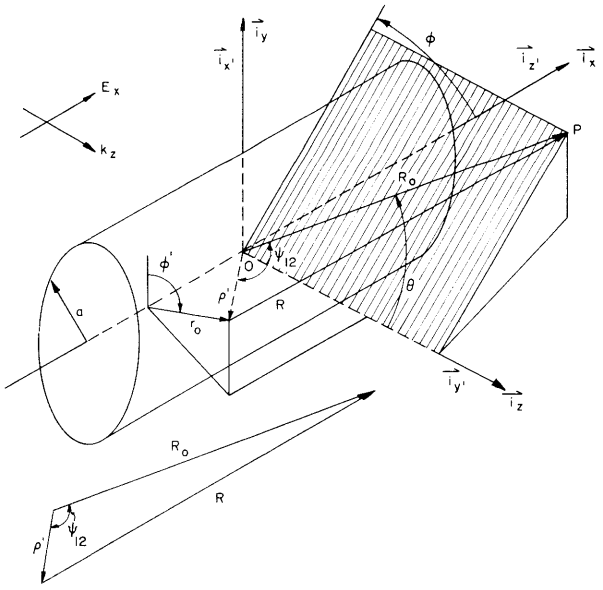

Fig. II-22. Geometry of the finite plasma cylinder.

experimental approach (1) involves the study of the scattered field and makes use of simulated geometries of known properties. One theoretical approach involves solving the boundary-value problem of a dielectric cylinder with losses. As an aid to solving the boundary-value problem, computers have been programmed to calculate the amplitude and phase of the reflection and transmission coefficients as functions of density, collision frequency, and plasma diameter (2).

Our research involves an investigation of both approaches. Thus far, work has been concentrated on the theoretical aspects of the problem. The present approach differs from the boundary-value approach, in that it assumes that the dominant field inside the plasma column is the incident uniform plane wave, since $\omega_p/\omega < 1$. The action of the uniform plane wave sets the electrons in motion, which motion in turn produces radiation. The far field of these radiators is computed from the vector potential

$$A_x = \frac{\mu_o}{4\pi} \int_{\substack{\text{volume of} \\ \text{plasma}}} \frac{J_{z'}(\rho')}{R} e^{-jkR} e^{j\omega t} \, d\tau' \tag{1}$$

in which the integration is over the volume of the plasma; R is the distance from the current distribution $J(\rho')$ to the point of observation; k is $2\pi/\lambda_o$; λ_o is the free-space wavelength; $J_{z'} = -N(\rho') \, ev_z(\rho \cdot t)$; $N(\rho')$ is the density — in our calculations, assumed to be $\begin{cases} N = N_o & r \leq a \\ N = 0 & r > a \end{cases}$ — and v_z' is calculated from

$$\frac{m dv_{z'}}{dt} = -eE_{z'} \, e^{j\omega t} \exp[-(jka + jky')] \tag{2}$$

The geometry of the finite plasma cylinder is indicated in Fig. II-22.

The following assumptions are made in deriving and integrating the equation of motion:

(a) $\omega \gg \omega_p$;

(b) the excitation is such that $v \ll c$; and

(c) no thermal or drift motions are taken into account.

In considering the scattering of the incident wave, the first assumption allows us to neglect the interaction of the charges of the plasma with each other. The second assumption allows us to neglect the $\vec{v} \times \vec{B}$ term.

In carrying out the integrations for the vector potential, it is assumed that $R_o \gg 2\ell$, a, λ, and therefore

$$R \approx R_o$$

$$kR \approx kR_o - [kr_o \sin \phi' \cos \theta + kr_o \sin \theta \sin \phi \cos \phi' + kz_o \sin \theta \cos \phi]$$

Here, x', y', z' are the Cartesian coordinates used in carrying out the integration; the cylindrical variables have the following limits:

$$0 \leq r_o \leq a$$

$$0 \leq \phi' \leq 2\pi$$

$$-\ell \leq z_o \leq \ell$$

R_o is the distance from the origin O to the observation point P; R is the distance from the charge distribution to the point P; and p' is the distance from the origin to the charge distribution. The x, y, z coordinates are the Cartesian coordinates for the observation point P. Equation 1 can be rewritten as

$$A_x = \frac{\omega_p^2 E_{z'}}{4\pi R_o j\omega c^2} \exp(j\omega t - jkR_o - jka) \int_0^{2\pi} \int_0^{a} \int_{-\ell}^{\ell} r_o d\phi' dr_o dz_o \exp(jk\Phi)$$

where

$$\Phi = jk[r_o \cos\phi' \sin\theta \sin\phi + z_o \sin\theta \cos\phi + r_o \sin\phi'(\cos\theta - 1)]$$

For $\phi = \pi/2$, the plane POQ lies in the y-z plane.

$$E_{\phi \text{ scattered}} = + \frac{\partial A_x}{\partial t} = j\omega A_x$$

$$= \frac{\omega_p^2}{\omega^2} \left[\frac{2\pi(2\ell)}{\lambda}\right]\left[\frac{2\pi(2a)}{\lambda}\right] \frac{a}{8R_o} E_{z'} \exp(j\omega t - jkR_o - jka) F_{\text{geometry}}$$

For arbitrary θ,

$$F_{\text{geometry}} = \left\{1 + \frac{x^2}{2!} + \frac{x^4}{3!2!} + \ldots + \frac{x^{2n}}{(n+1)!n!} + \ldots\right\}$$

where $x = jka \sin\theta/2$.

For the special case $\theta = 0$, $\theta = \pi$

$$F(\theta=0) = 1$$

$$F(\theta=\pi) = \left[1 + \frac{1}{2!}(jka)^2 + \ldots + \frac{1}{n!}\frac{1}{(n+1)!}(jka)^{2n} + \ldots\right]$$

For our case ($ka \approx 9.5$), with the use of Stirling's formula, the term $(jka)^{2n}/n!(n+1)!$, for $n = 24$, is of the order of 10^{-2}. The total field at $(\theta=0, R_o)$ is given by

$$E_\phi = -E_{z'}\left[1 - \frac{\omega_p^2}{\omega^2}[k2\ell][k2a]\frac{a}{8R_o}\exp(j\omega t - jkR_o - jka)\right]$$

For an infinite slab (thickness 2a) of lossless dielectric, the boundary-value solution of the field at $(\theta=0, R_o)$ is

$$E_{\phi \text{ boundary value}} = \frac{-4E_{z'} \exp(j\omega t - jkR_o + jka)}{\left(\frac{k}{k'}+1\right)^2 e^{2jk'a} - \left(\frac{k}{k'}-1\right)^2 e^{-2jk'a}}$$

where

$$k' = \omega(\epsilon_o\mu_o)^{1/2}\left[\left(1-\frac{\omega_p^2}{\omega^2}\right)^{1/2}\right]$$

and for $(\omega_p/\omega)^2 \ll 1$,

$$E_{\phi \text{ boundary value}} \approx -E_{z'}\left(1-\frac{1}{2}\frac{\omega_p^2}{\omega^2}\right)\exp\left[j\omega t - jkR_o - jka + jka\frac{\omega_p^2}{\omega^2}\right]$$

A comparison of these results shows that the finite cylinder causes less attenuation of the amplitude, and causes no first-order phase shift. For the infinite slab, the phase advance is $ka\omega_p^2/\omega^2$. As the size of the plasma region is increased $(R_o \geq \ell, a, \lambda)$, we must use higher-order terms in approximating the phase kR in the expression for the vector potential. Thus, at the point P $(\theta=0, R_o)$, kR to second order in $(1/R_o)$ is

$$kR \approx kR_o - kr_o \sin\phi' + \frac{1}{2}\frac{kr_o^2}{R_o}\cos^2\phi' + \frac{1}{2}\frac{kz_o^2}{R_o}$$

Equation 1 becomes

$$A_x = \frac{\omega_p^2 E_{z'}}{4\pi R_o j\omega c^2}\exp(j\omega t - jkR_o - jka)\iiint \exp\left[-\frac{1}{2}\frac{jk}{R_o}\left(z_o^2 + r_o^2\cos^2\phi'\right)\right] r_o dr_o d\phi' dz_o$$

and the total field at $(\theta=0, R_o)$ is approximately

$$E_\phi \approx -E_{z'}\exp(j\omega t - jkR_o - jka)\left\{\left[1-\left(\frac{\omega_p}{\omega}\right)^2\frac{(k\ell)(ka)\,a}{2R_o} + \frac{j(ka)^2\,k\ell}{48R_o^2}\left(\frac{\omega_p}{\omega}\right)^2(4\ell^2+3a^2)\right]\right\}$$

The second-order phase advance caused by a larger but finite tenuous plasma cylinder is

$$\theta \approx \tan\theta = \tan\frac{E_{im}}{E_{real}} \approx ka\left(\frac{\omega_p}{\omega}\right)^2\left[\frac{(ka)(k\ell)\left(4\ell^2+3a^2\right)}{48R_o^2}\left(1+\left(\frac{\omega_p}{\omega}\right)^2\frac{(k\ell)(ka)\,a}{2R_o}\right)\right]$$

In future work, we shall examine more carefully the relationship between the phase advance and the size of the cylinder, consider the effects of density profiles, and correlate the theoretical values with the experimental data to be obtained from cylindrical geometries of known properties.

H. Y. Hsieh

References

1. B. Rosen, The inverted universe plasma analog for microwaves, Project Matterhorn Technical Memorandum No. 85, Princeton University, August 1959.

2. S. Edelberg, Electromagnetic interaction with re-entry plasmas, Re-entry Physics Program Semiannual Technical Reports, June 1959, December 1959, June 1960, Lincoln Laboratory, M. I. T.

7. STUDIES OF A HIGH-POWER PULSED MICROWAVE GAS DISCHARGE

The operating characteristics of a system consisting of a dense plasma that is produced by the fields of a resonant cavity are considered here. The circuit analysis of this system is complicated by the fact that the resonant properties of the system depend on the plasma parameters. The plasma is able to control the amount of microwave power it receives by shifting its electron density and, as a consequence, the resonant frequency of the cavity. Therefore stable operation will be achieved only when the power required by the plasma to produce a given plasma electron density is just that supplied to the plasma by the microwave cavity fields. In this report the calculated stable operating points of the system are given as functions of the level and frequency of the microwave power incident on the resonant cavity.

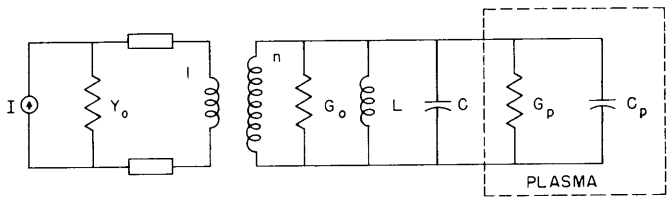

Fig. II-23. Equivalent circuit for a cavity containing a dense plasma at frequencies near a single resonance.

An equivalent circuit for a plasma in a resonant cavity that is connected to a matched source by a transmission line is shown in Fig. II-23. In this circuit the equivalent cavity conductance, inductance, and capacitance are denoted G_o, L, and C; and G_p and C_p are the real and imaginary parts of the equivalent admittance of the plasma.

In the calculation of the power distribution for the various parts of this circuit it is convenient to normalize the circuit parameters to the cavity conductance G_o. We define the following parameters:

$$\beta_1 = \frac{Y_{o1}}{n^2 G_o}$$

$$\beta_p = \frac{G_p}{G_o}$$

$$L_n = G_o L = \frac{1}{\omega_o' Q_o}$$

$$C_n = \frac{C}{G_o} = \frac{Q_o}{\omega_o'}$$

where Q_o is the unloaded cavity Q value when the plasma is replaced by a perfect conductor; β_1 is the input cavity coupling coefficient; β_p is the plasma coupling coefficient and is the ratio of the microwave power dissipated in the plasma to the power dissipated in the rest of the cavity; and ω_o' is the resonant frequency of the cavity when the plasma is present and can be related to the unperturbed cavity resonant frequency by

$$\omega_o' = \omega_o - \delta\omega \tag{1}$$

where ω_o is the cavity resonant frequency when the plasma is replaced by a perfect conductor, and $\delta\omega$ is the shift of resonant frequency that occurs as a result of the presence of the plasma.

Given the microwave power reflected from the resonant cavity, we can find the power P_p absorbed in the plasma in terms of the microwave power P_i incident on the cavity and the circuit parameters. The result is

$$\frac{P_p}{P_i} = \frac{4\beta_1\beta_p}{(1+\beta_1+\beta_p)^2 + \left(2Q_o \frac{\Delta\omega - \delta\omega}{\omega_o}\right)^2} \tag{2}$$

in which $\Delta\omega$ is defined as $\Delta\omega = \omega_o - \omega$. In obtaining Eq. 2 the assumption was made that the system is never operated far from resonance.

Figure II-24 is a graphical representation of Eq. 2 showing the definitions of $\delta\omega$ and $\Delta\omega$. This figure also illustrates the two possible operating states that are implied in Eq. 2; that is, for $\delta\omega$ greater than, or less than, $\Delta\omega$. The state in which the system will operate depends on the power requirements of the plasma.

We now assume that the power required to maintain a density n in the plasma

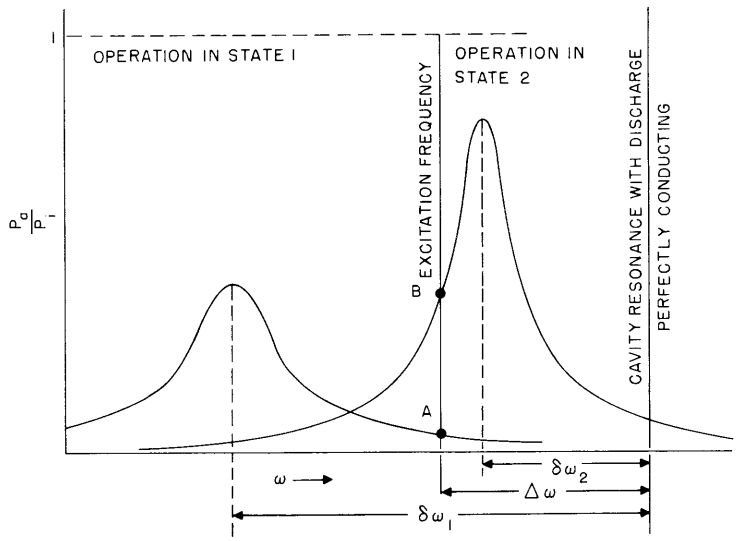

Fig. II-24. Graphical representation of Eq. 2 illustrating the definitions of $\delta\omega$ and $\Delta\omega$. Also indicated are the two possible operating states. (A is the operating point for state 1; B, for state 2.)

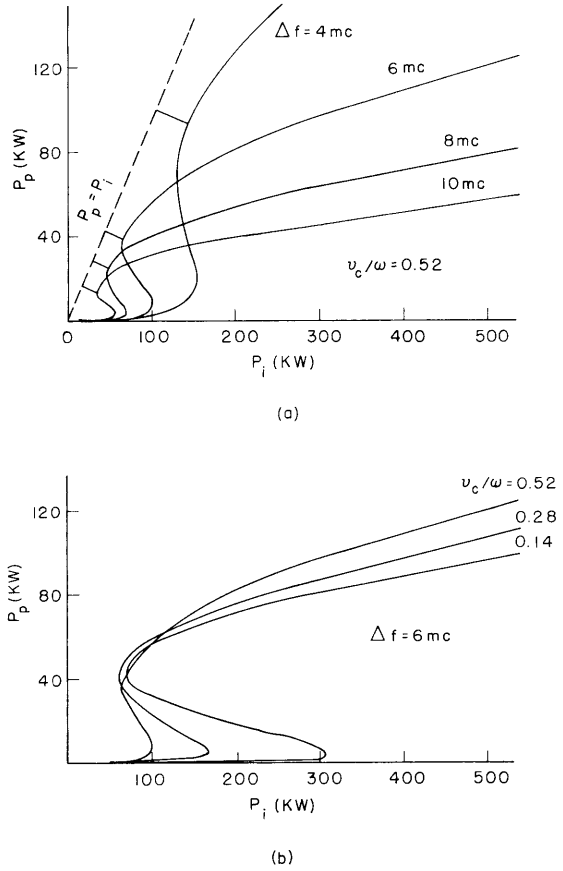

Fig. II-25. Plots of operating points given in Fig. II-24. P_p versus P_i for: (a) parametric Δf; (b) parametric v_c/ω.

is proportional to n. Thus

$$n = K_1 P_p \tag{3}$$

From the theory presented in a previous report (1), we obtain, for $\nu_c/\omega < 1$,

$$\beta_p = \frac{Q_o}{\omega_o}\,\delta\omega\,\frac{\nu_c}{\omega} \tag{4a}$$

and

$$\frac{\delta\omega}{\omega_o} = \frac{cK_g}{2\omega_p} \tag{4b}$$

where ν_c is the collision frequency for momentum transfer; ω_p is the electron plasma frequency; c is the velocity of light; and K_g is a geometrical constant. Substitution of Eqs. 3 and 4 in Eq. 2 yields

$$\frac{P_p}{P_i} = \frac{K_2(P_p)^{1/2}\,4\beta_1\left(\frac{\nu_c}{2\omega}\right)}{\left[(1+\beta_1)\,K_2(P_p)^{1/2} + \frac{\nu_c}{2\omega}\right]^2 + \left[\left(\frac{2Q_o}{\omega_o}\right)\Delta\omega K_2(P_p)^{1/2} - 1\right]^2} \tag{5}$$

where

$$K_2 = \left(\frac{K_1 e^2}{m\epsilon_o}\right)^{1/2}\frac{1}{cK_g Q_o}$$

Equation 5 has been solved for P_p in terms of P_i for a few parametric values of ν_c/ω and $\Delta\omega$. Graphs of these solutions are presented in Fig. II-25. The parameter K_2 was chosen so that the solutions of Eq. 5 would give values of P_p and P_i that could be used to analyze the experiments previously described (2). The dotted line in Fig. II-25 represents the condition that all of the incident power is dissipated in the plasma. The perpendicular lines drawn from the dotted lines to the operating point loci show the points at which this condition is most nearly reached. These, then, are the points at which $\delta\omega = \Delta\omega$ and the system is excited at resonance. These lines also separate the two states of operation illustrated in Fig. II-24. The system operates in state 1 at small values of incident power, and in state 2 at large values of P_i.

Many of the operating characteristics of the system previously described (2) can be found from inspection of Fig. II-25. At large incident power levels the amount of power dissipated in the plasma, and therefore the plasma electron density, are relatively independent of the incident power. In this region, P_p is a strong function of the excitation frequency. At low gas pressures, and therefore at small collision frequencies, more incident power is required to cause the system to operate in state 2. These conclusions are in agreement with experimental results.

T. J. Fessenden

References

1. T. J. Fessenden, Measurement of a dense plasma in a resonant cavity, Quarterly Progress Report No. 60, Research Laboratory of Electronics, M. I. T., Jan. 15, 1961, pp. 34-37.

2. T. J. Fessenden, Studies of a high-power pulsed microwave gas discharge, Quarterly Progress Report No. 58, Research Laboratory of Electronics, M. I. T., July 15, 1960, pp. 44-48.

8. PENNING IONIZATION GAUGE (PIG) DISCHARGE

A study was begun in the fall of 1960 for the purpose of investigating the operating characteristics of the Penning Ionization Gauge (PIG) discharge. The PIG discharge is a reflex discharge (1, 2) with an externally applied axial magnetic field (Fig. II-26). Electrons oscillate along the magnetic field lines in the region between the two cathodes.

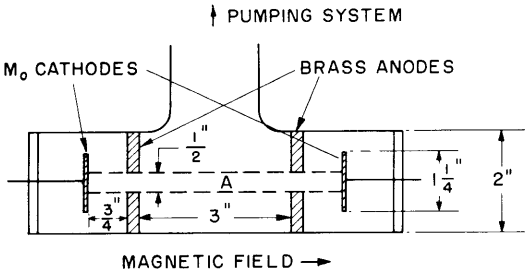

Fig. II-26. Cross section of cylindrical PIG discharge. The plasma is formed in region A.

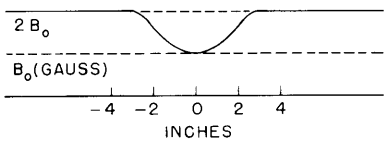

Fig. II-27. Magnitude of the mirror magnetic field as a function of distance from the center of the discharge.

They collide with the neutral gas and thus produce ions and slow electrons. The ions flow to the cathodes and cause emission of secondary electrons. Both the ions leaving the plasma and the secondary electrons entering it contribute a net negative current to the plasma regions. In the steady state the same amount of negative current must leave the plasma at the anode.

An experimental apparatus has been constructed and preliminary data are presented here. Our PIG discharge has two ring anodes, and is operated in a mirror magnetic field (Fig. II-27). The cathodes are made of molybdenum to minimize sputtering (3) and provide axial containment for the plasma. A schematic diagram of the electrical circuit is shown in Fig. II-28.

The voltage-current characteristics are plotted for various values of magnetic field (Fig. II-29a), and for two different pressures (Fig. II-29b). Notice that for small magnetic fields and low pressures there are regions that exhibit negative resistance, and

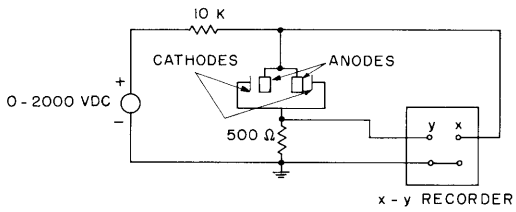

Fig. II-28. Electrical circuit.

regions in which the current goes to zero as the voltage is increased. The data were obtained by slowly decreasing the voltage from its maximum value and recording current and voltage on an automatic x-y recorder. The initial breakdown voltage is not reproducible, but after breakdown the voltage-versus-current characteristics are as shown in Fig. II-29.

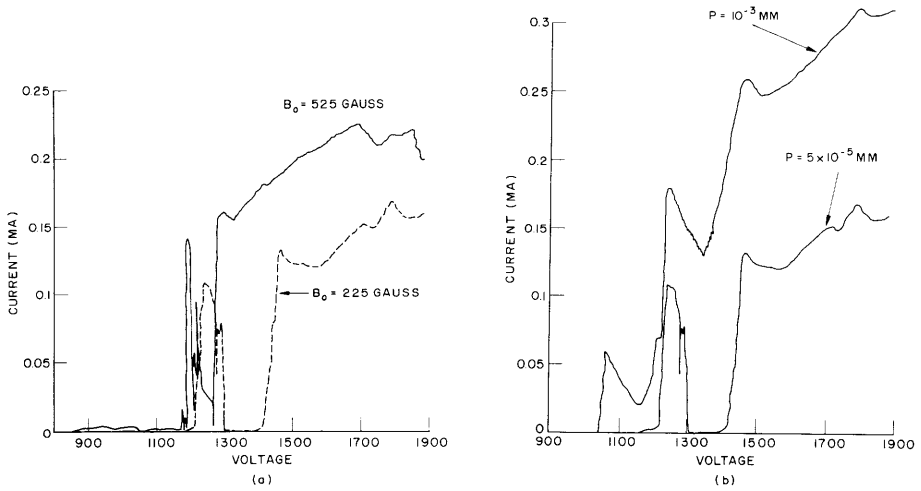

Fig. II-29. (a) V-I characteristics for two magnetic fields (P = 5×10^{-5} mm Hg).
(b) V-I characteristics for two pressures (B_o = 225 gauss).

Further experiments are planned for making probe measurements of plasma density and temperature. The noise emitted by the PIG discharge will also be studied in an effort to determine the characteristics of these negative-resistance regions.

W. Larrabee IV

References

1. J. Backus, Theory and operation of a Philips Ionization Gauge type discharge; The Characteristics of Electrical Discharges in Magnetic Fields, edited by A. Guthrie and R. K. Walkerling (McGraw-Hill Book Company, New York, 1949), Chapter 11, pp. 345-370.

2. R. E. Lundgren, Extraction and modulation of electron beam from Philips Ionization Gauge, Scientific Report No. 5 (UC-306), Electronics Research Laboratory, University of California, 1960.

3. J. D. Cobine, Gaseous Conductors (Dover Publications, Inc., New York, 1941), p. 230.

9. APPLICATIONS OF GEOMETRIC TECHNIQUES TO NONLINEAR DYNAMICS

a. Introduction

The dynamics of many physical systems can be described by a set of ordinary differential equations. In general, explicit, closed-form solutions of these equations are extremely difficult – if not impossible – to find. Approximate solutions may be established by linearization, power-series expansions or perturbation techniques. However, even though approximate solutions serve a very useful purpose in the necessarily limited range of their applicability, they fail to provide any information about the boundedness, stability, and periodicity of the solutions in the very important case of large deviations from equilibrium.

The general properties of the solutions mentioned above can be investigated through use of the topological techniques developed by Liapunov, Poincaré, Malkin, and others (1). Again, however, even though topological methods provide elegant and rigorous criteria for boundedness, stability, and periodicity, the implementation of these criteria in any specific problem is often just as complex as the derivation of the solution itself.

The difficulty of implementing the criteria of the topological theory may be overcome in the case of third-order autonomous nonlinear systems by a simple geometric interpretation of Liapunov's second method (1) and use of Poincaré's method of sections (1).

More precisely, consider the third-order nonlinear system

$$\frac{dx}{dt} = f(x) \tag{1}$$

where x is a three-dimensional vector, and f(x) is a column matrix, nonlinear function of x. Assume that the system admits a critical point x_1.

$$f(x_1) = 0 \tag{2}$$

If a surface exists that is large enough to include the critical point and any possible initial displacements and has the property that the vector field dx/dt crosses it inwardly everywhere, then the solutions of Eq. 1 are bounded. If the critical point is stable, then the solutions may converge to it; if it is unstable, periodic solutions may exist. If such a surface does not exist, the solutions are unbounded. This is the geometric interpretation of Liapunov's second method.

The question of periodic solutions can be answered in a similar manner. Consider a closed region, topologically equivalent to a solid torus, free of critical points, with the property that the vector field dx/dt points inwardly at every point of the surface enclosing the region. In other words, consider a toroidal trap for trajectories x(t) that lie inside it. Assume that the trajectories intersect a certain cross section S_1 of the torus without contact, that is, without ever being tangent to it. This means that the

vector field dx/dt intersects S_1 at points Q, Q' ... and defines a topological mapping $Q \rightarrow Q'$ of S_1 into itself. If the cross section S_1 has a fixed point P, that is, if P is mapped into itself, then the particular trajectory that corresponds to $P \rightarrow P$ is closed and therefore periodic. This is Poincaré's method of sections.

In addition, if a simply connected section S_1 is mapped into itself by means of a continuous function, the mapping possesses at least one fixed point, and consequently it admits at least one closed or periodic path. This is Brouwer's fixed-point theorem (2).

The procedure that has been outlined is best illustrated by means of a specific example. This example is pertinent to a xenon-controlled nuclear reactor, but the equations are general enough to be adaptable to other physical systems. Other third-order systems have been treated by the same method (3).

b. Illustrative Example

Consider a third-order system whose dynamics are describable by the set of equations:

$$\frac{d\phi}{dt} = \omega_o(1-X)\,\phi \tag{3}$$

$$\frac{dI}{dt} = \lambda_i(\phi - I) \tag{4}$$

$$\frac{dX}{dt} = \lambda_x(\alpha\phi + \beta I - \gamma\phi X - X) \tag{5}$$

where $\omega_o = \frac{\delta_o}{\tau_e}$, $\alpha = \frac{y_x}{y - c\delta_o}$, $\beta = \frac{y_i}{y - c\delta_o}$, $\gamma = \frac{c\delta_o}{y - c\delta_o}$,

$$\alpha + \beta - \gamma = 1, \quad y = y_i + y_x$$

Here, c, λ_i, λ_x, τ_e are positive, system parameters, δ_o, y_i, y_x are positive, adjustable parameters, and ϕ, I, X are variables, physically constrained to be positive.

The problem is to examine the boundedness and stability of the system for small and large deviations from equilibrium.

(i) Stability of the Critical Point

Notice that the system admits a trivial critical point (ϕ=0, I=0, X=0), and a nontrivial critical point (ϕ=1, I=1, X=1), provided that $y > c\delta_o$.

Consider the critical point (1, 1, 1). The type of stability at the critical point can be investigated by considering the linear approximation of Eqs. 3-5.

The characteristic equation of the linear approximation is

$$s^3 + [\lambda_x(\alpha+\beta)+\lambda_i]\,s^2 + \lambda_x[\lambda_i(\alpha+\beta)+\omega_o]\,s + \lambda_i\lambda_x\omega_o = 0 \tag{6}$$

or its equivalent,

$$1 + \omega_o \lambda_x (\alpha - \gamma) \frac{s + \dfrac{\lambda_i}{\alpha - \gamma}}{s[s+\lambda_x(\alpha+\beta)][s+\lambda_i]} = 0 \tag{7}$$

Use of any of the well-known linear stability criteria yields the following results.

For $\alpha > \gamma$ ($y_x > c\delta_o$), the critical point is stable when

$$\Delta = \frac{c\delta_o}{y} < \frac{c\lambda_i \tau_e}{y} \frac{1 + \Lambda - \Delta}{1 - (1+\Lambda)\psi + (\psi - 1 + \Lambda)\Delta} \tag{8}$$

where $\Lambda = \lambda_x/\lambda_i$, and $\psi = y_x/y$. Condition 8 is plotted in Fig. II-30 for the particular values $c = 1.5$, $\lambda_i = 2.87 \times 10^{-5}$ sec^{-1}, $\lambda_x = 2.09 \times 10^{-5}$ sec^{-1}, $y = 6.4 \times 10^{-2}$, and $\tau_e = 0.1$ sec.

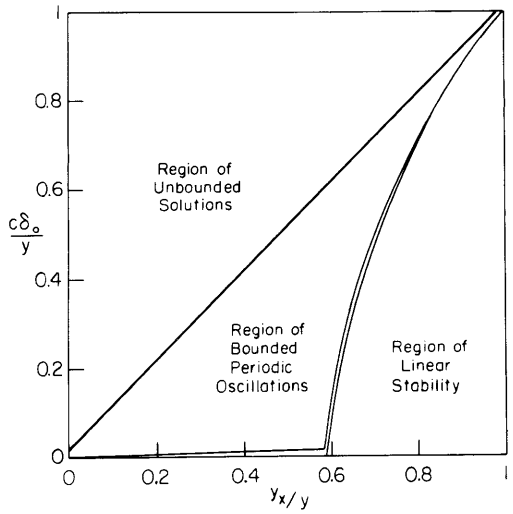

Fig. II-30. Regions of linear stability, periodic oscillations, and unbounded solutions.

For $\alpha < \gamma$ ($y_x < c\delta_o$), the critical point is always unstable because for all values $\alpha < \gamma$ the roots of Eq. 7 are in the right-half s-plane.

To summarize, the linear approximation yields an unstable critical point whenever condition 8 is not fulfilled (Fig. II-30).

(ii) Boundedness and Stability for Large Deviations from Equilibrium

The boundedness of the solutions for very large deviations from equilibrium can be examined by investigating the existence of a closed surface in phase space (ϕ, I, X) that

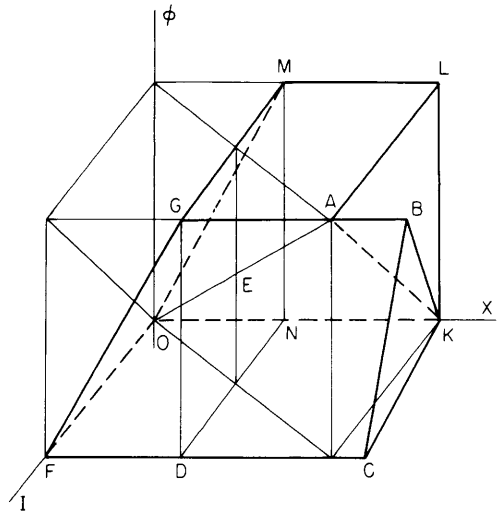

Fig. II-31. Closed surface surrounding critical point E, intersected inwardly by all trajectories when $c\delta_o < y_x$.

is crossed inwardly by the vector field $(d\phi/dt, dI/dt, dX/dt)$.

For $\alpha > \gamma$, consider the surface shown in Fig. II-31, consisting of eight mutually intersecting plane surfaces defined as follows: Take the arbitrary point A(a, a, a) with a > 1. Define the plane surfaces:

ABCDFGA:	Plane $E_1 \parallel I = 0$ through point A
ABKA:	Plane E_2 defined by $\phi - I = 0$ $(X \geq a)$
ALKA:	Plane E_3 defined by $X = a$ $(\phi \geq I)$
ALMGA:	Plane E_4 defined by $\phi = a$ $(a \geq X \geq 1, \phi \geq I)$
BKCB:	Plane E_5 defined by $\alpha\phi + \beta I - X = -a$ $(X \leq a, I \leq \phi)$
CDFONKC:	Plane E_6 defined by $\phi = 0$
KLMONK:	Plane E_7 defined by $I = 0$
FGMOF:	Plane E_8 defined by $\phi = aX$ $(X \leq 1)$

It is evident that this surface does enclose the critical point E(1, 1, 1). All trajectories cross the surface inwardly because

$\frac{dI}{dt} < 0$ on E_1

$\frac{d\phi}{dt} < 0, \quad \frac{dI}{dt} = 0$ on E_2

$\frac{dX}{dt} < 0$ on E_3, provided that a is large

$\frac{d\phi}{dt} < 0$ on E_4

$\frac{d}{dt}(\phi^2+X^2+I^2) < 0$ on E_5

$\phi = 0, \frac{d\phi}{dt} = 0$ on E_6. The trajectories come only arbitrarily close to E_6 because $\phi < 0$ has no physical meaning.

$\frac{dI}{dt} > 0$ on E_7

Finally, on E_8 observe that the surface S: $\alpha\phi + \beta I - \gamma\phi X - X = 0$ crosses the lines:

$I = 0, X = 1$ at $\phi = 1/(\alpha-\gamma) > 0$

$\phi = I = X$ at $\phi = I = X = 1$

$\phi = 0, X = 1$ at $I = 1/\beta > 1$

If a is chosen large, the plane E_8 lies at the left of the surface S, and therefore $\frac{dX}{dt} > 0$ on E_8. Also, the projection of the vector $\frac{d\phi}{dt}, \frac{dI}{dt}, \frac{dX}{dt}$ on the normal of E_8 is

$$P_n = \omega_o(1-X)\,\phi - a\lambda_x[\alpha\phi+\beta I-\gamma\phi X-X]$$

$$= a\left[(\lambda_x a\gamma-\omega_o)X^2-(\lambda_x\alpha a-\omega_o-\lambda_x)X-\lambda_x\beta I\right] < 0 \qquad (9)$$

provided that $\alpha > \gamma$, and a is large. Consequently, the trajectories cross E_8 inwardly.

In view of the fact that the only requirement for the existence of the surface of Fig. II-31 is that a be large, it is evident that such a surface can be made to include all initial displacements and because it is intersected inwardly by all trajectories it constitutes a trajectory trap. Consequently, when $\alpha > \gamma$, the solutions of the system of Eqs. 3-5 are bounded. Furthermore, if the critical point is stable, the solutions are asymptotically stable; but if the critical point is unstable, the system admits, in general, periodic solutions, as it will be shown.

Next, consider the case in which $\alpha < \gamma$ and distinguish the following ranges.

The first range is

$$\frac{\omega_o(\gamma-\alpha)}{\lambda_i\gamma} < 1 \qquad (y_x<c\delta_o<y_x+c\lambda_i\tau_e)$$

Consider the closed surface shown in Fig. II-32, which consists of seven mutually intersecting plane surfaces defined as follows. Take the arbitrary point A (ϕ=b,I=b,X=βb) with b > 1. Define the plane surfaces:

ABCDA: Plane E_1 defined by $X = \beta b$

ADFGHA: Plane E_2 defined by $I = b$ in the region $I > \phi$

CDFOC: Plane E_3 defined by $\phi = 0$

CBKLOC: Plane E_4 defined by $I = 0$

FGLOF: Plane E_5 defined by $\phi = aX \left(a < b, X < \frac{\alpha}{\gamma}\right)$

GHKLG: Plane E_6 defined by $X = d < \alpha/\gamma$

ABKHA: Plane E_7 defined by $\phi - \frac{b-a}{b} I = a$

This surface does enclose the critical point E(1, 1, 1). All trajectories cross the surface inwardly because $\frac{dX}{dt} < 0$ on E_1. To see this clearly, consider, again, the ruled hyperboloid S: $a\phi + \beta I - \gamma\phi X - X = 0$. This hyperboloid has an asymptotic plane at

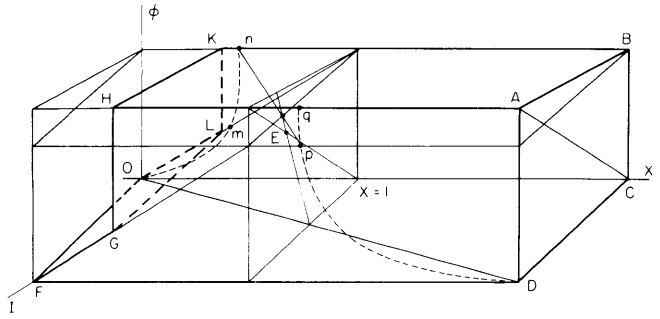

Fig. II-32. Closed surface surrounding critical point E, intersected inwardly by all trajectories when $y_x < c\delta_o < y_x + c\lambda_i\tau_e$.

$X = \frac{\alpha}{\gamma} < 1$ and intersects the plane $I = 0$ along the hyperbolic branch Omn and the plane $I = b$ along the hyperbolic branch Dpq. For all points at the right of this surface, $dX/dt < 0$ and, therefore, the same is true for plane E_1

$\frac{dI}{dt} < 0$ on E_2

$\frac{d\phi}{dt} = 0, \ \phi = 0$ on E_3. The trajectories come only arbitrarily close to E_3 because $\phi < 0$ has no physical meaning.

$\frac{dI}{dt} > 0$ on E_4

The projection of the vector $\frac{d\phi}{dt}, \frac{dI}{dt}, \frac{dX}{dt}$ on the normal of plane E_5 is negative, provided that a is large enough, and a range of X smaller than, but arbitrarily close to, α/γ is considered (see Eq. 9). Consequently, the trajectories cross E_5 inwardly.

$$\frac{dX}{dt} > 0 \qquad \text{on } E_6$$

since it is at the left of the hyperboloid S.

Finally, the projection of the vector $\frac{d\phi}{dt}$, $\frac{dI}{dt}$, $\frac{dX}{dt}$ on the normal of plane E_7 is

$$P'_n = \omega_o(1-X)\,\phi - \frac{b-a}{b}\lambda_i(\phi-I) < 0 \tag{10}$$

provided that

$$\frac{\omega_o(1-X)}{\lambda_i} < \frac{b-a}{b} < 1 \qquad \text{for } X > d \tag{11}$$

In view of the fact that the range of values α, β, γ under consideration is such that

$$\frac{\omega_o(\gamma-\alpha)}{\lambda_i\gamma} < 1$$

and d can be taken arbitrarily close to α/γ, conditions 10 and 11 are readily satisfied, and the trajectories cross plane E_7 inwardly.

Since the only requirements for the existence of the surface of Fig. II-32 are that a and b > a be large, it can be concluded immediately that the solutions are bounded for $c\delta_o < y_x + c\lambda_i\tau_e$.

The second range is

$$\frac{\omega_o(\gamma-\alpha)}{\lambda_i\gamma} > 1 \qquad (c\delta_o > y_x + c\lambda_i\tau_e)$$

In this range the solutions are unbounded because no closed surface surrounding the critical point can be found. In fact, the solutions diverge either monotonically or in an oscillatory manner.

Monotonic divergence is possible only when the vector $\frac{d\phi}{dt}$, $\frac{dI}{dt}$, $\frac{dX}{dt}$ has positive or zero components asymptotically. Inspection of Eqs. 3-5 reveals that the only possibility is

$$X = \text{constant} < 1 \qquad \frac{dX}{dt} = 0$$

The solution X = constant is admissible when the cross section of the ruled hyperboloid S by the plane X = constant < 1 has a slope equal to the asymptotic value of $d\phi/dI$. Consequently,

$$\omega_o(1-X)\,\phi(\alpha-\gamma X) + \lambda_i(\phi-I)\,\beta = 0$$

or

$$X^2 - X\left[1 + \frac{\lambda_i}{\omega_o} + \frac{\alpha}{\gamma}\right] + \frac{\lambda_i(\alpha+\beta)}{\omega_o\gamma} + \frac{\alpha}{\gamma} - \frac{\lambda_i}{\omega_o\gamma}\frac{X}{\phi} = 0$$

For $\phi \to \infty$, this equation admits positive solutions smaller than 1 only when

$$c\delta_o \geq 2(c\lambda_i\tau_e y_i)^{1/2} + y_x - c\lambda_i\tau_e$$

When $y_x + c\lambda_i\tau_e < c\delta_o < 2(c\lambda_i\tau_e y_i)^{1/2} + y_x - c\lambda_i\tau_e$, monotonic divergence is not consistent with the set Eqs. 3-5, and all variables ϕ, X, I diverge in an oscillatory manner.

It should be emphasized that all of these results have been derived without any approximations or tedious computations, as opposed to other approaches to the problem. Furthermore, the existence of bounds does not necessarily imply that the bounds are tolerable. In fact, they may be extremely large.

(iii) Existence of Periodic Solutions

The question of the existence of periodic solutions can be established by means of Poincaré's method of sections and Brouwer's fixed-point theorem. To this effect, investigate the existence of a toroidal region that does not contain the critical point and whose bounding surface is intersected inwardly by the trajectories.

Consider, first, $\alpha > \gamma$. Notice that for all values of $\alpha > \gamma$ one of the characteristic roots of Eq. 7 is always real negative, say $-s_1$ ($s_1 > 0$). This implies that no closed surface can be found in the neighborhood of the critical point which is crossed outwardly by the trajectories because, for $-s_1 < 0$, there are always two trajectories approaching the critical point. However, a small open-ended cylindrical surface around the critical point, intersected outwardly by the trajectories, does exist when the former is unstable. To prove this, proceed as follows:

Consider the system of Eqs. 3-5 and transfer the origin of the phase space to the critical point. Thus

$$\frac{d\phi}{dt} = -\omega_o X - \omega_o \phi X \tag{12}$$

$$\frac{dX}{dt} = \lambda_x[(\alpha-\gamma)\phi+\beta I-(\gamma+1)X-\gamma\phi X] \tag{13}$$

$$\frac{dI}{dt} = \lambda_i[\phi-I] \tag{14}$$

A linear transformation of ϕ, I, X into ϕ_1, I_1, X_1, by means of the modal matrix that corresponds to the characteristic roots reduces the linear approximation to its normal form and Eqs. 12-14 to

$$\frac{d\phi_1}{dt} = -s_1\phi_1 + f_1 \tag{15}$$

$$\frac{dX_1}{dt} = uX_1 + vI_1 + f_2 \tag{16}$$

$$\frac{dI_1}{dt} = -vX_1 + uI_1 + f_3 \tag{17}$$

where the f's are second-order polynomials in (ϕ_1, I_1, X_1).

Define the cylinder

$$C = X_1^2 + I_1^2 > 0 \tag{18}$$

Notice that

$$\frac{dC}{dt} = 2uX_1^2 + 2uI_1^2 + 2(X_1f_2+I_1f_3) > 0 \tag{19}$$

because $X_1f_2 + I_1f_3$ is of third order in ϕ_1, I_1, X_1, and for sufficiently small values of these, the first two terms in the right-hand side of Eq. 19 dominate. The meaning of Eqs. 18 and 19 is that there is a small neighborhood around the critical point in which the cylinder C is intersected outwardly by the trajectories.

The direction of the axis of the cylinder is determined by the directional cosines with respect to ϕ, I, X of the principal axis ϕ_1, which corresponds to the characteristic root $-s_1$. These cosines are

$$\cos \alpha_\phi = \frac{[s_1-\lambda_x(\alpha+\beta)][s_1-\lambda_i]}{\left\{[s_1-\lambda_x(\alpha+\beta)]^2[s_1-\lambda_i]+\lambda_i^2[s_1-\lambda_x(\alpha+\beta)]^2+\lambda_x^2[\lambda_i-s_1(\alpha-\gamma)]^2\right\}^{1/2}}$$

$$= \frac{[s_1-\lambda_x(\alpha+\beta)][s_1-\lambda_i]}{D} \tag{20}$$

$$\cos \alpha_I = \frac{-\lambda_i[s_1-\lambda_x(\alpha+\beta)]}{D}$$

$$\cos \alpha_x = \frac{\lambda_x[\lambda_i-s_1(\alpha-\gamma)]}{D}$$

It can be shown that

$$\lambda_x(\alpha+\beta) < s_1 < \frac{\lambda_i}{\alpha-\gamma} \tag{21}$$

Therefore, the principal axis ϕ_1 and the cylinder are oriented as shown in Fig. II-33.

Next, extend the cylinder by two funnel-like surfaces beyond the equilibrium point, as shown in Fig. II-34. The funnels consist of three mutually intersecting planes:

EPQE and EP_1Q_1E: Plane E_9 defined by $\phi = I$

EQRE and EQ_1R_1E: Plane E_{10} defined by $bI + X = b + 1$ $(b > 0)$

ERRE and EP_1R_1E: Plane E_{11} defined by $-c\phi + X = 1 - c$ $(c > 0)$

Require that the slopes of planes E_{10} and E_{11} be such that the principal direction ϕ_1 is inside the funnels — a condition that is easily fulfilled.

Now, all trajectories cross the funnels outwardly because

$$\frac{d\phi}{dt} \gtrless 0 \quad \text{for} \quad X \lessgtr 1 \quad \text{and} \quad \frac{dI}{dt} = 0 \quad \text{on } E_9$$

$$\frac{dX}{dt} \gtrless 0 \quad \text{and} \quad \frac{d\phi}{dt} \gtrless 0 \quad \text{for} \quad X \lessgtr 1 \quad \text{on } E_{10}$$

$$\frac{dX}{dt} \gtrless 0 \quad \text{and} \quad \frac{d\phi}{dt} \gtrless 0 \quad \text{for} \quad X \lessgtr 1 \quad \text{on } E_{11}$$

Note, however, that the slope of E_{11} can be decreased as in the case of E_8 (Fig. II-31) to have the trajectories intersecting outwardly. This does not conflict with the requirement of the directional cosines.

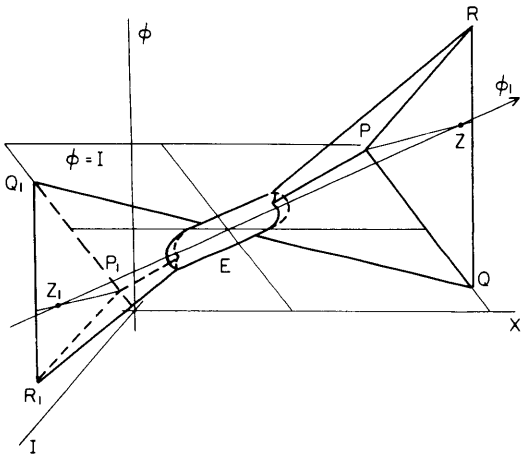

Fig. II-33. Open-ended surface around critical point E, intersected outwardly by all trajectories.

Superposition of the surfaces shown in Figs. II-31 and II-33 results in the critical-point, free toroidal region that was sought, if the volumes of Fig. II-31 falling into the funnels and the cylinder, as well as the origin, are excluded. The exclusion of the origin is straightforward because one of the characteristic roots is positive. A simple review of the behavior of the trajectories on the planes E_1 through E_{11} and the cylinder C immediately reveals that the bounding surface of the torus is crossed by the

trajectories inwardly everywhere. Therefore the topological torus constitutes a trajectory trap.

A typical cross section of the toroidal region by the plane I = 1 is shown in Fig. II-34. Two simply connected sections S_1 and S_2 result. Observe that any trajectory that is originally in the torus is trapped there. Furthermore, it intersects the section S_1 toward the plane of the figure along the positive I direction ($dI/dt > 0$ on S_1), and the section S_2 away from the plane of the figure along the negative I direction ($dI/dt < 0$ on S_2). This implies that a trajectory starting from a point $(\phi_o, I_o=1, X_o)$ on S_1 moves away and cannot return to S_1 along the negative I direction, and so on. Similar considerations of the signs of the vector field $\frac{d\phi}{dt}$, $\frac{dI}{dt}$, $\frac{dX}{dt}$ in the various regions of the torus lead to the overall conclusion that the trajectories circulate around the torus. Therefore, the simply connected section S_1 is topologically mapped into itself by a continuous vector field which circulates in a region free of critical points. According to Brouwer's fixed-point theorem, the mapping possesses a fixed point, or the system admits periodic solutions.

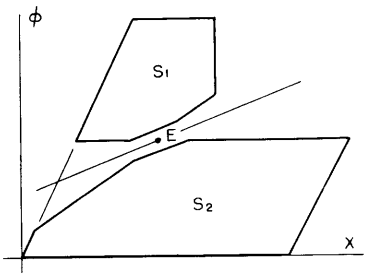

Fig. II-34. Cross section of toroidal surface surrounding critical point E by the plane I = 1.

Similar arguments apply when $y_x < c\delta_o < y_x + c\lambda_i\tau_e$ and it is concluded that the system admits periodic solutions.

To summarize, when $c\delta_o < y_x + c\lambda_i\tau_e$ and the critical point is unstable, the system oscillates. The oscillations may be sinusoidal or of the relaxation type. It should be pointed out that the existence of the solid torus is not adequate topology to guarantee either the uniqueness or the stability of the periodic solutions. Such questions can be examined by means of the general theorem of existence of periodic solutions, but this is beyond the scope of this report. Also, it should be noted that the existence of a negative characteristic root implies that some exceptional trajectories may indeed converge to the critical point, even when it is unstable.

On the other hand, when $y_x + c\lambda_i\tau_e < c\delta_o$ no closed surface surrounds the critical point and the system in always unbounded (Fig. II-30). The unboundedness manifests itself either by diverging oscillations or by a monotonically increasing ϕ with a bounded X.

E. P. Gyftopoulos

References

1. S. Lefschetz, Differential Equations, Geometric Theory (Interscience Publishers, Inc., New York, 1957).

2. L. L. Rauch, Oscillation of a third-order nonlinear autonomous system, Contributions to the Theory of Nonlinear Oscillations, Annals of Mathematics Studies No. 20 (Princeton University Press, Princeton, N.J., 1950), pp. 39-88.

3. E. P. Gyftopoulos, Applications of geometric theory to nonlinear reactor dynamics (to be published in J. Nuclear Sci. Engr.).

10. INSTABILITY CAUSED BY THE ELECTRIC CURRENT PERPENDICULAR TO THE MAGNETIC FIELD

In Quarterly Progress Report No. 60, the author showed (1) that it is necessary to have an instability to account for a large current observed in the Penning Ionization Gauge (PIG) discharge. It was shown that the instability is produced if there is a radial current. The mechanism is loosely defined as a two-beam instability perpendicular to the magnetic field. This instability is quite different from the conventional two-beam instability discussed by Bernstein and Kulsrud (2). They have considered only the electrostatic wave, which was shown to propagate only parallel to the magnetic field. There is another class of waves, magnetohydrodynamic or magnetoacoustic waves. These waves are characterized by the fact that ions and electrons tend to move together, so that the charge separation is small. These waves are similar to the Alfvèn waves. However, the former can propagate perpendicular to the magnetic field (3).

In order to demonstrate the instability caused by the perpendicular component of the

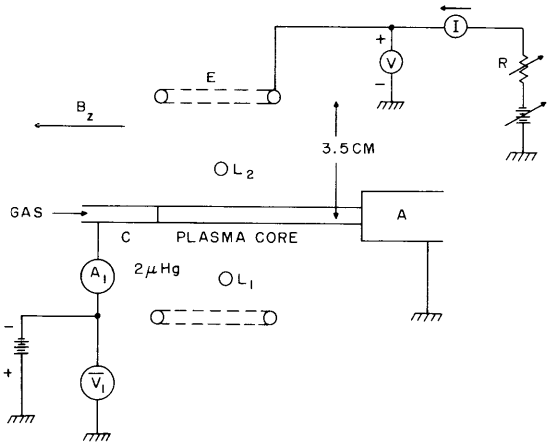

Fig. II-35. Experimental configuration. (A is the anode; C, the cathode; E, the third electrode; L_1, L_2, Langmuir probes; V, bias voltage; I, radial current.)

electric current, an experiment with the configuration shown in Fig. II-35 was carried out in the system of the hollow-cathode discharge that has been previously reported (4). The main arc was run between cathode C and anode A. The arc current and voltage were 23 amps and 28 volts. An external magnetic field of 500 gauss was applied longitudinally. Argon gas was maintained at approximately 2μ Hg during the experiment. The third electrode, E, was biased with respect to the anode, and the resulting oscillation was observed by the Langmuir probe L_1, while the density and temperature were measured by the Langmuir probe L_2.

With no current being drawn by the third electrode, the temperature of the plasma was 1.5 ev. The density was approximately 10^{13}/cc near the axis. The floating potential of the third electrode was approximately +1 volt. The peak-to-peak value of the noise was approximately 1.7 volts.

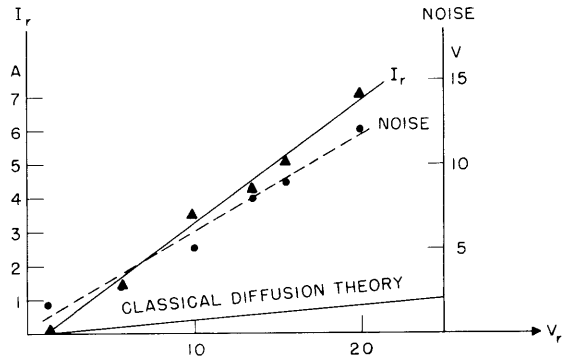

Fig. II-36. Radial current and noise as a function of applied radial electric potential.

It was found that the radial current is very small, if the third electrode is biased negative so that it draws ion current. The order of magnitude of that current was approximately 100 ma, which value is roughly in agreement with classical diffusion theory. The noise level remained unchanged. No spectacular change was observed with the bias of -24 volts. However, the situation was completely different, when the third electrode was biased positive. The radial current exceeded 1 amp with the applied voltage of 5.8 volts, and the noise level increased to 3.0 volts. The results are shown in Table II-2 and Fig. II-36. Note that classical diffusion theory predicts a different tendency. The last column of the table represents the power input from the third electrode, which is only a fraction of the power of 640 watts dissipated by the main arc.

These results indicate clearly that the diffusion is governed by the "anomalous diffusion," and that the instability can be caused by the radial electric current. Instability caused by the radial electric field is ruled out because there was no observed increase

Table II-2. Experimental results.

Radial Electric Current (amp)	Bias (volts)	Noise Level (peak to peak) (volts)	Electron Temperature (ev)	Power to E (current × bias in watts)
0	1.1	1.7	1.45	0
1.5	5.8	3.0		8.7
3.4	10.0	5.0		34
4.4	13.5	8	3.0	60
5.2	15.5	9		80
7.0	20.0	12		140

in diffusion, when the third electrode was biased negative.

The theory of two-beam instability perpendicular to the magnetic field can explain the observed oscillations of the PIG discharges (5). Allen, Kino, and Lawson (6) have observed the oscillation in their cesium discharge and found that it becomes smaller if the electrodes are lined up with the external magnetic field. Their result can presumably be explained by the existence of the perpendicular component of the electric current.

S. Yoshikawa

References

1. S. Yoshikawa, Transport coefficients calculated from the Liouville equation, Quarterly Progress Report No. 60, Research Laboratory of Electronics, M.I.T., Jan. 15, 1961, pp. 65-70.

2. I. B. Bernstein and R. M. Kulsrud, Phys. Fluids 3, 937 (1960).

3. D. A. Frank-Kamenetskii, J. Tech. Phys. (U.S.S.R.) 5, 847 (1961).

4. L. M. Lidsky, S. D. Rothleder, and S. Yoshikawa, Studies of the hollow-cathode discharge plasma, Quarterly Progress Report No. 59, Research Laboratory of Electronics, M.I.T., Oct. 15, 1960, pp. 22-27.

5. F. F. Chen and R. Bingham, Bull. Am. Phys. Soc. Ser. II 6, 189 (1961) (Abstract).

6. M. A. Allen, G. S. Kino, and J. D. Lawson, Bull. Am. Phys. Soc. Ser. II 6, 191 (1961) (Abstract); Report AFCRC-TN-60-587, Air Force Cambridge Research Center, Bedford, Massachusetts, 1960, p. 15.

II-C. PLASMA MAGNETOHYDRODYNAMICS AND ENERGY CONVERSION*

Prof. E. N. Carabateas
Prof. J. A. Fay
Prof. G. N. Hatsopoulos
Prof. W. D. Jackson
Prof. H. P. Meissner
Prof. D. C. Pridmore-Brown
Prof. A. H. Shapiro
Prof. H. H. Woodson
L. Y. Cooper
R. S. Cooper
D. M. Dix
D. A. East
W. H. Heiser
E. D. Hoag
S. A. Khayatt
G. B. Kliman
P. Klimowski
A. Kniazzeh
M. F. Koskinen
A. T. Lewis
J. R. Melcher
W. T. Norris†
J. P. Penhune
E. S. Pierson
J. W. Poduska
J. H. Wasserlein

1. ELECTROHYDRODYNAMIC AND MAGNETOHYDRODYNAMIC SURFACE WAVES AND INSTABILITIES

The perfectly conducting fluid commonly forms the basis for magnetohydrodynamic stability studies. With this model the existence of surface currents has physical meaning and leads to incompressible surface waves or instabilities characterized by the Alfvèn velocity. As a direct consequence of the natural tendency of currents to diffuse throughout the bulk of a conducting fluid, the perfect conductor can be simulated in the laboratory only with difficulty. It is natural to ask what the properties would be of an analogous system involving surface charges and electric fields rather than currents and magnetic fields. The electrohydrodynamic system has the advantage of being more easily realized because the charges relax to the boundaries with time.

Although many surface interactions with electric fields are controlled by the semiconducting properties of the fluid (1), there is a class of interactions which occurs in the limit of vanishing conductivity. An example is the stabilization of a dielectric liquid jet by a longitudinal electric field (2), a problem which is formally similar to the stabilization of the M-H pinch by a magnetic field (3).

A comparison is made here between two simple electrohydrodynamic and magnetohydrodynamic systems involving a surface interaction in plane geometry. The surface dynamics are formulated in terms of the surface traction of Korteweg and Helmholtz (4). Experimental results are given for the two electrohydrodynamic cases.

a. Theoretical Analysis

The four problems considered each involve a region filled with two nonmiscible liquids separated by a plane interface of tension T parallel to two rigid boundaries. The liquids are presumed inviscid, incompressible and perfect dielectrics. A gravitational field g is taken as acting in the negative direction with the other axes lying in the plane

*This work was supported in part by National Science Foundation under Grant G-9330, and in part by WADD Contract AF33(616)-7624 with Flight Accessories Laboratory, Wright-Patterson Air Force Base, Ohio.

†Commonwealth Fellow from England, 1960-61.

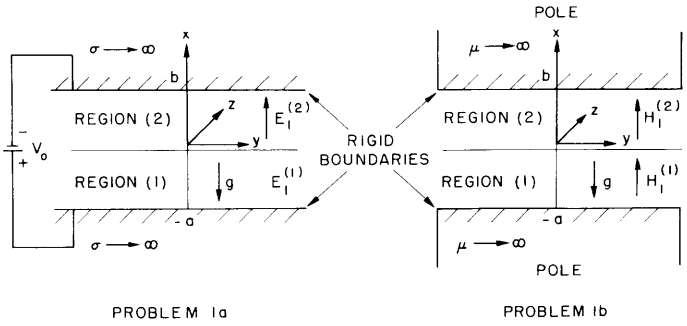

Fig. II-37. A liquid interface stressed by a normal electric or magnetic field. Problem 1a: Electric field with free, or no free charge on interface. Problem 1b: Magnetic field.

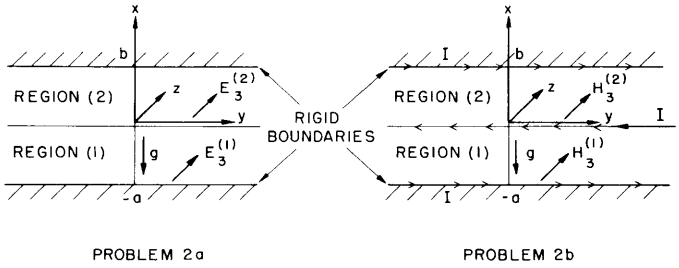

Fig. II-38. A liquid interface stressed by a tangential electric or magnetic field. Problem 2a: Electric field. Problem 2b: Magnetic field with free, or no free currents on interface.

of the static interface. The problems considered are shown in Figs. II-37 and II-38. Problem 1a, with a static electric field $\overline{E}$ in the x direction, includes the idealized case of no free charge on the boundary, as well as the case in which sufficient time has elapsed for charge to relax to the interface. Similarly, Problem 2b, with a static magnetic field $\overline{H}$ in the z direction includes the possibility of amperian or free currents on the interface. Problems 1b and 2a are formally similar to Problems 1a and 2b when these problems are considered without free charges or currents on the interface. The circumstance of a real surface current might be created by a conducting film at the interface.

Problem 2b, for $\mu_1 = \mu_2$ = permeability of free space and surface tension T = 0, $a = b \to \infty$, is equivalent to the incompressible limit of the gravitational instability considered by Kruskal and Schwarszchild (5).

(i) Equations

Surface dynamics will be discussed for small displacements from the equilibrium condition of no fluid velocity v. Hence the equations of motion are:

$$\nabla \cdot \overline{v} = 0 \tag{1}$$

$$\rho \frac{\partial \overline{v}}{\partial t} + \nabla p' = -g\rho \bar{a}_1 \tag{2}$$

$$\nabla \times \overline{E} = -\mu \frac{\partial \overline{H}}{\partial t} \tag{3}$$

$$\nabla \cdot \mu H = 0 \tag{4}$$

$$\nabla \times \overline{H} = 0 \tag{5}$$

$$\nabla \cdot \epsilon \overline{E} = 0 \tag{6}$$

where p' is the fluid pressure, and $\bar{a}$ is a vector with unit components in the axis directions. Subscripts 1, 2, 3 will be used to indicate vector components, and superscripts (1), (2) will indicate regions in which variables are to be evaluated. A normal vector $\bar{n}$, when evaluated at the interface, will be taken as positive when it extends from region (1) to region (2). In static equilibrium this is the direction of the positive x axis. The constitutive equations for the fluids are assumed to be linear with the electric and magnetic inductive capacities given by $\epsilon = k_e \epsilon_o$ and $\mu = k_m \mu_o$.

From Eq. 2, the static pressure is given by

$$p' = -\rho g x + p_o \tag{7}$$

Small departures from the static solutions are considered to be of the form

$$p = \hat{p} \exp(at + \beta_2 y + \beta_3 z) \tag{8}$$

The assumption of negligible displacement and conduction currents is justified in Eq. 5, provided that

$$\left|\beta_2^2\right| + \left|\beta_3^2\right| \gg \left|\mu\sigma a\right| + \left|\mu\epsilon a^2\right| \tag{9}$$

This is an extremely good approximation for the fluids considered here.

By using Eqs. 1-3, and 5, all of the incremental variables can be written in terms of the scalars $\hat{p}$, $\hat{e}_3$, and $\hat{h}_3$ which satisfy the relation

$$\left[\frac{d^2}{dx^2} - \tau^2\right] \begin{bmatrix} \hat{p} \\ \hat{e}_3 \\ \hat{h}_3 \end{bmatrix} = 0 \tag{10}$$

where $\tau^2 = -\beta_2^2 - \beta_3^2 = -\beta^2$, and $\hat{e}$ and $\hat{h}$ are the perturbed electric and magnetic fields, respectively. The solutions to Eq. 10 are

$$\begin{bmatrix} \hat{p} \\ \hat{e}_3 \\ \hat{h}_3 \end{bmatrix} = \begin{bmatrix} A_1 \\ C_1 \\ D_1 \end{bmatrix} e^{\tau x} + \begin{bmatrix} A_2 \\ C_2 \\ D_2 \end{bmatrix} e^{-\tau x} \tag{11}$$

The remaining variables are written in terms of the A's, C's, and D's. Using Eqs. 1-3, and 5, we obtain

$$\hat{v}_1 = -\frac{1}{\rho a}\frac{d\hat{p}}{dx} = -\frac{\tau}{\rho a}\left[A_1 e^{\tau x} - A_2 e^{-\tau x}\right] \tag{12}$$

$$\hat{v}_2 = -\frac{\beta_2}{\rho a}\hat{p} = -\frac{\beta_2}{\rho a}\left[A_1 e^{\tau x} + A_2 e^{-\tau x}\right] \tag{13}$$

$$\hat{v}_3 = -\frac{\beta_3}{\rho a}\hat{p} = -\frac{\beta_3}{\rho a}\left[A_1 e^{\tau x} + A_2 e^{-\tau x}\right] \tag{14}$$

$$\hat{h}_1 = \frac{1}{\beta_3}\frac{d\hat{h}_3}{dx} = \frac{\tau}{\beta_3}\left[D_1 e^{\tau x} - D_2 e^{-\tau x}\right] \tag{15}$$

$$\hat{h}_2 = \frac{\beta_2}{\beta_3}\hat{h}_3 = \frac{\beta_2}{\beta_3}\left[D_1 e^{\tau x} + D_2 e^{-\tau x}\right] \tag{16}$$

$$\hat{e}_1 = \frac{1}{\beta_3}\frac{d\hat{e}_3}{dx} - \frac{a\beta_2\mu}{\beta_3^2}\hat{h}_3 = \frac{\tau}{\beta_3}\left[C_1 e^{\tau x} - C_2 e^{-\tau x}\right] - \frac{a\mu\beta_2}{\beta_3^2}\left[D_1 e^{\tau x} + D_2 e^{-\tau x}\right] \tag{17}$$

$$\hat{e}_2 = \frac{\beta_2}{\beta_3}\hat{e}_3 + \frac{a\mu}{\beta_3^2}\frac{dh_3}{dx} = \frac{\beta_2}{\beta_3}\left[C_1 e^{\tau x} + C_2 e^{-\tau x}\right] + \frac{a\tau\mu}{\beta_3^2}\left[D_1 e^{\tau x} - D_2 e^{-\tau x}\right] \tag{18}$$

(ii) Boundary Conditions

The coefficients are determined by the boundary conditions. At the interface these are written in terms of a normal vector $\bar{n}$ that, under the assumption of small displacements of the interface, satisfies the condition

$$\frac{d\bar{n}}{dt} = -\bar{a}_2\frac{\partial v_1}{\partial y} - \bar{a}_3\frac{\partial v_1}{\partial z} \tag{19}$$

This follows from the requirement that $\bar{n}$ remain perpendicular to the interface. With the use of Eq. 8, Eq. 19 gives

$$\begin{aligned} \hat{n}_1 &= 0 \\ \hat{n}_2 &= -\beta_2\hat{v}_1/a \\ \hat{n}_3 &= -\beta_3\hat{v}_1/a \end{aligned} \tag{20}$$

Equations 1-4 are integrated to give the boundary conditions. In this connection, Eq. 2 is supplemented by the superficial stresses caused by the electromagnetic field and the surface tension (6, 7). Hence, at the interface, Eqs. 1-4 require that

$$\bar{n} \cdot [\bar{v}^{(2)} - \bar{v}^{(1)}] = 0 \tag{21}$$

$$n_a \left[(p^{(2)} - p^{(1)}) - T\left(\frac{\partial^2 \xi}{\partial y^2} + \frac{\partial^2 \xi}{\partial z^2} \right) \right] - \left[T_{a\beta}^{(2)} - T_{a\beta}^{(1)} \right] n_\beta = 0 \tag{22}$$

where $T_{a\beta}$ is the Maxwell stress tensor as given by

$$T_{a\beta} = \epsilon E_a E_\beta - \frac{1}{2} \epsilon \delta_{a\beta} (1-c)\, E_\gamma E_\gamma + \mu H_a H_\beta - \frac{1}{2} \mu \delta_{a\beta} (1-d)\, H_\gamma H_\gamma$$

with d and c the magnetostriction and electrostriction terms defined as

$$d = \frac{\rho}{k_m} \frac{dk_m}{d\rho} \qquad c = \frac{\rho}{k_e} \frac{dk_e}{d\rho}$$

and ξ is the position of the interface measured in the x direction.

$$\bar{n} \times [\bar{E}^{(2)} - \bar{E}^{(1)}] - \bar{n} \cdot \bar{v} \left(\mu_2 H^{(2)} - \mu_1 H^{(1)} \right) = 0 \tag{23}$$

$$n \cdot \left(\mu_2 \bar{H}^{(2)} - \mu_1 \bar{H}^{(1)} \right) = 0 \tag{24}$$

When no real currents or charges exist on the interface, the additional conditions of Eqs. 5 and 6 are needed.

$$\bar{n} \times (H^{(2)} - H^{(1)}) = 0 \tag{25}$$

$$\bar{n} \cdot \left(\epsilon_2 \bar{E}^{(2)} - \epsilon_1 \bar{E}^{(1)} \right) = 0 \tag{26}$$

In Problem 1a the boundaries at x = -a, b are perfectly conducting, and in Problem 1b, they are infinitely permeable, so that

$$\left.\begin{aligned} &\text{Problem 1a: } \bar{n} \times \bar{E} = 0 \\ &\text{Problem 1b: } \bar{n} \times \bar{H} = 0 \end{aligned}\right\} \tag{27}$$

In Problems 2a and 2b, it is required that as $|x| \to \infty$

$$\bar{e} \to 0, \quad \bar{h} \to 0 \tag{28}$$

Finally, in both problems the boundaries are rigid, so that at x = -a, b

$$\bar{n} \cdot \bar{v} = 0 \tag{29}$$

These boundary conditions are used to determine the A's, C's, and D's. The

procedure is to finish linearizing Eqs. 21-29 and take advantage of Eq. 20 and the relation $\hat{\xi} = \hat{v}_1/a$. The solutions given by Eqs. 11-18 are then used to express these conditions as sets of homogeneous linear equations in the twelve coefficients (A's, C's, and D's in the two regions). The desired dispersion relations are given by the requirement that the respective determinants of these coefficients vanish.

(iii) Solutions

The compatibility conditions give:

$$\text{For Problem 1:}\quad \omega^2 = -a^2 = \tau^2\left[V_g^2 + V_c^2 - \begin{bmatrix} V_a^2 \\ \\ V_b^2 \end{bmatrix}\right] \tag{30}$$

$$\text{For Problem 2:}\quad \omega^2 = -a^2 = \tau^2\left[V_g^2 + V_c^2 + \frac{\tau_3^2}{\tau^2}\begin{bmatrix} V_a^2 \\ \\ V_b^2 \end{bmatrix}\right] \tag{31}$$

where

$$V_g^2 = \frac{g(\rho^{(1)}-\rho^{(2)})}{\rho_{eg}\tau} \tag{32}$$

$$V_c^2 = \frac{T\tau}{\rho_{eg}} \tag{33}$$

$$\rho_{eg} = \rho^{(2)} \coth \tau b + \rho^{(1)} \coth \tau a \tag{34}$$

The parameters V_g and V_c are the phase velocities (8) of gravity and capillary waves, and V_a and V_b are the effective Alfvèn velocity and its electrohydrodynamic dual as given below.

Problem 1a. Free charge on interface:

$$V_b^2 = \frac{1}{\rho_{eg}}\left[\epsilon^{(2)}\left(E_1^{(2)}\right)^2(1+c^{(2)}) \coth \tau b + \epsilon^{(1)}\left(E_1^{(1)}\right)^2(1+c^{(1)}) \coth \tau a\right] \tag{35}$$

Problem 1a. No free charge on interface:

$$V_b^2 = \frac{1}{\rho_{eg}}\left[\frac{(\epsilon^{(2)}-\epsilon^{(1)})(\epsilon^{(2)}(1+c^{(1)})-\epsilon^{(1)}(1+c^{(2)}))\, E_1^{(2)}E_1^{(1)}}{\epsilon^{(1)} \tanh \tau b + \epsilon^{(2)} \tanh \tau a}\right] \tag{36}$$

Problem 2a:

$$V_b^2 = (E_3)^2 \frac{(\epsilon^{(2)}-\epsilon^{(1)})(\epsilon^{(2)}(1-c^{(2)})-\epsilon^{(1)}(1-c^{(1)}))}{(\epsilon^{(2)}+\epsilon^{(1)})\,\rho_{eg}} \tag{37}$$

Problem 2b. Free current on the interface:

$$V_a^2 = \frac{\left[(1-d^{(1)})\,\mu^{(1)}\left(H_3^{(1)}\right)^2 + (1-d^{(2)})\,\mu^{(2)}\left(H_3^{(2)}\right)^2\right]}{\rho_{eg}} \tag{38}$$

The results for Problem 1b and for Problem 2b with no free surface current are given by the conditions for Problem 1a with no free charge and for Problem 2a after the substitution $\epsilon \rightarrow \mu$, $E \rightarrow H$, $c \rightarrow d$.

c. Interpretation of Theoretical Results

It follows from Eqs. 30, 35, and 36 that in the configuration of Problem 1, the electric and magnetic field intensities can always be made large enough to produce an unstable interface. (This makes the reasonable assumption that $(\epsilon^{(2)}-\epsilon^{(1)})(\epsilon^{(2)}(1+c^{(2)})-\epsilon^{(1)}(1+c^{(1)})) > 0$.) The effect of an increased electric or magnetic field is to slow down a surface wave of a given wavelength until the effective phase velocity vanishes and the surface becomes unstable. The wavelength of the instability is that value of $2\pi/\tau$ which first fulfills this condition. Equations 35 and 36 show that the electrostrictive or magnetostrictive terms act to increase the unstabilizing influence of the fields.

As would be expected, in all of the cases considered, there is an instability at some wavelength if $\rho^{(2)} > \rho^{(1)}$.

The configuration of Problem 2 is apparently more strongly dependent on the strictive terms. In fact, Eq. 37 shows that the values of the d's and c's can make the effective velocities V_a and V_b of Eq. 31 real or imaginary. The stress tensor of Eq. 22 is based on the assumption that the permittivity or permeability is only a function of ρ. For liquid dielectrics, c is often computed from the Clausius-Mossotti equation (9), which gives

$$c = \left[\frac{(k_e-1)(k_e+2)}{3k_e}\right] \tag{39}$$

It follows that

$$(\epsilon^{(2)}-\epsilon^{(1)})[\epsilon^{(2)}(1-c^{(2)})-\epsilon^{(1)}(1-c^{(1)})] = \frac{\epsilon_o^2}{3}\left(k_e^{(2)}-k_e^{(1)}\right)^2\left[2-\left(k_e^{(1)}+k_e^{(2)}\right)\right] \tag{40}$$

or, according to the Clausius-Mossotti equation, for $k_e^{(1)}$ and $k_e^{(2)}$ greater than 1, V_b^2 of

Eq. 37 is negative and the electric field slows down surface waves propagating in the z direction. In the sections that follow no experimental evidence will be found for such a large electrostriction.

If the effect of the striction is presumed to be small, Eq. 31 shows that in the configuration of Problem 2, for high electric or magnetic field intensities $\left(\left[\begin{matrix}|V_a| \\ |V_b|\end{matrix}\right] \gg |V_c| + |V_g|\right)$, transverse incompressible surface waves propagate along the field lines, which may be termed Alfvèn or electrohydrodynamic surface waves, respectively.

Experimental attention will now be given to Problem 1a with free charge and to Problem 2a. However, the implications of this discussion for the other problems should be apparent from Eqs. 30-38.

d. Experimental Results

(i) Problem 1a with Free Charge

If the fluid of region (1) is much more highly conducting than that of region (2), but still satisfies the conditions of Eq. 9, it follows that $E_1^{(1)}$ is very small compared with $E_1^{(2)}$ and may be dropped from Eq. 35. In this case, Eq. 30 shows that the interface is stable as long as $\eta > 0 (\alpha^2 < 0)$, where

$$\eta = (\tau b)^2 - [(\tau b) \coth \tau b]\, W + G \tag{41}$$

and

$$W = \frac{(1+c^{(2)})\, \epsilon^{(2)} \left(E_1^{(2)}\right)^2 b}{T}$$

$$G = \frac{(\rho^{(1)} - \rho^{(2)})\, g b^2}{T}$$

The dimensionless number W is proportional to the ratio of electric energy stored per unit volume to surface energy per unit volume, and G is proportional to the ratio of energy density stored in the gravitational field to energy density stored in the surface formation. By analogy with ordinary fluid mechanics, $\sqrt{W}$ might be called the electric Weber number, and $\left(\frac{W}{G}\right)^{1/2}$ the electric Froude number (10).

The conditions for impending instability are given by Eq. 41 with $\eta = 0$. To determine W, the function in brackets may be approximated with little error by (τb) for $\tau b > 1$, and by 1 for $\tau b < 1$. It follows that the conditions for impending instability are:

$$\text{For } \tau b > 1: \quad W = 2\sqrt{G}; \quad V_o = b\left(\frac{4(\rho^{(1)}-\rho^{(2)})\, gT}{[(1+c^{(2)})\epsilon^{(2)}]^2}\right)^{1/4} \tag{42}$$

$$\text{For } \tau b < 1: \quad W = G; \quad V_o = b^{3/2}\left(\frac{(\rho^{(1)}-\rho^{(2)})\, g}{(1+c^{(2)})\,\epsilon^{(2)}}\right)^{1/2} \tag{43}$$

Although this approximation is poor for determining the wavelength if τb is approximately 1, or less, it may be used for $\tau b \gg 1$. In this case, Eqs. 41 and 43 give the wavelength of impending instability as

$$\lambda = 2\pi\left(\frac{T}{(\rho^{(1)}-\rho^{(2)})\, g}\right)^{1/2} \tag{44}$$

Equations 42 and 43, as well as Eq. 44, provide an experimental check on the theory that has been discussed. Equations 42 and 43 give the theoretical dependence of the voltage for instability on the spacing of the top plate and the interface. The experimental arrangement of Fig. II-39 gives a check on this result.

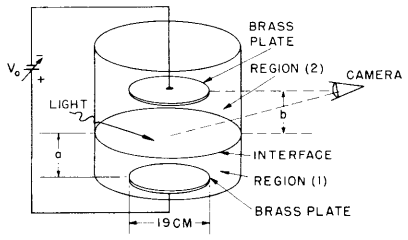

Fig. II-39. Experimental arrangement for measuring voltage for instability of an interface stressed by a normal electric field.

Several liquids were used with water to obtain curves of the general form shown in Fig. II-40 in which the voltage required to create an instability is plotted against the plate-interface spacing. In general, it is found that the curves follow the 3/2 power law for low values of b, and are linear at high values, with the transition in the region $\tau b = 1$. The plot shown is for a xylene-water interface (11). The two solid curves in Fig. II-40 indicate the theoretical results when electrostriction is or is not taken into account. The discrepancy between the curve for $c_2 = 0$ and the experimental results may be used to infer a value of 0.14 ± 0.05 for c_2, as compared with a value of 0.85 from Eq. 58.

The instability consists of a disturbance on the interface which, although initially sinusoidal in nature, quickly grows into a sharply pointed spout extending toward the upper plate. The point of instability is taken as the voltage at which this spout appears.

A sequential photograph of one section of the interface during the instability growth

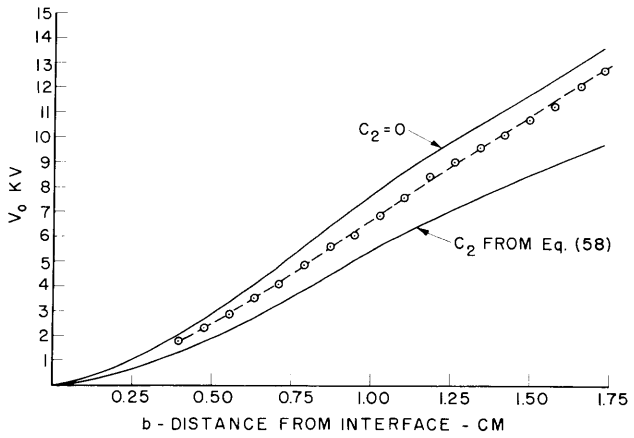

Fig. II-40. Voltage for instability V_o as a function of plate-interface spacing. The middle curve is experimental with xylene and water used. The $c_2 = 0$ curve is theoretical, without the effect of electrostriction. The curve labeled "c_2 from Eq. 58" indicates the effect of electrostriction when the Clausius-Mossotti equation is used.

is shown in Fig. II-41. The position of the viewer in these photographs is shown in Fig. II-39. Note that the initial sinusoidal disturbance quickly grows into a sharp peak with a much shorter base than the initial disturbance wavelength. As may be seen, the instability is in a more advanced stage in the background.

The sharp point of the nonlinear disturbance peak leads to a considerably increased local field intensity. If this intensity is sufficient to break down the dielectric, the instability criterion also gives a prediction of the voltage for breakdown between a liquid interface and a solid boundary.

The approximate disturbance wavelength can be taken from Fig. II-41. In this experiment, b = 5.22 cm. If we use a value of λ (from Fig. II-41) of 3.3 cm, the value of τb is approximately 5. Hence, Eq. 44 should be valid, and gives λ = 3.5 cm. This agreement is better than would be expected from the experimental error involved.

(ii) Problem 2a

Equation 31 shows that a disturbance produced at the origin in the configuration of Problem 2a would propagate along the interface at a velocity that would depend on the relative directions of the wave and the electric field. If the disturbance is assumed to propagate with the same wavelength in all directions, a viewer from above would expect to see a radiating "ellipse" with axes proportional to the phase velocities in the respective directions, as shown in Fig. II-42. This figure has been drawn under the assumption that V_b^2 is positive, or that the parameter c is of the order of magnitude predicted in the previous section.

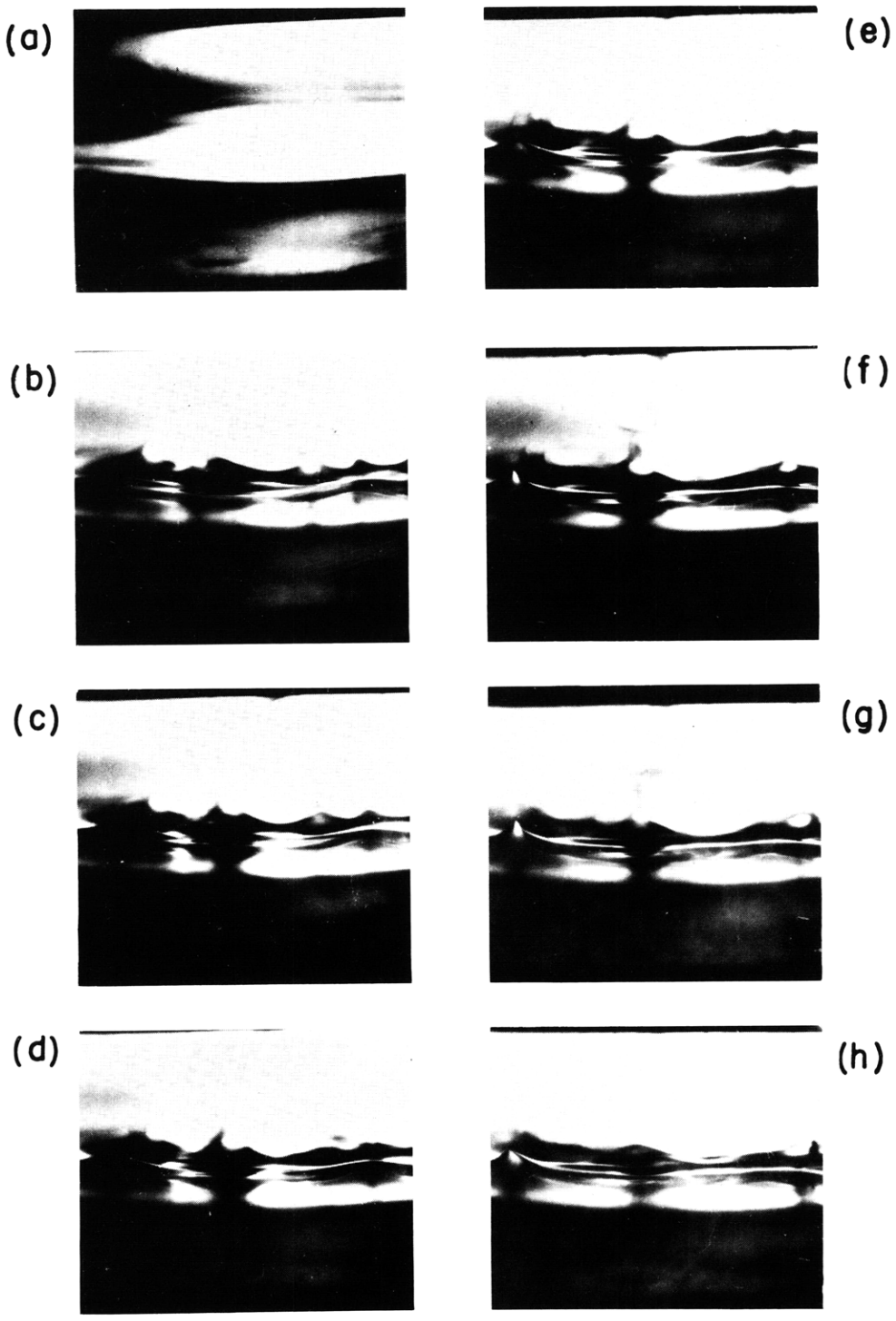

Fig. II-41. Sequential photograph of instability development at the interface stressed by normal electric field. (a) No field; (b)-(h) relative times, 2, 4, 6, 7, 8 and 9×10^{-2} sec. Note the nonlinear peak formed in the last stages.

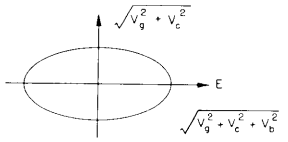

Fig. II-42. Surface wave front of constant wavelength created by a disturbance at the origin.

A qualitative check of this result was made by use of the apparatus of Fig. II-43 (essentially the configuration of Problem 2a). The maximum field attainable was limited by the electroconvection of the fluid (1).

A disturbance was produced at the interface by a burst of air from a glass pipette as shown. The interference rings from the resulting waves were photographed from above with a 1/100 sec exposure. Several of the pictures are shown in Fig. II-44 with the interface formed by air and acetophenone ($k_e \approx 19$). These pictures are only qualitative, since the wavelength is not controlled and appears to be different in the

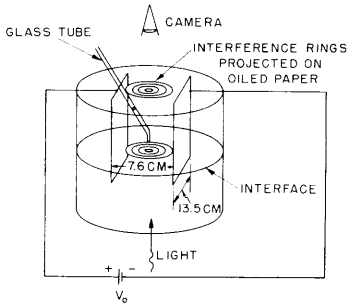

Fig. II-43. Apparatus used to photograph waves on a dielectric interface stressed by a tangential electric field.

respective axis directions. Acetophenone is a poor liquid to use (as are most liquids of high permittivity) because it has a conductivity sufficiently high to make the time constant for the relaxation of charge to the surface of the same order as $1/a$. Although Eq. 9 represents a good approximation under this condition, Eq. 26 is an unrealistic boundary condition.

The use of xylene produced essentially similar results; higher field intensities were required to produce a noticeable eccentricity. In xylene the relaxation time for free charge is considerably longer than $1/a$. Here, the eccentricity was somewhat higher than would be expected with the use of the electrostriction data of the previous section. The results of this section and the previous one are in agreement to the extent that the major axis of the observed ellipse in every case is in the direction of the electric field, and never perpendicular to it as would be predicted by Eq. 39.

The preceding discussion of the low-frequency dynamics of a plane liquid-liquid or liquid-gas interface stressed by an electric or magnetic field should serve to indicate the duality of the magnetic and electric surface interactions. The Alfvèn velocity or its electrohydrodynamic dual are fundamental for determining the wavelike or unstable

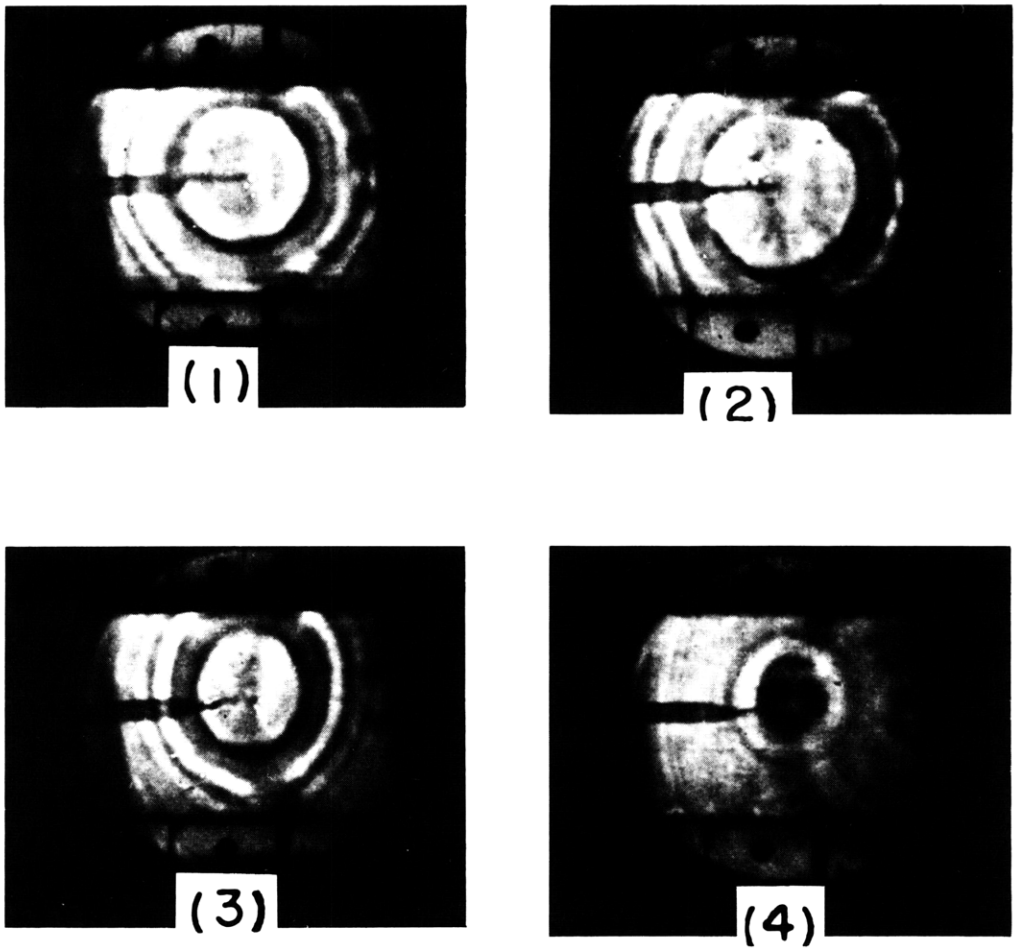

Fig. II-44. Wave patterns on the interface of acetophonone stressed by an electric field (directed from top to bottom) created by a burst of air at the center: (1) no field; (2) 4.2 kv; (3) 15 kv; (4) 20 kv.

behavior of the interface. The character of the surface dynamics is strongly dependent on the striction resulting from the interaction, at the molecular level, of the fields with the fluids. The discrete occurrence of the instability that results when an interface is stressed by a perpendicular field make possible a critical experiment for determining the nature of these interfacial strictions as they occur in dielectrics.

It is evident that the effect of these strictions is of considerable importance in determining the dynamics of the surfaces stressed by tangential fields, in which case the magnitude of the striction terms can make the motion wavelike or unstable. Our experimental results indicate independently that the effect of electrostriction is considerably less than would be expected from the use of the standard form of the Maxwell stress tensor in conjunction with the Clausius-Mossotti equation.

J. R. Melcher

References

1. W. V. R. Malkus and G. Veronis, Phys. Fluids 4, 13 (1961).

2. N. K. Nayyar and G. S. Murty, Proc. Phys. Soc. (London) 75, 369 (1960).

3. M. Kruskal and J. L. Tuck, Instability of a pinched fluid with a longitudinal magnetic field, AEC Report No. LA-1716, 1953.

4. J. A. Stratton, Electromagnetic Theory (McGraw-Hill Book Company, Inc., New York, 1941), p. 145.

5. M. Kruskal and M. Schwarszchild, Proc. Roy. Soc. (London) A223, 348 (1954).

6. J. A. Stratton, op. cit., p. 148.

7. H. Lamb, Hydrodynamics (Dover Publications, Inc., New York, 6th ed., 1932), p. 456.

8. Ibid., p. 461.

9. J. A. Stratton, op. cit., p. 140.

10. H. Rouse, Elementary Mechanics of Fluids (John Wiley and Sons, Inc., New York, 1957), p. 104.

11. The constants used for the theoretical results were taken from the Handbook of Chemistry, edited by N. A. Lange (Handbook Publishers, Inc., Sandusky, Ohio, 8th ed., 1952).

2. PERFORMANCE CHARACTERISTICS OF CESIUM THERMIONIC CONVERTERS

There are two types of voltage current characteristics obtained from cesium thermionic converters. (a) At low cesium pressures, when the cesium atom mean free path is large compared with the interelectrode spacing, the effect of collisions is negligible and the plot of ln I versus V consists of two straight lines (1). This region of operation is characterized by oscillation in the output region (2, 3). (b) When the cesium pressure is increased to such an extent that the cesium mean-free path is considerably smaller than the interelectrode spacing, the V-I curve has a smooth curvature. This shape of the V-I curve can be explained by a sheath type of analysis similar to that commonly used in double probe measurements. In this report experimental results are given for both types of operation, and a correlation of experimental and theoretical results is presented.

a. Experimental Data

The experimental data presented here were selected to illustrate these two types of operation of the cesium converter, as well as the effect of cesium coverage on the tantalum emitter.

The V-I curve shown in Fig. II-45 is for a heat input to the emitter of 2100 watts and a cesium temperature of 136°C. The corresponding cesium pressure is 4.5×10^{-3} mm Hg. The mean-free path of the cesium atoms was evaluated by means of an equation derived by Nottingham (4), and for the above-mentioned pressure was found to be $\lambda = 3 \times 10^{-1}$ cm.

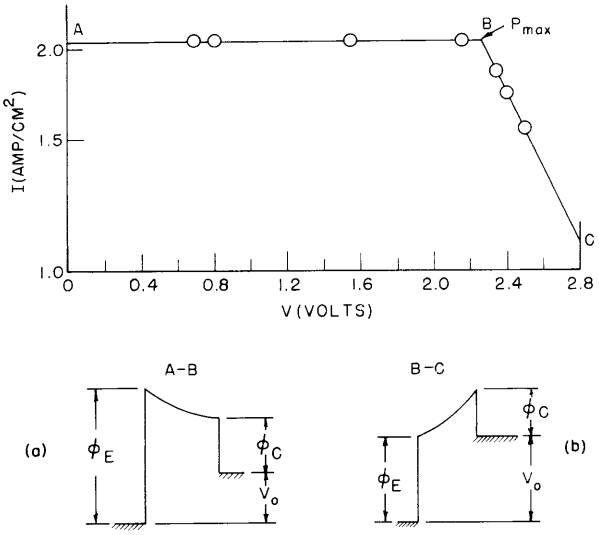

Fig. II-45. Collision-free experimental I-V curve with corresponding motive diagrams (w = 2100 watts; T_{Cs} = 136°C; λ_{Cs} = 0.3 cm; δ = 0.1 cm ($\lambda_{Cs} = 3\delta$); A = 26 cm^2).

It is realized that the mean-free path of cesium atoms is three times larger than the interelectrode spacing. The shape of the V-I curve in Fig. II-45 suggests that under these conditions the effect of collisions may be negligible.

The motive diagrams (a) and (b) shown in Fig. II-45 represent the two straight-line parts of the experimental data. The breakoff point occurs at an output voltage of 2.28 volts. We shall assume that this voltage equals the difference in the work functions of emitter and collector. The collector is maintained sufficiently cold that its work function can be considered as that of a monolayer of cesium (1.81 volts). The work function of the emitter will therefore be

$$\phi_E = \phi_C + V_B = 1.81 + 2.29 = 4.09$$

Since the work function of pure tantalum is 4.1 volts, this value indicates that the emitter is not covered with cesium. For values of the output voltage less than the difference in work functions, the output current is equal to the saturation current from the emitter.

From this value of the work function of the emitter and a saturation current of 2.04 A/cm^2, the emitter temperature can be estimated by means of Richardson's equation,

$$I_s = 2.04 = AT^2 \exp(-\phi/kT_E)$$

where A = 120.1, and therefore the value for T_E is 2430°K. This value agrees with that

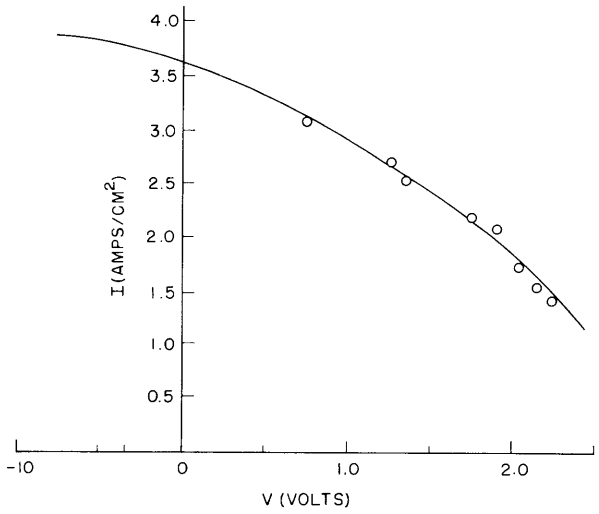

Fig. II-46. Experimental sheath type of V-I curve for 2100-watt heat input (w = 2100 watts; T_{Cs} = 250°C; λ = 0.03 mm; δ = 1 mm or 33λ; A = 26 cm^2).

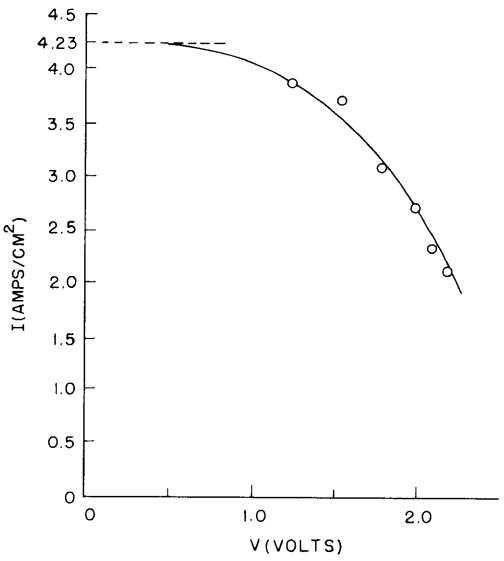

Fig. II-47. Experimental sheath type of V-I curve for 2400-watt heat input (w = 2400 watts; T_{Cs} = 250°C; λ = 0.03 mm; δ = 1 mm or 33λ; A = 26 cm^2).

inferred from a heat-transfer analysis of the unit.

For output voltages larger than the difference in work functions, the current should decrease exponentially, as can be seen from the motive diagram (b) of Fig. II-45. This is indicated by the three experimental points obtained in this region which fall on a straight line. These points are insufficient to accurately determine the slope of this line, which appears to correspond to a temperature of approximately 9000°K.

The V-I curve shown in Fig. II-46 is obtained with a 2100-watt heat input to the emitter at a cesium-bath temperature of 250°C. The cesium pressure for this temperature is 4.5×10^{-1} mm Hg, and the mean-free path is $\lambda = 3 \times 10^{-3}$ cm. Hence, in this case, the mean-free path is 33 times smaller than the spacing and the effect of collisions should dominate the operation of the device. That this is true is manifested by the radical change in the shape of the V-I curve shown in Fig. II-46 from that shown in Fig. II-45. In Fig. II-47 the experimental V-I curve is shown for an increased heat input of 2400 watts and the same cesium temperature of 250°C.

It should be noted that in the collision-free operation the emitter work function and the emitter temperature can be readily determined from the experimental V-I curve. In the following discussion a method will be outlined for determining the quantities given above from an experimental sheath type of voltage-current characteristic. This method will then be applied to obtain these quantities from the curves shown in Figs. II-46 and II-47.

b. Theoretical Analysis of the Sheath Type of Operation

The sheath type of operation of the cesium converter can be analyzed theoretically by considering that the part of the V-I curve in the positive electric power output region is really a part of a sheath curve. This sheath curve shows saturation in the current for

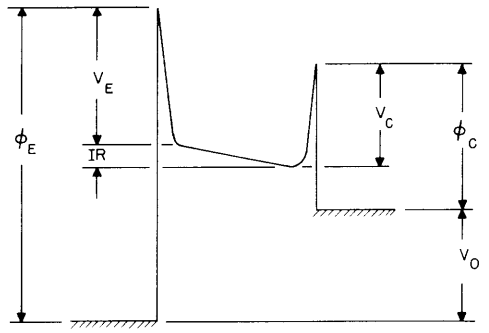

Fig. II-48. Motive diagram of a plasma thermionic converter.

very large negative and positive values of the voltage. Such curves are obtained whenever sheaths are formed at the electrodes.

When many collisions occur in the interelectrode spacing of a cesium converter a

plasma is formed there with a space-charge sheath at each end; one next to the emitter, and the other next to the collector. Let the voltage of the emitter sheath be called V_E and that of the collector, V_C. It is then seen from Fig. II-48 that the output voltage will be given by

$$V = \phi_E - \phi_C - V_E + V_C - IR \tag{1}$$

The net current flowing through the device can be expressed at the emitter side in terms of the potential V_E of the emitter sheath and the random electron current I_e in the plasma. The same current can be expressed at the collector side in terms of the potential V_C of the collector sheath and the random electron and ion currents in the plasma.

The assumption is made that the plasma is uniform. This means that the electron concentration, electron temperature, and therefore random electron current, have the same value at the two edges of the plasma (next to the emitter and the collector). Also, the ion current is neglected on the emitter side. Therefore we have

$$I = I_s - I_e \exp(-V_E/kT_e) \tag{2a}$$

$$I = I_e \exp(-V_C/kT_e) - I_p \tag{2b}$$

where I is the net current flowing through the device, I_s is the saturation current of the emitter, I_e is the random electron current, I_p is the random ion current, and T_e is the temperature of the electrons. Elimination of I_e from Eqs. 2a and 2b yields

$$\frac{I_s - I}{I_p + I} = \exp\left(-\frac{V_E - V_C}{kT_e}\right) \tag{3}$$

Substituting the value of $V_E - V_C$ in terms of the output voltage from Eq. 1, we obtain

$$\frac{I_s - I}{I_p + I} = \exp\left(\frac{V}{kT_e} - \frac{\phi_E - \phi_C}{kT_e} + IR\right) \tag{4}$$

Or, taking the natural logarithm of both sides, we get

$$\ln\frac{I_s - I}{I_p + I} = \frac{V}{kT_e} - \frac{\phi_E - \phi_C}{kT_e} + IR \tag{5}$$

Now, let the quantity ψ be defined as

$$\psi = \frac{I_s - I}{I_p + I} \tag{6}$$

Then, if the IR-drop term is neglected, Eq. 5 takes the form

$$\ln \psi = \frac{V}{kT_e} - \frac{\phi_E - \phi_C}{kT_e} \tag{7}$$

If we assume that the electron temperature T_e does not vary appreciably with V, Eq. 7 shows that the plot of $\ln \psi$ versus V should be a straight line, the slope of which should give T_e. Once the electron temperature is found, the difference in work functions of the emitter and the collector can be determined from Eq. 7. If the collector work function is known, the emitter work function can be obtained.

If the emitter work function and the value of the saturation current are known from the V-I curve, the temperature of the emitter can be estimated by means of Richardson's equation. It is therefore possible to obtain from a sheath type of V-I curve all of the basic information pertinent to the operation of the cesium converter, provided that the collector work function or the emitter temperature is known.

From Eq. 4 it is obvious that as V tends to $+\infty$, the current I tends to $-I_p$. On the other hand, as V tends to $-\infty$, the current I tends to I_s.

c. Correlation of Theoretical and Experimental Results

Let us estimate from the V-I curve shown in Fig. II-46 the value of the saturation current I_s to be 3.8 amp/cm^2. From this value of I_s and the value of the current I corresponding to each value of the output voltage, as obtained from the V-I curve, the quantity ψ defined by Eq. 6 is calculated for different values of the output voltage. The

Table II-3. Curve with I_s = 3.8 amp/cm^2 = 98.7 amp.

V (volts)	I (amp)	$I_s - I$ (amp)	$\frac{I_s - I}{I}$
.75	80	18.7	.234
1.25	70	28.7	.41
1.35	68	30.7	.452
1.75	57	41.7	.732
1.90	54	44.7	.829
2.05	45	53.7	1.19
2.15	40	58.7	1.47
2.25	38	60.7	1.60

random ion current I_p has been neglected because in the range of V in which experimental data are available I_p will be negligible as compared with I. This, of course, is not true for small values of the output current I. The results of the calculations of the

Table II-4. Curve with I_s = 4.2 amp/cm^2 = 109 amp.

V (volts)	I (amp)	$I_s - I$ (amp)	$\frac{I_s - I}{I}$
1.25	100	9	.09
1.55	93	16	.172
1.80	80	29	.362
2.00	70	39	.557
2.10	60	49	.818
2.20	55	54	.98

quantity ψ for the V-I curve of Fig. II-46 are summarized in Table II-3. In these computations the actual experimental points have been used and not points obtained from the smoothed V-I curves shown in Figs. II-46 or II-47.

The plot of log ψ versus V is shown in Fig. II-49. It is seen that the experimental points fall approximately on a straight line. The slope of this line indicates an electron temperature of 9000°K. Such high electron temperatures have been predicted by Nottingham (5), and by Lewis and Reitz (6). They are usually attributed to the emitter sheath which accelerates the electrons to very high energies. With the value of T_e determined, Eq. 7 will give the difference in work functions $\phi_E - \phi_C$ from any pair of corresponding values of V and I obtained from the V-I curve. In

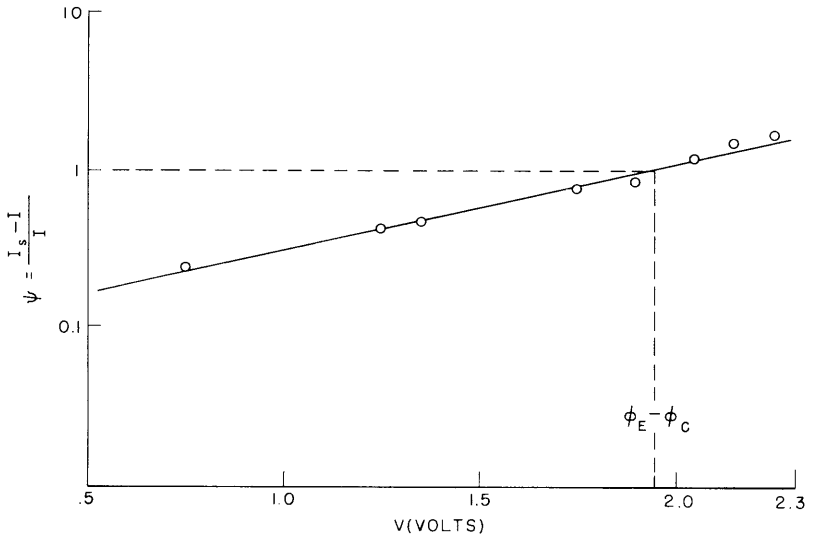

Fig. II-49. ψ versus V plot for Fig. II-46 (T_e = 9000°K; ϕ_C = 1.81 volts; ϕ_E = 3.76 volts; T_E = 2300°K).

this way we find that $\phi_E - \phi_C = 1.95$ volts.

If we assume that $\phi_C = 1.81$ volts, the emitter work function is $\phi_E = 3.76$ volts. Since the emitter work function and the emitter saturation current density are known, the emitter temperature can be estimated by means of Richardson's equation. It is found that $T_E = 2300°K$. The same method of approach has been applied to the experimental V-I curve shown in Fig. II-47 obtained at a higher heat input to the emitter than that in the V-I curve of Fig. II-46 and for the same cesium pressure.

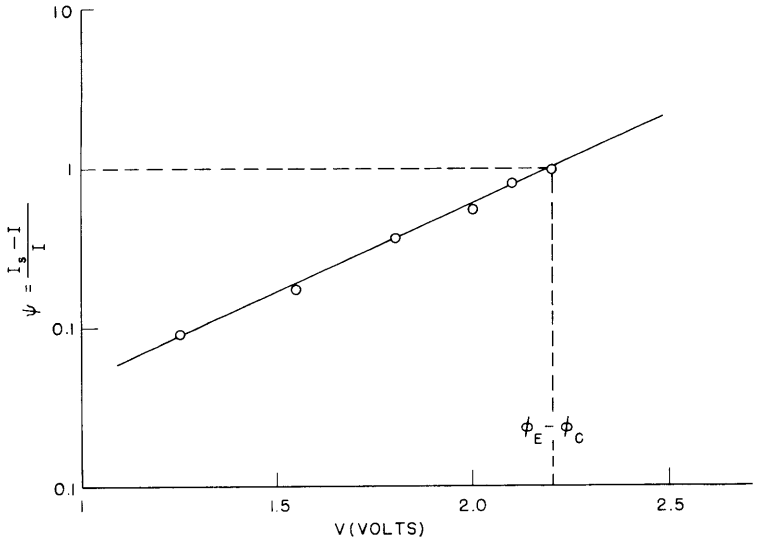

Fig. II-50. ψ versus V plot for Fig. II-47 ($T_e = 4540°K$; $\phi_C = 1.81$ volts; $\phi_E = 4.01$ volts; $T_E = 2480°K$).

The saturation current, as estimated from Fig. II-47, is approximately equal to 4.2 amp/cm^2. The quantity ψ is then computed and the results are summarized in Table II-4. Finally, log ψ is plotted versus V and the result is shown in Fig. II-50. The experimental points, again, fall approximately on a straight line. The electron temperature determined from the slope of the line is found to be $T_e = 4540°K$. The emitter work function as obtained from Eq. 7 is $\phi_E = 4.01$ volts. The corresponding emitter temperature is estimated to be $T_E = 2480°K$.

The emitter temperatures estimated above are close to the values obtained by means of a heat-balance equation that involves the known heat input and the heat rejected by electron cooling and radiation.

G. N. Hatsopoulos, E. N. Carabateas

(References on following page)

References

1. K. C. Hernqvist, M. Kaneisky, and F. H. Norman, RCA Rev. 19, 244 (1958).

2. H. L. Garvin, W. B. Teutch, and R. W. Pidd, Generation of alternating current in the cesium cell, J. Appl. Phys. 30, 1508-1509 (1960).

3. K. P. Luke and F. E. Jamerson, Low-frequency oscillations in a filamentary cathode cesium diode converter (to be published in J. Appl. Phys., March 1961).

4. W. B. Nottingham, Chapter 2, p. 1; Chapter 8, p. 1 in Direct Conversion of Heat to Electricity, Summer Session, M. I. T., 1960, edited by J. Kaye and J. Welsh.

5. W. B. Nottingham, General theory of the plasma diode energy converter, Report on the Twentieth Annual Conference on Physical Electronics held March 24-26, 1960 at M. I. T., pp. 95-114.

6. H. W. Lewis and J. R. Reitz, Efficiency of the plasma thermocouple, J. Appl. Phys. 30, 723 (1960).